^{197}Au

Mössbauer Spectroscopy

hyperfine interactions and dynamical behaviour of gold in molecular crystals and small particles.

Thijs Viegers

ERRATA

Page

2	Table 1.1	:	cm^{-3} should read cm^{-1}
13	Figure 2.6, upper line:		SN 74123N should read SN7474N
15	Eq. 2.3 should read	:	$R = \alpha \sqrt{n} = \alpha \sqrt{Ct}$
35	Table 3.4	:	$(\mu_2 - \mu_1)$ should read $(m_2 - m_1)$
37	Line 10	:	Eq. 3.36 should read Eq. 3.32
44	Eq. 4.11	:	replace Σ by $\int$, and $\int$ by Σ
45	Eq. 4.13	:	$N(v_s)$ should read $M(v_s)$
47	Line 11	:	0.939 should read 0.929
51	Line 7	:	Eq. 3.43 should read Eq. 3.48
51	Line 29	:	$t_a < 2$ should read $t_a < 4$
72	Table 5.9	:	σ_p should read σ_z
76	Table 5.11	:	Eq. 5.4 should read Eq. 5.6
78	Line 33	:	$(3d^{10}6s6p)$ should read $(5d^{10}6s6p)$
78	Line 34	:	$(3d^{10}6s)$ should read $(5d^{10}6s)$
108	Figure 7.6 (c)	:	$\alpha(I = 1/2) = -8.4$ mm/sec
109	Figure 7.7	:	$\alpha(I = 1/2) = -8.4$ mm/sec
123	Figure 8.4	:	Average particle diameter is 50 Å

h^2 should read h^2 in Eqs. 6.3, 6.4, 6.11, 6.12, 8.2 and 8.8

^{197}Au MÖSSBAUER SPECTROSCOPY

HYPERFINE INTERACTIONS AND DYNAMICAL BEHAVIOUR OF GOLD IN MOLECULAR CRYSTALS AND SMALL PARTICLES

PROMOTOR DR J.M. TROOSTER

^{197}Au MÖSSBAUER SPECTROSCOPY

HYPERFINE INTERACTIONS AND DYNAMICAL BEHAVIOUR
OF GOLD IN MOLECULAR CRYSTALS AND SMALL PARTICLES

PROEFSCHRIFT

TER VERKRIJGING VAN DE GRAAD VAN DOCTOR
IN DE WISKUNDE EN NATUURWETENSCHAPPEN
AAN DE KATHOLIEKE UNIVERSITEIT TE NIJMEGEN, OP GEZAG VAN
DE RECTOR MAGNIFICUS, PROF DR A J H VENDRIK,
VOLGENS BESLUIT VAN HET COLLEGE VAN DECANEN
IN HET OPENBAAR TE VERDEDIGEN
OP VRIJDAG 12 NOVEMBER 1976
DES NAMIDDAGS TE 4 UUR

door

MATHIAS PETRUS ANTONIUS VIEGERS
geboren te Nijmegen

Aan Wilma,

Sander en Nina

Lay Out: *Elly van Kuijck*

Design Cover: *Emile Viegers*

Illustrations: *Depts. of Illustration and Photography, Faculty of Science*

CONTENTS

CHAPTER 4

CHAPTER 5

CHAPTER 1

INTRODUCTION

The Mossbauer effect is the phenomenon of recoilless emission or absorption of γ-rays. As there exist many textbooks on theory and applications of the Mossbauer effect we will confine ourselves to indicate the characteristic properties of this spectroscopy.

The most outstanding feature of recoilless emission or absorption is the fact that the linewidth is determined only by the lifetime of the nuclear state involved. The linewidth (ΔE) of the more common Mossbauer transitions is of the order of 10^{-7} eV. As the energy (E) of the transitions is of the order of 10^4 to 10^5 eV the value of $Q = E/\Delta E$ is 10^{11} to 10^{12}. Therefore it is possible to measure very small shifts and splittings of the nuclear levels, which are due to hyperfine interactions.

Another typical aspect of Mossbauer spectroscopy is the use of the Doppler effect the source is given a velocity v with respect to the absorber and the energy of the emitted radiation E_γ, as 'seen' by the absorber is then given by

$$E(v) = (1 + \frac{v}{c}) E_\gamma \quad , \tag{1.1}$$

where c is the velocity of light. Energy differences are therefore expressed in terms of the Doppler velocity. Conversion factors for energy units are given in Table 1.1.

A third aspect concerns the probability of recoilless emission or absorption (the Mossbauer fraction), which is related to the vibrational amplitude of the nucleus. Thus the intensity of a Mossbauer absorption gives information on the dynamics of the emitting and absorbing nuclei.

The most popular Mossbauer nuclei are ^{57}Fe and ^{119}Sn. Both have a small linewidth and a large Mossbauer fraction. Moreover the parent nuclei, which populate the excited state have a long lifetime and sources can be used for over one year. The investigations, described in this thesis, are concerned with the Mossbauer effect in ^{197}Au. The energy of the nuclear transition is rather high (77 keV, see Table 1.1) and consequently the Mossbauer fraction is appreciable only at very low temperatures. Furthermore the parent nucleus (^{197}Pt) has a half life of 18 hrs and sources can be used for a few days only.

Nevertheless we undertook this investigation because, once available, the
technique can be readily applied to all gold containing substances in order
to study the hyperfine interactions, which contain a large amount of in-
formation on the chemical environment of the Mössbauer nucleus. These hyper-
fine effects on gold cannot be measured by other techniques like Electron
Spin Resonance (ESR) or Nuclear Magnetic Resonance (NMR), except in a few
special cases. Further, the source of ^{197}Au in Pt exhibits the natural line-
width, not broadened by small hyperfine effects, in contrast with iron and
tin sources. This makes it less complicated to determine absolute Mössbauer
fractions.

The next chapter of this thesis deals with the experimental techniques.
A detection method is described, developed to obtain short measuring times.
Chapter 3 and 4 summarize the theory and formulas used throughout the in-
vestigations and treat the analysis of the measured spectra. The results of
our measurements are reported in the following chapters: chapter 5 deals with
hyperfine interactions in diamagnetic gold compounds, chapter 6 with the
dynamical behaviour of the gold atom in these compounds, chapter 7 with the
only paramagnetic compound of gold thusfar isolated in pure form and finally
in chapter 8 we report on our measurements on small particles of gold metal.

Table 1.1

Properties of the ^{197}Au Mössbauer nucleus [1]

natural isotopic abundance: 100%	Energy conversion table:
γ-ray energy E_γ = 77.345 keV	1 mm/sec =
half life excited state $t_{\frac{1}{2}}$ = 1.90 ns	
linewidth Γ_o = 2.401 × 10^{-7} eV	2.580 × 10^{-7} eV
internal conversion coefficient α = 4.30	4.133 × 10^{-26} Joule
maximum resonance cross section σ_o = 3.86 × 10^{-20} cm^2	2.081 × 10^{-3} cm^{-3}
nuclear quadrupole moment Q = 0.594 b	2.994 × 10^{-3} ^{o}K
ground state magnetic moment μ_g = 0.144865 μ_N	62.39 Mc/s
excited state magnetic moment μ_e = 0.417 μ_N	

[1] J.G. Stevens and V.E. Stevens, "Mössbauer Effect Data Index 1973", New York (1974).

CHAPTER 2

EXPERIMENTAL TECHNIQUES AND APPARATUS

Mossbauer spectrometry involves determination of the count-rate of
γ-rays emitted by a source after passing through an absorber. The count-rate
is measured as function of the velocity of the source relative to the
absorber. There exist a great variety of spectrometers and the technique is
continuously improved. We refer to the literature for a description of
various methods (see for instance Goldanskii and Herber [Go68] or Greenwood
and Gibb [Gr71] . In this investigation we have used a constant acceleration
spectrometer, in which the velocity of the source is changed linearly in
time. A brief description is given in the next section. On the succeeding
pages we will treat in more detail those parts that are typical for this
research.

Concurrent with the Mossbauer work we have performed magnetization
measurements, X-ray diffraction and an electron microscopic investigation,
which are described in the respective chapters.

2 1 Spectrometer

A schematic diagram of the spectrometer is given in Figure 2.1 to
illustrate the principles of operation. The heart of the spectrometer is a
velocity transducer of the Kankeleit-type [Ka64] with a sensitivity of 25
mV/(mm/sec) and a displacement of 0.25 mm/V(DC). Both coils are part of a
feedback system with a voltage gain of 3000 and a bandwidth of 0-150 Hz. Due
to the triangular shape of the reference signal, the source is swept twice
through its velocity range during one cycle. The two spectra obtained are
analysed independently.

The finite voltage gain and bandwidth of the feedback circuit result in
small deviations from the triangular velocity wave form. We have not bothered
too much about this non-linearity, because the actual velocity is measured
with high accuracy as described in section 2.4.

The velocity measurement and the γ-ray count-rate are stored simulta-
neously in the memory of a Nuclear Data (ND2200) multichannel analyser, each
in 512 channels per period. The system is operated at a frequency of $\sim$ 5 Hz.
Synchronization is established every period by means of a start pulse. The
channel advance pulses are interrupted during a short time around maximum
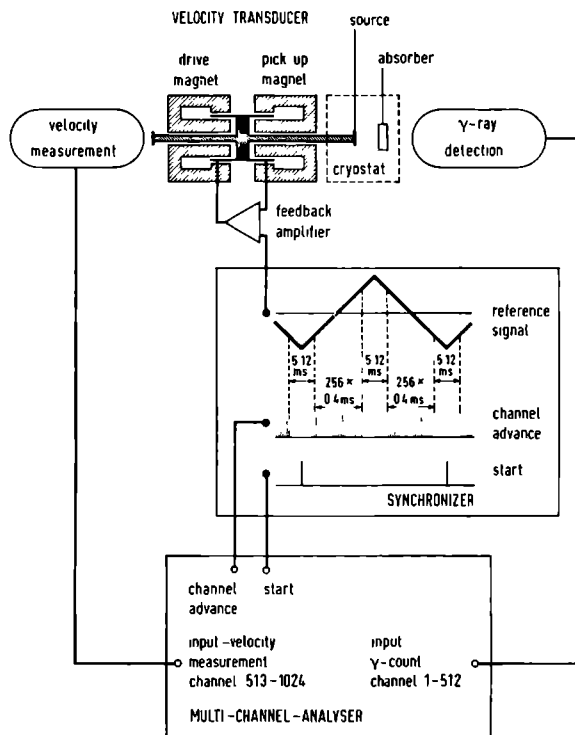
Figure 2.1 Schematic diagram of the Mössbauer spectrometer.

velocity, when the acceleration changes sign.

2.2 γ-ray source
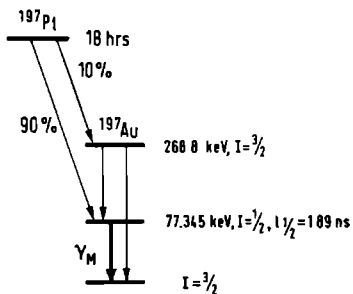
Figure 2.2 The γ-decay scheme of ^{197}Pt.

Table 2.1 Isotopic composition and calculated activities of the three sources after 24 hrs irradiation in a thermal neutron flux Φ.

150 mg natural platinum, $\Phi = 5 \times 10^{13}$ neutrons/cm^2/sec

composition		radioactive products		
isotope	relative abundance (%)	isotope	half life	activity (mCi)
192	0.8	193^m	4.3 d	1.50
194	32.9	195^m	4.1 d	2.90
195	33.8			
196	25.3	197	18 hrs	85.0
198	7.2	199(Au)	3.15 d	36.0

38 mg enriched in ^{196}Pt, $\Phi = 2 \times 10^{14}$ neutrons/cm^2/sec

composition		radioactive products		
isotope	relative abundance (%)	isotope	half life	activity (mCi)
194	8.91	195^m	4.1 d	0.8
195	33.46			
196	54.89	197	18 hrs	186.8
198	2.74	199(Au)	3.15 d	13.8

43 mg enriched in ^{196}Pt, $\Phi = 2 \times 10^{14}$ neutrons/cm^2/sec

composition		radioactive products		
isotope	relative abundance (%)	isotope	half life	activity (mCi)
194	13.76	195^m	4.1 d	1.4
195	38			
196	45.76	197	18 hrs	174.7
198	2.32	199(Au)	3.15 d	13.1

The radioactive nucleide ^{197}Pt, which is the parent nucleus for ^{197}Au (see Figure 2.2), is produced by thermal neutron capture of ^{196}Pt. Three sources have been used in these investigations: a 150 mg natural platinum disk, containing 25.3% of ^{196}Pt and two samples of 38 mg and 43 mg, enriched to 54.9% and 45.8% in ^{196}Pt respectively. They were send to the "Reactor Centrum Nederland" at Petten for a 24 hr irradiation in a flux of 5×10^{13} neutrons/cm^2/sec for natural platinum and 2×10^{14} neutrons/cm^2/sec for the
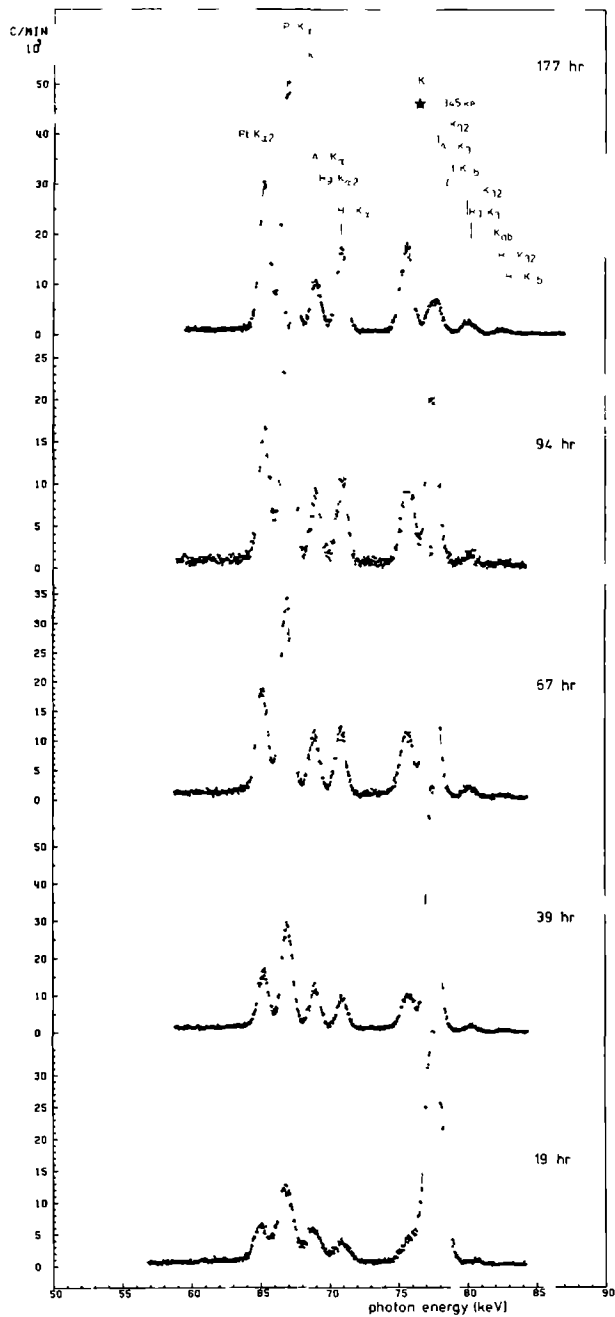
Figure 2.3a
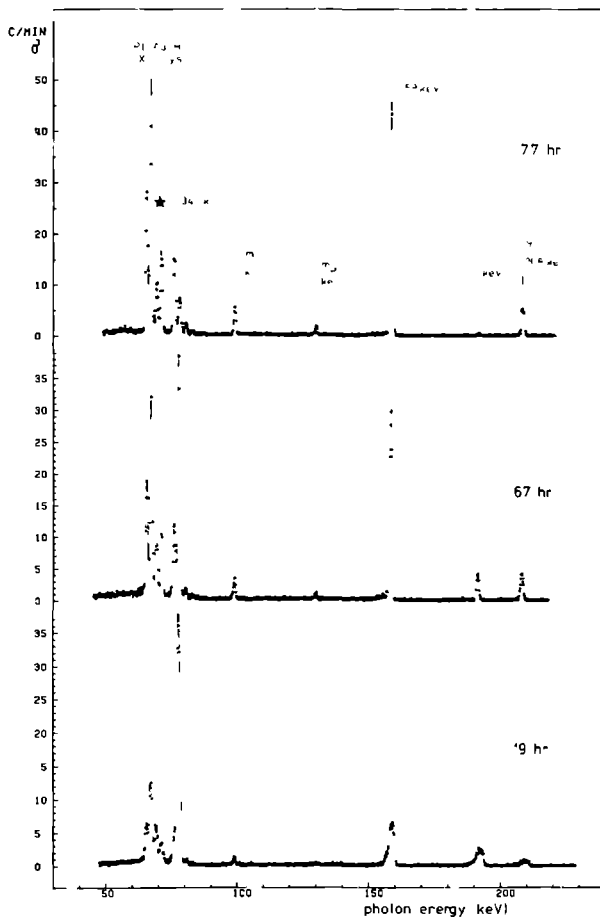
Figure 2.3   High resolution γ-spectra of the 38 mg. 54.9% ^{196}Pt source
              at different points of time from the moment, that the sample
              left the reactor. The spectra were measured with an intrinsic
              germanium solid state detector with an active area of 200 mm^2
              and a thickness of 10 mm (Princeton Gamma Tech IG210b). The
              high resolution could only be obtained with the source kept
              at a large distance from the detector to reduce the count-
              rate. Under the conditions of a Mössbauer experiment the X-
              rays are not resolved. The Mössbauer transition is indicated
              by an ★.

enriched samples. Apart from [197]Pt other isotopes are formed as well, the most important being [199]Au with a half life of 3.1 d. The isotopic composition of the samples is given in Table 2.1 together with calculated activities of radioactive isotopes at the end of the irradiation. The sources were installed in the spectrometer, without further treatment, approximately 19 hrs after leaving the reactor.

As can be seen in Table 2.1, [197]Pt has the shortest half life of all radioactive isotopes formed in the samples. This is illustrated in Figure 2.3a and 2.3b, which show γ-spectra of the 38 mg, 54.9% [196]Pt source at different time intervals after irradiation. At the time of installation of the source the Mössbauer transition clearly dominates over the X-ray radiation. After 3 days (4 half lives of [197]Pt) the measurements are stopped, because the relative intensity has become too small. A few weeks later, when the [199]Au activity has also disappeared, the sample could be irradiated again.

In the 38 mg, 55.9% [196]Pt sample a trace impurity of ^{192}Ir has been found, which has a half life of 74 days and is formed in the reaction [191]Ir (n,γ) [192]Ir. [191]Ir has a relatively large cross section for thermal neutron capture of 750 barn, to be compared with 0.9 barn for [196]Pt. Because of the long half life of ^{192}Ir there is a build up of activity every time the sample is irradiated.

2 3 Absorber preparation

All measurements on gold compounds were made on powdered crystals. The samples were carefully grounded to minimize the possibility of a preferential orientation of tne crystallites. The compounds were pressed in lucite containers with an inner diameter of 12 mm and a thickness upto 5 mm, depending of the amount of material available and on the specific weight.

2 4 Cryostat and insert

The cryostat is a three-wall metal dewar, shown in Figure 2.4. The bottom of the helium vessel and the outer vacuum can have been provided with aluminized mylar windows.

Source and absorber are contained in an insert, consisting of an 1" diameter thin walled stainless steel tube, which can be evacuated or filled with an exchange gas. The velocity transducer has been mounted in the upper part of the insert at room temperature. On top of the insert, outside the

8

photodiode
diverging lens
beam splitter

adjustable
  stationary mirror
moving mirror

transducer in vacuum

transducer extension rod

evacuation valve

vacuum seals

radiation shield

sample exchange lock

lock gate

lock valve

helium
return line

nitrogen
filling tube

helium filling tube

thermal radiation
  shields
evacuation

nitrogen reservoir

vacuum

helium reservoir

removable
source and absorber
  housing

drawer

mylar windows

γ-ray detection

Figure 2.4 Stainless steel dewar with insert for experiments where both source and absorber are cooled. This arrangement has been designed to change the sample without breaking the vacuum or warming up the cryostat. Using different tail-sections it can be operated in the range $1.2^{o}K < T < 100^{o}K$.

vacuum region, a Michelson-type interferometer has been placed for absolute velocity measurements, described in section 2.5. To drive the source we use a transducer extension rod, made from a ½" diameter thin walled stainless steel tube. At the lower end of the insert the extension rod is held in place by a phosphor-bronze leaf spring, electroplated with 50 μ of copper, which serves also as a thermal connection with the helium bath.

electrical leads

transducer
    extension rod

leaf spring

guide pin

electrical contact

Indium groove

thermal radiation
    shield

stainless steel
    absorber support

Germanium thermometer

absorber holder
heater coil
mylar window

drawer

source holder
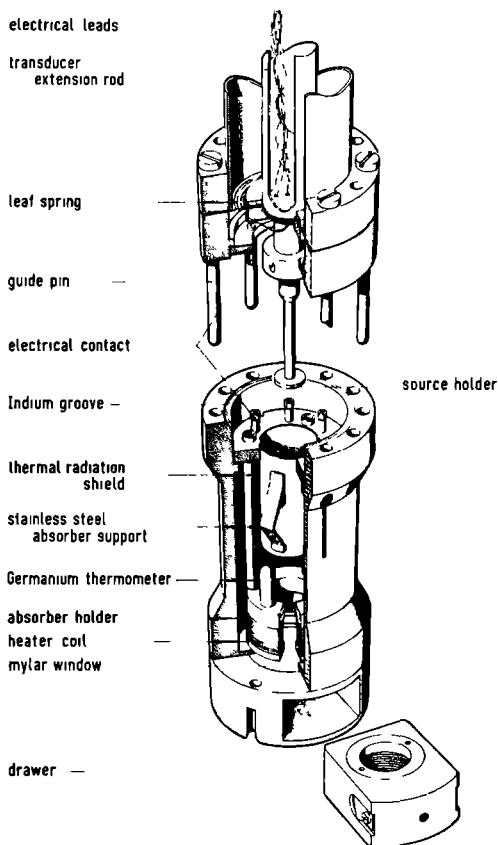
Figure 2.5 *Tail-section of the insert. The source is kept at bath temperature by a heat sink through the centre spring and is thermally shielded from the absorber. The absorber can be either put in a drawer outside the vacuum in direct contact with the coolant liquid or inside the vacuum where it can be heated to approximately $100^{o}K$.*

This system has a great versatility, because at the end of the insert various tail-sections can be mounted. For our experiments, which involve short lived sources with a high initial activity, it is necessary to mount the source and absorbers quickly and easily. Figure 2.5 shows the tail-section designed for measurements at temperatures between 1.2^OK and 100^OK.

Vacuum grease (Apiezon N) is used to glue the source to an aluminium source holder, which is subsequently mounted at the end of the transducer extension rod. The upper part of the insert is then lowered on the tail-section, which has been placed in the lead shielded lock on top of the cryostat. Guide pens align both parts, so that electrical connections are made by six gold-plated contacts. The two parts are bolted together with stainless steel screws and an indium ring provides the vacuum seal.

For measurements at 4.2^OK or lower the absorber is mounted in a drawer outside the vacuum region in direct contact with the coolant liquid. To change the sample the insert is pulled out of the helium bath until the tail-section reaches the sample exchange lock, where the valve is closed and the drawer pulled out. Then another drawer is pushed in, the valve is re-opened and the insert is lowered in its original position. This whole operation is executed in less than 5 minutes and consumes about 150 cm^3 liquid helium. The helium vessel has a capacity of 5 liters and a consumption of approximately 100 cm^3/hr when full, decreasing to 40 cm^3/hr when almost empty.

For temperature dependent measurements above 4.2^OK the absorber is wrapped in aluminium foil to minimize temperature differences over the sample. The absorber is then mounted inside the evacuated region where it can be heated with a heater coil. A copper cylinder with aluminium bottom, anchored at 4.2^OK, provides a thermal shielding of the source. The temperature of the absorber is measured with a germanium sensor and regulated with a BOC model 3010 temperature controller. Stabilization better than 0.05^OK could be obtained. When the vacuum conditions of the insert are optimal ($< 10^{-5}$ torr) the heater power is 0.9 mWatt/^{O}K (1 mWatt corresponds with the evaporation heat of 1.38 cm^3/hr helium at 4.2^OK). There is a heat inleak of 6.5 mWatt mainly through the electrical leads, which run through the push-rod from the room temperature region. As a result of the heat inleak the lowest absorber temperature is 12^OK. For lower temperatures the insert is filled with exchange gas.

2.5 Absolute velocity measurements

a. The method

The velocity is measured with a high accuracy using a Michelson inter-
ferometer with a He-Ne laser as described by Fritz and Schulze [Fr68] (see
Figure 2.4). One mirror of the interferometer is fixed, the other is mounted
on the velocity transducer. The intensity at the light-detector depends on
the position x of the moving mirror:

$$I \propto \sin 2\pi \frac{x}{\frac{1}{2}\lambda} \quad , \qquad\qquad\qquad (2.1)$$

where λ is the wavelength of the radiation. Thus every time the mirror travels
$\frac{1}{2}\lambda$ the intensity changes from bright to dark. With $\lambda = 6328$ Å one obtains a
frequency of 3164 Hz, when the velocity of the moving mirror is 1 mm/sec.

The laser beam is made divergent with a small negative lens at the
entrance of the interferometer. The wave front is then no longer flat, so that
instead of a single spot, which varies in intensity, there arise circular
interference fringes. This makes the adjustment of the interferometer easier.
Another advantage of this lens is the elimination of undesired harmonics on
the intensity due to reflection on the exit mirror of the laser, as discussed
by Cranshaw [Cr73]. A circuit diagram of the light-detector with amplifier
is shown in Figure 2.6[*]. The intensity of the light is measured with a fast
photodiode, amplified and subsequently shaped into a logical signal, which
gives a pulse every time a light fringe passes the photodiode. The DC level
of the amplifier is automatically adjusted by feedback of the signal with a
large (10 sec) time constant. The pulses, corresponding with the passage of
the interference fringes over the detector, are counted in the multichannel
analyser. The average velocity $\bar{v}_i$ during the dwell time Δt_i in channel number
i can be calculated from the channel contents n_i:

$$\bar{v}_i = \frac{n_i \lambda}{2N\Delta t_i} \quad , \qquad\qquad\qquad (2.2)$$

where N is the number of passes through the velocity range.

[*] designed by H.W. Neijenhuisen

12

Figure 2.6   Circuit diagram of the light-detector

Random errors originate from vibrations of the interferometer with
respect to the velocity transducer. They average out in time except for small
velocities, where the amplitude of the vibration is larger than the distance
travelled by the moving mirror during the dwell time of one channel. In that
case one obtains always a positive contribution from the noise, because only
the absolute value of the velocity is measured. In practice this occurs
around zero velocity in less than 2% of the total velocity range.

Systematic errors are caused by misalignment of the interferometer. In
that case the measurements are carried out under an angle α with the direction
of the velocity, introducing a factor cos α. This error can easily be kept
below 0.05%.

b. Processing of the measurements

From the contents of each channel the velocity is calculated with Eq. 2.2.
As only the absolute value of the velocity is measured the appropriate sign is
added in the calculation. The measured $\bar{v}_i$ are fitted with a polynomial of up
to eight degree, leaving out the measurements around zero velocity. In
analysing the Mössbauer spectra the polynomial coefficients are used to
calculate the velocity corresponding with each channel number.

13

velocity

256 channels

second half

horizontal deviation
from linearity

horizontal deviation
from linearity

first half

256 channels

Figure 2.7   ---- ideal velocity wave form ——— actual velocity wave form.
Indicated (not at scale) is the deviation from linearity,
which is plotted in Figure 2.8.

deviation from linearity
(channel units)

20

10

00   50   100   150   200   250

-10

-20

first half

-30

50   100   150   200   250

second half

Figure 2.8   Deviation from linearity. The drawn curve is a least squares
polynomial of degree 7. A higher degree does not substantially
improve the fit.

14

To judge the goodness of fit and the operation of the drive system we plot the horizontal deviation from linearity, expressed in the number of channels, as function of the channel number. This procedure is illustrated in Figure 2.7. Figure 2.8 shows a typical example of the deviation from linearity. This deviation proved to be practically independent of the velocity range. Small oscillations with an amplitude of about 0.05 channels and a period of approximately 20 channels can be observed in Figure 2.8. The origin of these oscillations is not well understood in particular because they cannot be seen on the signal of the pick-up coil.

The performance of the velocity measurement is probably best illustrated by the ratio of the magnetic moments of ^{57}Fe for the excited state ($\mu^{\star}$) and the ground state (μ). We obtained for the Mossbauer spectrum of iron:

$$\mu^{\star}/\mu = 1.712 \pm 0.003 \quad ,$$

which corresponds well with the value of 1.715 ± 0.004 obtained by Preston, Hanna and Heberle [Pr62].

2 6 γ-ray detection

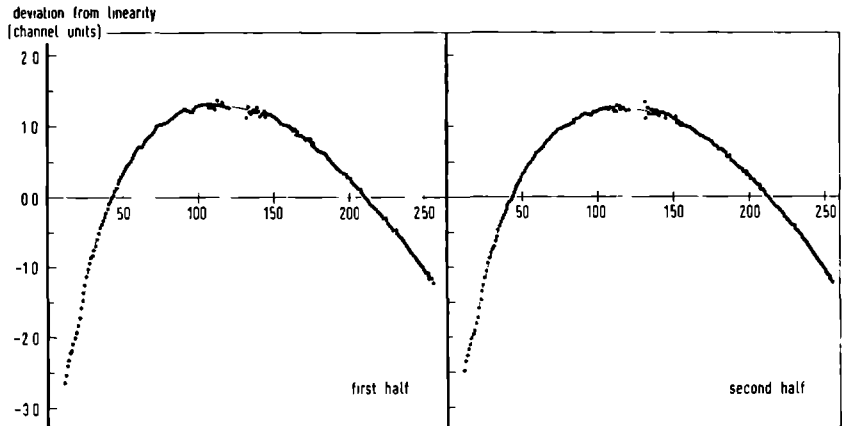Our first measurements were carried out with a conventional detection system, using a 1" thick NaI(Tl) scintillation detector. The detector pulses are amplified and fed to a single channel analyser, which selects those pulses that correspond with an adjustable energy range in the γ-spectrum (Figure 2.9). The optimal position and width of the energy window was determined from the requirement that a maximal signal to noise ratio should be obtained in the shortest time. -It should be noted, that this requirement does not necessarily lead to a maximum absorption depth.- The statistical variance equals the square root of the number of counts n, whereas the amount of signal is a constant factor α of n. Thus the signal to noise ratio R is given by:

$$R = \alpha \quad n$$
$$= \alpha \quad C.t \quad , \tag{2.3}$$

where C is the count-rate and t the measuring time.
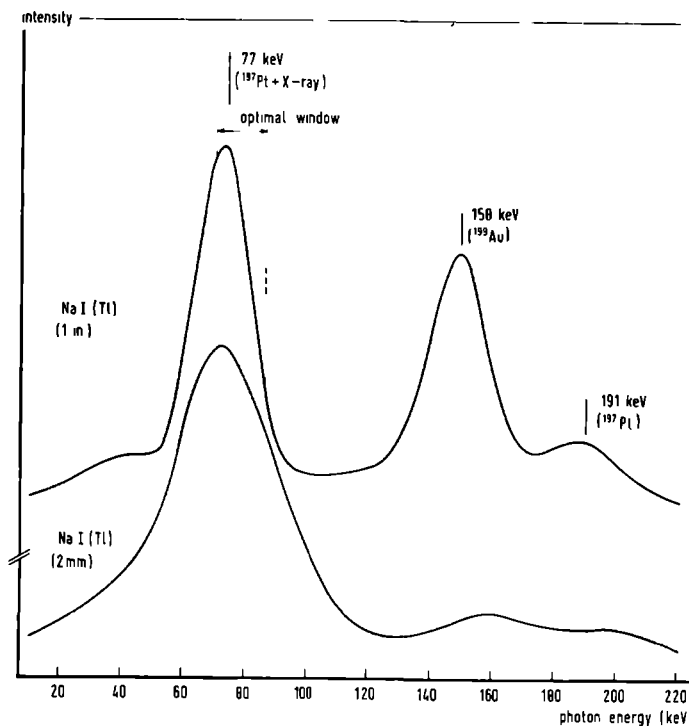
*Figure 2.9   γ-spectra of 150 mg natural platinum activated for 24 hrs
in a thermal neutron flux of 5 × 10^13 neutrons/cm²/sec.
The two spectra were observed two days after the sample
was removed from the reactor, (1) with a 1" thick and (2)
with a 2 mm thick NaI(Tl) scintillation detector. Although
the resolution can be improved by lowering the count rate,
a NaI(Tl) detector does not resolve the Mossbauer transition
from the X-rays (compare with Figure 2.3). The lower
efficiency for the higher energy γ-rays in case of a thin
scintillation crystal is evident.*

Within the selected energy range we obtained a count-rate of 10^4 counts/
sec and for a 136 mg/cm² gold foil a maximum absorption depth of about 4%.
This means that the measuring time to obtain a signal to noise ratio of 50 is
3.5 min per channel, or 15 hrs, when 256 channels are used. This long
measuring time is due to the limited count-rate, that can be handled by
linear pulse amplifiers, whereas the count-rate in the detector is orders of

magnitude higher.

It has been suggested by Mossbauer [Mo72] that to overcome this limitation integrating methods could be used, when the Mössbauer transition is > 150 keV and such a method has actually been applied in measurements on Osmium [Wa75] and Zinc [Be71]. We have successfully applied an integrating technique to the detection of the 77 keV [197]Au Mössbauer transition using a thin scintillation detector [Vi74]. In Figure 2.10 a diagram is given for
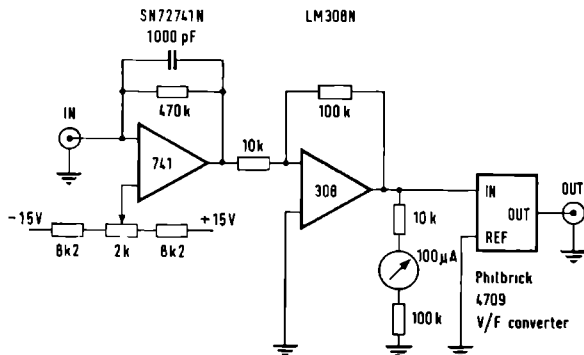
Figure 2.10   Circuit diagram of the integrating counting technique.

the integrating counting technique as applied by us. The photomultiplier current is integrated with a time constant equal to the dwell time per channel (400 μsec) and the output of the integrator is digitized by means of a voltage to frequency converter. The output pulses of the converter are then counted in the usual way. The photomultiplier gain and the DC level of the integrator are adjusted in such a way that the AC amplitude of the signal is only slightly less than the range of the voltage to frequency converter. The additional variance due to digitalization is then negligible.

With this integrating counting method full advantage can be taken of the high source activity. On the other hand the relative Mossbauer absorption is decreased because no discrimination other than the efficiency of the detector is made against other radiation. As can be seen from Eq. 2.3 the factor, by which the count-rate is increased, must be larger than the square of the factor, by which the relative absorption intensity becomes smaller, in order to obtain a reduction of the measuring time. In our case the decrease of the relative absorption intensity could be limited to a factor 2, using a thin

(2 mm) scintillation crystal, which has low efficiency for the high energy γ-rays (compare Figure 2.9).

The time required to obtain a signal to noise ratio of 50 with a fresh source, made from natural platinum, and the 135 mg/cm^2 gold foil was 3.4 min or 0.8 sec per channel. The spectrum is shown in Figure 2.11. Here the noise is defined as

$$N = \{\frac{1}{256} \sum_{i=1}^{256} [Y_m(i) - Y_c(i)]^2\}^{\frac{1}{2}} \quad , \tag{2.4}$$

$Y_m(i)$ and $Y_c(i)$ are the measured and least square fitted intensities in channel i, respectively. Signal is the peak intensity. Conventional pulse counting techniques would require 4×10^6 counts/sec to obtain for the same relative absorption intensity the signal to noise ratio of Figure 2.11.
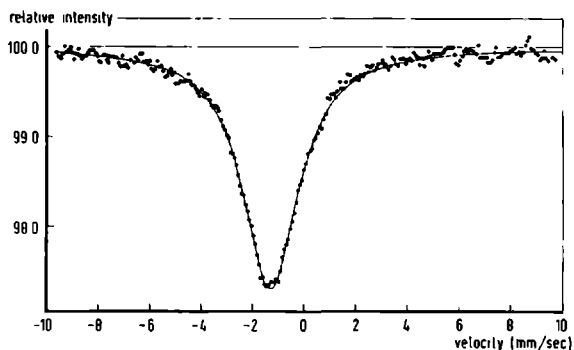
Figure 2.11 *Mössbauer spectrum of a 135 mg/cm^2 gold foil at 4.2^{o}K, obtained in 3.4 min or 0.8 sec per point. The drawn line is a least-square-fitted Lorentzian.*

Because of the decreasing contribution of Mössbauer radiation to the detector current the relative intensity is reduced with ageing of the source. Thus three days after the end of the irradiation the relative intensity was 1% and the signal to noise ratio obtained in 3.4 min was 10.

The conclusion is that the effective count-rate is increased two orders of magnitude and the reduction of the measuring time is a factor 25.

Recently Kankeleit has given a thorough discussion of the application of current integration methods [Ka75]. In his paper Kankeleit reports on experiments, which indicate long recovery times of the detectors. In our experiments the intensities and intensity variations of the radiation are considerably lower than in Kankeleits experiments and no adverse effects could be detected in the Mössbauer spectra. Minor differences were observed between three thin crystal NaI(Tl) scintillation detectors (see Table 2.2).

Table 2.2 *Signal to noise ratio, obtained with different scintillation detectors under the same circumstances.*

Scintillation X-tal thickness	diameter	Photomultiplier	Signal to noise ratio
2 mm	50 mm	Philips AVP 153	3.80
1 mm	50 mm	EMI-9656 KA	3.60
1 mm	25 mm	EMI-9524 KA	3.85

It has been argued [Ka75] that the integration technique introduces other sources of variance resulting from the low pass (DC) coupling of the detector. All drifts in the system will contribute to it. We observed sometimes oscillations on the spectrum (see for instance Figure 2.11), which did not average out in several hours. This can be due to a burst of low frequency noise, which occurs once during the measurement. On the other hand the frequency is comparable with the oscillation observed on the velocity (section 2.5). In that case there has to be some coupling with the drive motion, although the oscillations have not been observed on the pick-up signal. This effect requires a more detailed investigation.

2.7 Determination of the background level

A general expression for the transmitted γ-ray intensity $I(v)$, measured as function of the velocity v is:

$$I(v) = I_b(v) \, [\, 1 - L(v) \,] + I_d \quad , \tag{2.5}$$

where $I_b(v)$ is the intensity without Mössbauer absorption and $L(v)$ the relative resonant absorption lineshape, determined by the characteristic

19

properties of source and absorber. I_d is an arbitrary constant, introduced by the integrating counting method. As v is a function of time t, we may replace v by t in Eq. 2.5.

The baseline of the spectrum, $I_b(t)$, is velocity dependent, because the solid angle Ω, under which the radiation is detected, varies with the position of the source:

$$I_b(t) \propto \Omega(t) \quad . \tag{2.6}$$

If x_o is the equilibrium distance between source and collimator, $x(t)$ the displacement of the source from the equilibrium position and D the area of the collimator, we have:

$$\Omega(t) = \frac{D}{4\pi \, [x_o - x(t)]^2}$$

$$= \frac{D}{4\pi x_o} [1 - \frac{2x(t)}{x_o}] \quad (x(t) \ll x_o)$$

$$= \Omega_o \, [1 - \Delta(t) \,] \tag{2.7}$$

The last equal sign defines Ω_o and the relative solid angle variation $\Delta(t)$. With Eq. 2.6 we obtain for the baseline:

$$I_b(t) = I_o \, [1 - \Delta(t) \,] \quad . \tag{2.8}$$

Hence Eq. 2.5 becomes:

$$I(t) = I_o \, [1 - \Delta(t) \,] \, [1 - L(t) \,] + I_d \quad . \tag{2.9}$$

If $\Delta(t) \ll 1$ and $L(t) \ll 1$, $I(t)$ can be approximated by:

$$I(t) = I_o \, [1 - \Delta(t) - L(t) \,] + I_d$$

$$= [I_o + I_d] - I_o \Delta(t) - I_o L(t) \quad . \tag{2.10}$$

20

To determine the true relative absorption intensity from I(t) the so-called background level I_o should be known, whereas $[I_o + I_d]$ is measured. The value of I_d depends on the dark current of the photomultiplier, the potentiometer settings of the integrator and the conversion rate of the voltage to frequency converter, which are all parameters that in principle can be measured. However, it proved easier to determine the relative absorption intensity from a comparison with the baseline curvature, the more so as for long measurements the DC level of the integrator output is re-adjusted several times during the acquisition of a spectrum to compensate for the ageing of the source.

In one period T the source is swept with a constant acceleration from a maximum velocity v_{max} to a minimum velocity $-v_{max}$ and subsequently in the opposite direction when the acceleration has changed sign. Disregarding deviations from linearity, the displacement x(t) has a parabolic shape:

$$x(t) = v_{max} [t - \frac{2}{T} t^2] \quad (0 \leqslant t \leqslant \frac{1}{2} T) \quad . \tag{2.11}$$

The expression for $\frac{1}{2} T \leqslant t \leqslant T$ is similar, but with negative sign. Substitution of x(t) of Eq. 2.11 in the expression for $\Delta(t)$ of Eq. 2.7 yields:

$$\Delta(t) = \frac{2v_{max}}{x_o} [t - \frac{2}{T} t^2] \quad . \tag{2.12}$$

Using $\Delta(t)$ of Eq. 2.12 we obtain from Eq. 2.10 after integration:

$$\int_0^{\frac{1}{2} T} I(t) dt = [I_o + I_d] \cdot \frac{1}{2} T - I_o \frac{v_{max} T^2}{12 x_o} - I_o \int_0^{\frac{1}{2} T} L(t) dt \;, \tag{2.13a}$$

and

$$\int_{\frac{1}{2} T}^T I(t) dt = [I_o + I_d] \cdot \frac{1}{2} T + I_o \frac{v_{max} T^2}{12 x_o} - I_o \int_{\frac{1}{2} T}^T L(t) dt \;. \tag{2.13b}$$

Because in both half periods L(t) is the same, substraction of Eq. 2.13a and Eq. 2.13b yields:

$$\int_{\frac{1}{2}T}^{T} I(t)\,dt - \int_{0}^{\frac{1}{2}T} I(t)\,dt = I_o \frac{v_{max} T^2}{6x_o} \quad . \qquad (2.14)$$

As all constants, except I_o, in this equation are known, I_o can be determined and thus also I_d. In practice Eq. 2.14 has to be modified, because the intensity is measured during a period smaller than $\frac{1}{2}T$. The integrations are carried out by summing the channel contents of the first and second half and T is correspondingly adjusted.

The spectrum of Figure 2.11 may serve as a typical example: v_{max} was 9.35 mm/sec, x_o was 112 mm and $\frac{1}{2}T$ was 0.1024 sec (the time required for 256 channels with a dwell time of 0.4 msec each), so that the maximum value of $\Delta(t)$ was 0.427%, which is about one fifth of the absorption depth of the gold foil.

Once I_o is known, Eq. 2.11 can be used to remove the baseline curvature. However, we preferred to determine $\Delta(t)$ experimentally by measuring a blank "spectrum" B(t) without absorber for each series of measurements with one source:

$$B(t) = B_o [1 + \Delta(t)] + B_d \quad . \qquad (2.15)$$

B(t) is subsequently fitted with a parabola and this parabola is used to remove the baseline curvature from the measured spectrum. Source collimator misalignment and non-linearity of the velocity is in this way accounted for.

For the execution of this procedure we developed a computer code, which requires as input: the measured spectrum I(v), the measured blank baseline B(v) and the values of v_{max}, x_o and T. The resulting spectrum I'(v):

$$I'(v) = I_o [1 - L(v)] \quad , \qquad (2.16)$$

is stored on a direct access data storage device for subsequent analysis.

2 8 Application of an external magnetic field

For a few measurements an external magnetic field was applied with a superconducting solenoid placed at the bottom of the helium vessel (not shown

in Figure 2.3). We used a 60 kOe magnet with 38 mm bore. A zero field region for the source is located at 72 mm above the maximum field region, where the absorber is situated. A longer tail-section of the insert is then used to fulfil the requirements for source-absorber distance.

The photomultiplier tube was placed outside the influence of the magnet using a bend light-pipe made of a 5 cm diameter lucite rod with a length of 2 m. At one end the 2 mm thick scintillation crystal was mounted and at the other end the photomultiplier tube. The gain and resolution of this detector were smaller by a factor of about 4 compared to measurements without light-pipe. However, this did not significantly influence the measurements, when the integrating counting technique was used.

CHAPTER 3

THE PARAMETERS OF A MOSSBAUER SPECTRUM

As pointed out in chapter 1, the Mossbauer effect has a very high energy resolution. Due to this resolution one is able to measure small shifts and splittings of the nuclear energy levels, caused by the interaction of the nucleus with its environment. The theory that describes the nuclear level splitting is also used in connection with other resonance techniques like Nuclear Magnetic Resonance, Electron Spin Resonance and Quadrupole Resonance, and can be found in many textbooks (see for instance Abragam [Ab61]). Apart from this the Mössbauer effect gives also information on the dynamics of the motion of the emitting and absorbing nuclei in solid bodies.

As an introduction to the discussion of the experimental results, we briefly describe in the next section three lower order terms in the multipole expansion of the hyperfine interaction energy, namely the electric monopole, the electric quadrupole and the magnetic dipole interaction. Higher order terms are usually negligible. The relative intensities of the transitions between the various nuclear levels are treated in the subsequent section. In the last section of this chapter we shall deal with the parameters of the Mössbauer spectrum, which depend on the dynamical behaviour of the resonating atoms in the solid. Much of the contents of this chapter can be found in reviews of the Mössbauer effect [Ab64,Go68,Gr71,We64,We65].

3 1 Nuclear level splitting

The energy of the nuclear levels depends on the surroundings of the nucleus. The rotational degeneracy of these levels can be lifted when the symmetry of the environment is low enough. In the formulas, describing the energy of the nuclear levels, the electronic and solid state surroundings of the nucleus occur as parameters, which are essentially the subject of this study and will be discussed in some detail.

a Isomer shift

As described in the introduction the Mossbauer transition is a nuclear transition, in which the kinetic and electronic state of the atoms is not altered. Thus the Coulomb interaction of the nucleus with the surrounding

electrons is not measured. However, the finite nuclear radius R can result in a different transition energy for two samples, if the radius of the nucleus is different for the two nuclear states involved and if both samples have a different chemical surrounding. The resulting shift, known as the Isomer Shift δ, is given by:

$$\delta = E_a - E_s = \frac{2}{5} \pi Ze^2 (R_e^2 - R_g^2) [|\Psi_a(0)|^2 - |\Psi_s(0)|^2] \quad , \quad (3.1)$$

where a and s refer to absorber and source and e and g to the nuclear excited state and ground state, respectively. Ze is the nuclear charge and $|\Psi(0)|^2$ the electron density at the site of the nucleus. With the approximation $(R_e^2 - R_g^2) = 2R\Delta R$, where $\Delta R = R_e - R_g$, we obtain

$$\delta = \frac{4}{5} \pi Ze^2 R^2 (\Delta R/R) [|\Psi_a(0)|^2 - |\Psi_s(0)|^2] \quad , \quad (3.2)$$

$(\Delta R/R)$ is called the nuclear factor.

The Isomer Shift, as measured, gives information on the difference in the electron density at the nucleus between source and absorber. Generally, however, δ is quoted with respect to some arbitrary chosen compound. In case of gold it has become practice to give δ with respect to the source of ^{197}Au in platinum.

s-Electrons have a non-zero $|\Psi(0)|^2$. However, other electrons influence the Isomer Shift through screening. By relativistic effects, in particular for large values of Z, also $p_{\frac{1}{2}}$-electrons possess a non-zero wavefunction at the nucleus.

b. **Quadrupole interaction**

The second correction to the electrostatic interaction between the nucleus and its surroundings is due to the non-spherical charge distribution within the nucleus. The Hamiltonian for this quadrupole interaction can be written as:

$$\mathcal{H}_Q = \vec{I}.\bar{\bar{P}}.\vec{I} \quad , \quad (3.3)$$

25

where $\bar{\bar{P}}$ is a traceless tensor of the second rank, the components of which are given by:

$$P_{ij} = \frac{eQ}{2I(2I-1)} \, V_{ij} \quad . \tag{3.4}$$

Q is the nuclear quadrupole moment, I the nuclear spin quantum number and V_{ij} is an element of the electric field gradient tensor, the components of which are the second derivatives with respect to the coordinates x_i and x_j of the electrostatic potential V at the nucleus

$$V_{ij} = \frac{\partial V}{\partial x_i \partial x_j} \quad . \tag{3.5}$$

If we choose the coordinate system along the principal axes of the electric field gradient the expression for $\mathcal{H}_Q$ is:

$$\mathcal{H}_Q = \frac{eV_{zz}Q}{4I(2I-1)} \, \{3I_z^2 - \vec{I}^2 + \frac{1}{2} \, \eta \, (I_+^2 + I_-^2)\} \quad , \tag{3.6}$$

where $\eta = (V_{xx} - V_{yy})/V_{zz}$. The energy level splitting resulting from $\mathcal{H}_Q$ is shown in Figure 3.1.

The levels of the excited state remain unchanged since $I = \frac{1}{2}$ and $Q = 0$, in contrast with the ground state, where $I = \frac{3}{2}$ and the splitting is given by:

$$2\varepsilon = \frac{1}{2} \, eV_{zz}Q \, \sqrt{1 + \frac{\eta^2}{3}} \quad , \tag{3.7}$$

with the eigenfunctions:

$$|+> = \cos \vartheta \, |3/2, \pm 3/2 > + \sin \vartheta \, |3/2, \mp 1/2 > \quad , \tag{3.8a}$$

$$|-> = \sin \vartheta \, |3/2, \pm 3/2 > - \sin \vartheta \, |3/2, \mp 1/2 > \quad , \tag{3.8b}$$

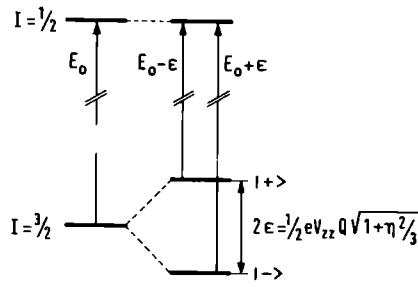where $\tan 2\vartheta = \sqrt{\frac{\eta^2}{3}}$ \hfill (3.9)

26

*Figure 3.1 Due to the electric quadrupole interaction
the fourfold degeneracy of the nuclear ground
state of ^{197}Au is partly removed.*

In the calculation of V_{ij} at a nucleus in the origin of a cartesian coordinate
system, it is useful to distinguish between the electric field gradient
caused by the atomic electrons and the charges in the lattice:

$$V_{ij} = \frac{e}{4\pi\epsilon_o} \left[(1-\gamma) \sum_{K} z^{K}_{eff} \left\{ \frac{3x^{K}_{i}x^{K}_{j} - |\vec{R}^{K}|^2}{|\vec{R}^{K}|^5} \right\} \right. , \tag{3.10a}$$

$$\left. -(1-R) \frac{<\Psi| \sum_{k} \frac{3x^{k}_{i}x^{k}_{j} - |\vec{r}^{k}|^2}{|\vec{r}^{k}|^5} |\Psi>}{<\Psi|\Psi>} \right] . \tag{3.10b}$$

Here ez^{K}_{eff} and $\vec{R}^{K}$ are the effective charge and the position vector of atom K.
x^{K}_{i} is the component of $\vec{R}^{K}$ along the i-axis. Ψ is an n-electron wavefunction
and the sum over k runs over all valence electrons at the atom. $\vec{r}^{k} = (x^{k}_{1},x^{k}_{2},x^{k}_{3})$
is the position of electron k. R and γ are the so-called Sternheimer [St50]
(anti-)shielding factors. These account for small induced distortions from
spherical symmetry of the inner shell electrons, that are not included in the
summation over k.

In many cases (e.g. a closed shell configuration or a configuration with
the highest spin multiplicity) a good approximation to Ψ is a single deter-
minant constructed from one-electron spin orbitals ψ_{k}:

$$\Psi = \sqrt{\frac{1}{n!}} \; \det \; |\psi_1(1) \ldots \psi_n(n)| \qquad (3.11)$$

When the set ψ_k is chosen to be orthonormal, Eq. 3.10b reduces to the sum of one-electron contributions and one obtains for instance for the diagonal components of $\bar{\bar{V}}$:

$$V_{11} = \sum_k V_{11}^k = \frac{-e}{4\pi\varepsilon_o} \sum_k \; < \psi_k \left| \frac{3\cos^2\theta_1 - 1}{|\vec{r}|^3} \right| \psi_k > (1-R) \qquad , \qquad (3.12)$$

where $\cos\theta_1$ are the direction cosini of $\vec{r}$. We now write ψ as:

$$\psi = R(r) Y_{lm}(\theta,\phi) \sigma \qquad , \qquad (3.13)$$

where $R(r)$ is the radial part, Y_{lm} is a spherical harmonic and σ the spin function. V_{11}^k, which does not depend on σ, then becomes:

$$V_{11}^k = \frac{-e}{4\pi\varepsilon_o} < R^k(r) \left| \frac{1}{|\vec{r}|^3} \right| R^k(r) > < Y_{lm}^k \left| 3\cos^2\theta_1 - 1 \right| Y_{lm}^k > (1-R) \qquad .$$

$$(3.14)$$

The first factor, also written as $< r^{-3} >$, depends only on the radial part of the atomic wavefunction. The most reliable $< r^{-3} >$ values are nowadays obtained using numerical relativistic self-consistent field calculations. The angular part (second factor of Eq. 3.14) is zero for s-orbitals, as they have a spherical symmetry, and for the real p- and d-orbitals it is given in Table 3.1.

Table 3.1 Values of $< Y_{lm}(\theta,\phi) | 3\cos^2\theta_i - 1 | Y_{lm}(\theta,\phi) >$
for p- and d-orbitals.

	p_x	p_y	p_z	d_{xy}	d_{xz}	d_{yz}	d_{z^2}	$d_{x^2-y^2}$
V_{xx}	$-\frac{4}{5}$	$\frac{2}{5}$	$\frac{2}{5}$	$-\frac{2}{7}$	$-\frac{2}{7}$	$\frac{4}{7}$	$\frac{2}{7}$	$-\frac{2}{7}$
V_{yy}	$\frac{2}{5}$	$-\frac{4}{5}$	$\frac{2}{5}$	$-\frac{2}{7}$	$\frac{4}{7}$	$-\frac{2}{7}$	$\frac{2}{7}$	$-\frac{2}{7}$
V_{zz}	$\frac{2}{5}$	$\frac{2}{5}$	$-\frac{4}{5}$	$\frac{4}{7}$	$-\frac{2}{7}$	$-\frac{2}{7}$	$-\frac{4}{7}$	$\frac{4}{7}$

Even in highly ionic solids the valence electrons are delocalized over more atomic centres, which can be taken into account in several ways. For instance in the Valence Bond treatment covalent structures are introduced. In the molecular orbital (MO) theory the electrons occupy MO's, which are generally written as linear combinations of atomic orbitals (LCAO-MO). Both theories should yield the same results when extended to ultimate refinement, but there are differences on the level at which they are applied for a qualitative explanation of experimental observations [Co61]. On this level it is useful to express the delocalization (or covalency) in an effective covalency parameter λ, which is most easily done with the LCAO-MO method: two electrons, involved in a chemical bond, occupy a molecular orbital χ:

$$\chi = (1 - \lambda^2)^{-\frac{1}{2}} \Lambda + \lambda\phi \quad . \tag{3.15}$$

The corresponding empty anti-bonding MO is then given by:

$$\chi^* = (1 - \lambda^2)^{-\frac{1}{2}} \phi - \lambda\Lambda \quad . \tag{3.16}$$

ϕ is located on the central atom and Λ is a linear combination of atomic orbitals with the appropriate symmetry located on the nearest neighbours. The overlap integral $< \phi | \Lambda >$ is set equal to zero. Replacing ψ in Eq. 3.12 by χ of Eq. 3.15, we obtain, neglecting the two-centre integrals:

$$V_{ii} = - \frac{2e}{4\pi\varepsilon_o} \{ \frac{1}{(1-\lambda^2)} < \Lambda | q | \Lambda > + \lambda^2 < \phi | q | \phi > \} \quad , \tag{3.17}$$

with

$$q = (3\cos^2\theta - 1)/|\vec{r}|^3 \quad . \tag{3.18}$$

The factor 2 arises because χ is doubly occupied. If we make the approximation that the electrons in orbitals, centred at the neighbours, are concentrated on the neighbour nuclei, the first term in Eq. 3.17 can be lumped into the effective atomic charge Z_{eff} of Eq. 3.10a. From Eq. 3.17 it appears that the atomic contribution is reduced by a factor λ^2 due to covalency. It should be kept in mind that the value of the covalency parameter λ is based in part on the LCAO-MO approximation and on the neglect of all two-centre integrals.

The interaction of the nuclear magnetic dipole moment $g_N \beta_N \vec{I}$ with a magnetic hyperfine field $\vec{B}_{hf}$ is described by:

$$\mathcal{H}_M = - g_N \beta_N \vec{I}.\vec{B}_{hf} \quad , \tag{3.19}$$

where g_N and β_N are the nuclear g factor and magneton respectively. $\vec{B}_{hf}$ can be split up in three contributions: the dipole field, which for one electron with spin $\vec{S}$ is.

$$\vec{B}_D = \frac{\mu_o g\beta}{4\pi} \{ \frac{\vec{S}}{|\vec{r}|^3} - \frac{3\vec{r}.(\vec{S}.\vec{r})}{|\vec{r}|^5} \} \quad , \tag{3.20}$$

the orbital contribution, for one electron with angular momentum $\vec{L}$ given by:

$$\vec{B}_L = - \frac{\mu_o}{2\pi} \frac{\vec{L}}{|\vec{r}|^3} \quad , \tag{3.21}$$

and the Fermi contact term:

$$\vec{B}_{FC} = \frac{2\mu_o}{3} g \beta \rho_s(0) \vec{S} \quad , \tag{3.22}$$

where $\rho_s(0)$ is the spin density at the nucleus. g and β are the electronic g factor and Bohr magneton respectively and μ_o is the permeability of the vacuum.

Magnetic interactions on gold have been observed in the Mossbauer spectra of ^{197}Au in alloys [Pa70]. From these measurements the magnetic moment of the nuclear excited state was determined to be $\mu_e = 0.419 \ \mu_N$, the ground state magnetic moment is $\mu_g = 0.14486 \ \mu_N$.

In some cases it is more convenient to describe $\mathcal{H}_M$ with the spin hamiltonian [Ab70]:

$$\mathcal{H}_M = \vec{I}.\bar{\bar{A}}.\vec{S} \quad , \tag{3.23}$$

where $\vec{S}$ is the effective electron spin and $\bar{\bar{A}}$ the hyperfine coupling tensor. Comparison of Eq. 3.19 and Eq. 3.23 yields:

$$\vec{B}_{hf} = - \frac{\bar{\bar{A}}.\vec{S}}{g_N \beta_N} \quad .$$

(3.24)

In case of an isotropic hyperfine coupling Eq. 3.23 reduces to:

$$\mathcal{H}_M = a \; \vec{I}.\vec{S} \qquad ,$$

(3.25)

where a is the hyperfine coupling constant.

d. Fluctuating hyperfine fields

In the calculation of the energy level schemes in the preceding paragraphs it has been tacitly assumed that the hyperfine fields are constant on a time scale, which is determined by the characteristic frequency ω of the energy involved. For the electric field gradient this condition is practically always satisfied. But in paramagnetic substances the relaxation time of the electron spin varies widely. When τ is shorter than the Larmor period $1/\omega_L$ of the nucleus in the field associated with the electron states, the effective magnetic hyperfine field can be calculated from the thermal average over all electron states. However, when τ is comparable with $1/\omega_L$ relaxation phenomena are observed. A recent introduction to relaxation phenomena in Mössbauer spectroscopy was given by H. Wegener [We75].

In the case $\tau \gg 1/\omega_L$ the nuclear spin $\vec{I}$ couples with the electron spin $\vec{S}$. When Eq. 3.25 applies, the resulting levels are most conveniently described by F-states where $\vec{F} = \vec{I} + \vec{S}$. We shall return to this subject in chapter 7 where the Mössbauer spectrum of a paramagnetic Au^{II} compound is interpreted in terms of transitions between different F-states.

3.2 Relative intensities of the spectral lines

To first order, the probability amplitude for a transition from a state $|I_1,m_1>$ to a state $|I_2,m_2>$ with emission of a circularly polarized photon in the direction $\underline{k}$ is proportional to [Br62]

$$A^q_{m_1 m_2}(\underline{k}) = [\sum_{\ell m} \sqrt{2\ell+1} < I_2, m_2; \ell, m | I_1, m_1 >$$

$$\times D^\ell_{mq}(\alpha, \beta, \gamma) < I_1 \| a^m_\ell T^m_\ell \| I_2 >]$$

$$+ [\sum_{\ell m} \sqrt{2\ell+1} < I_2, m_2; \ell, m | I_1, m_1 >$$

$$\times q \, D^\ell_{mq}(\alpha, \beta, \gamma) < I_1 \| a^e_\ell T^e_\ell \| I_2 >] \quad , \quad (3.26)$$

where the first term describes the magnetic multipole radiation, the second term the electric multipole radiation. ℓ is the multipole order, $q = +1$ indicates right circular polarization and $q = -1$ left circular polarization. $< I_2, m_2; \ell, m | I_1, m_1 >$ is the Clebsch-Gordan coefficient coupling the vectors I_1, I_2 and ℓ. $< I_1 \| a^\pi_\ell T^\pi_\ell \| I_2 >$ with $\pi = m$ or $\pi = e$ is the reduced matrix element for magnetic or electric multipole radiation of order ℓ respectively. $D^\ell_{mq}(\alpha, \beta, \gamma)$ are the rotation matrices for rotation over the Euler angles α, β and γ:

$$D^\ell_{mq} = e^{-i\alpha m} \, d^\ell_{mq}(\beta) \, e^{-i\gamma q} \quad . \quad (3.27)$$

The reduced rotation matrices $d^\ell_{mq}(\beta)$ are real and listed for instance by Brink and Satchler [Br62].

From now on we restrict ourselves to the 77 keV $I_1 = \frac{1}{2} \rightarrow I_2 = \frac{3}{2}$ transition of ^{197}Au, which has a mixed multipolarity of magnetic dipole ($\ell = 1$) and electric quadrupole ($\ell = 2$) radiation. The mixing ratio δ is defined as [Fr65]:

$$\delta = \frac{< I_1 \| a^e_2 T^e_2 \| I_2 >}{< I_1 \| a^m_1 T^m_1 \| I_2 >} \quad . \quad (3.28)$$

The sign of δ gives the relative fase factor.

From Mössbauer measurements with a ^{197}Pt source in a magnetically polarized iron matrix the value as well as the sign of δ was determined: $\delta = -0.354 \pm 0.005$ [Pr75].

Generally the transition takes place between two states $|a>$ and $|b>$, which are not pure m_I-states, but linear combination of these:

$$|a> = \sum_1 c_{m_1}^{1/2} \left|\frac{1}{2}, m_1\right> \qquad (3.29a)$$

$$|b> = \sum_1 c_{m_1}^{3/2} \left|\frac{3}{2}, m_1\right> \quad . \qquad (3.29b)$$

For a transition between these two states the probability amplitude (Eq. 3.26) becomes proportional to:

$$A_{ab}^q (\underline{k}) \propto \sum_{m_1} \sum_{m_j} (C_{m_1}^{1/2})^* \; C_{m_j}^{3/2}$$

$$\times \left\{ \sqrt{3} < \frac{3}{2}, m_j; 1, m \left| \frac{1}{2}, m_1 \right> D_{mq}^1 (\alpha, \beta, \gamma) \right.$$

$$\left. - \delta \sqrt{5} < \frac{3}{2}, m_j; 2, m \left| \frac{1}{2}, n_1 \right> q D_{mq}^2 (\alpha, \beta, \gamma) \right\} \quad . \qquad (3.30)$$

The probability $P_{ab}^q (\underline{k})$ of the transition from $|a>$ to $|b>$ is proportional to $|A_{ab}^q (\underline{k})|^2$. Polarization insensitive measurements require an incoherent sum over q.

$$P_{ab}(\underline{k}) = |A_{ab}^{+1}(\underline{k})|^2 + |A_{ab}^{-1}(\underline{k})|^2 \quad . \qquad (3.31)$$

When we evaluate Eq. 3.31 with the help of Eq. 3.30 and Eq. 3.27, the Euler angle γ disappears and the angles α and β can be replaced by tne spherical angles θ and ϕ. The result is:

$$P_{ab}(\underline{k}) \propto \left\{ \sum_{m_1} \sum_{m_1'} \sum_{m_j} \sum_{m_j'} (C_{m_1}^{1/2})^* \; C_{m_1'}^{1/2} \; C_{m_j}^{3/2} \; (C_{m_j'}^{3/2})^* \right.$$

$$\times < \frac{3}{2}, m_j; \ell_1 = 1, m \left| \frac{1}{2}, m_1 \right> < \frac{3}{2}, m_j'; \ell_2 = 1, m' \left| \frac{1}{2}, m_1' \right>$$

$$\left. \times \Theta(\ell_1 = 1, m, \ell_2 = 1, m') \right\} \qquad (3.32a)$$

$$+ \delta^2 \{\text{same expression with } \ell_1 = \ell_2 = 2\} \tag{3.32b}$$

$$- \delta \{\text{same expression with } \ell_1 = 1 \text{ and } \ell_2 = 2\} \quad . \tag{3.32c}$$

The angular factors have been put together in the function Θ, which is given by:

$$\Theta(\ell_1 = \ell, m, \ell_2 = \ell, m') =$$

$$(2\ell+1) \, e^{-i(m'-m)\phi} \, [\, d^{\ell}_{m,+1}(\theta) \, d^{\ell}_{m',+1}(\theta) + d^{\ell}_{m,-1}(\theta) \, d^{\ell}_{m',-1}(\theta) \,] \tag{3.33a}$$

and

$$\Theta(\ell_1 = 1, m, \ell_2 = 2, m') =$$

$$2 \sqrt{15} \, \cos(m'-m)\phi \, [\, d^{1}_{m,+1}(\theta) \, d^{2}_{m',+1}(\theta) - d^{1}_{m,-1}(\theta) \, d^{2}_{m',-1}(\theta) \,] \quad . \tag{3.33b}$$

Eq. 3.32a and Eq. 3.32b describe the magnetic dipole and electric quadrupole radiation respectively, and Eq. 3.32c results from interference between both types of radiation. The same equations apply to absorption spectra.

We have evaluated the angular dependent terms $\Theta(\ell_1, m_1, \ell_2, m_2)$ and the results are given in Table 3.2, 3.3 and 3.4. In Table 3.5 we give the Clebsch-Gordan coefficients that are involved. In a number of cases the experimental circumstances provide conditions for a simpler form of Eq. 3.32, treated in the next paragraphs.

Table 3.2 $\Theta(\ell_1 = 1, m_1, \ell_2 = 1, m_2) = 3 \times e^{-i(m_2 - m_1)\phi}$

m_2 \ m_1	1	0	1
1	$\frac{1}{2}(1 + \cos^2\theta)$	$\frac{1}{2}\sqrt{2}\,\sin2\theta$	$\frac{1}{2}\sin^2\theta$
0	$\frac{1}{2}\sqrt{2}\,\sin2\theta$	$\sin^2\theta$	$\frac{1}{2}\sqrt{2}\,\sin2\theta$
-1	$\frac{1}{2}\sin^2\theta$	$\frac{1}{2}\sqrt{2}\,\sin2\theta$	$\frac{1}{2}(1 + \cos^2\theta)$

Table 3.3 $\Theta(\ell_1=2,m_1,\ell_2=2,m_2) = 5 \times e^{-i(m_2-m_1)\phi}$

m_1 \ m_2	2	1	0	-1	-2
2	$\frac{1}{2}(\sin^2\theta + \frac{1}{4}\sin^2 2\theta)$	$-\frac{1}{4}(\sin 2\theta + \frac{1}{2}\sin 4\theta)$	$-\frac{1}{4}\sqrt{\frac{3}{2}}\sin^2 2\theta$	$-\frac{1}{4}(\sin 2\theta - \frac{1}{2}\sin 4\theta)$	$-\frac{1}{2}(\sin^2\theta - \frac{1}{4}\sin^2 2\theta)$
1	$-\frac{1}{4}(\sin 2\theta + \frac{1}{2}\sin 4\theta)$	$\frac{1}{2}(\cos^2 2\theta + \cos^2 2\theta)$	$\frac{1}{4}\sqrt{\frac{3}{2}}\sin 4\theta$	$\frac{1}{2}(\cos^2 2\theta - \cos^2 2\theta)$	$\frac{1}{4}(\sin 2\theta - \frac{1}{2}\sin 4\theta)$
0	$-\frac{1}{4}\sqrt{\frac{3}{2}}\sin^2 2\theta$	$\frac{1}{4}\sqrt{\frac{3}{2}}\sin 4\theta$	$\frac{1}{4}\sin^2 2\theta$	$-\frac{1}{4}\sqrt{\frac{3}{2}}\sin 4\theta$	$-\frac{1}{4}\sqrt{\frac{3}{2}}\sin^2 2\theta$
-1	$-\frac{1}{4}(\sin 2\theta - \frac{1}{2}\sin 4\theta)$	$\frac{1}{2}(\cos^2\theta - \cos^2 2\theta)$	$-\frac{1}{4}\sqrt{\frac{3}{2}}\sin^2 4\theta$	$\frac{1}{2}(\cos^2\theta + \cos^2 2\theta)$	$\frac{1}{4}(\sin 2\theta - \frac{1}{2}\sin 4\theta)$
-2	$-\frac{1}{2}(\sin^2\theta - \frac{1}{4}\sin^2 2\theta)$	$\frac{1}{4}(\sin 2\theta - \frac{1}{2}\sin 4\theta)$	$-\frac{1}{4}\sqrt{\frac{3}{2}}\sin^2 2\theta$	$\frac{1}{4}(\sin 2\theta - \frac{1}{2}\sin 4\theta)$	$\frac{1}{2}(\sin^2\theta + \frac{1}{4}\sin^2 2\theta)$

Table 3.4 $\Theta(\ell_1=1,m_1,\ell_2=2,m_2) = \sqrt{15} \times 2\cos(\mu_2-\mu_1)\phi$

m_1 \ m_2	2	1	0	-1	-2
1	$-\frac{1}{2}\sin 2\theta$	$\frac{1}{2}(\cos^2\theta + \cos 2\theta)$	$\frac{1}{2}\sqrt{\frac{3}{2}}\sin 2\theta$	$\frac{1}{2}(\cos^2\theta - \cos 2\theta)$	0
0	$-\frac{1}{2}\sqrt{2}\sin^2\theta$	$\frac{1}{2}\sqrt{2}\sin 2\theta$	0	$\frac{1}{2}\sqrt{2}\sin 2\theta$	$\frac{1}{2}\sqrt{2}\sin^2\theta$
-1	0	$-\frac{1}{2}(\cos^2\theta - \cos 2\theta)$	$\frac{1}{2}\sqrt{\frac{3}{2}}\sin 2\theta$	$-\frac{1}{2}(\cos^2\theta + \cos 2\theta)$	$-\frac{1}{2}\sin 2\theta$

Table 3.5 Clebsch-Gordan coefficients [Co64]
$< 3/2,m_1;\ell,m \mid 1/2,m_2 >$

m_1	m_2	m	$\ell = 1$	$\ell = 2$
3/2	-1/2	-2	0	$+\sqrt{4/10}$
1/2	-1/2	-1	$+\sqrt{1/6}$	$-\sqrt{3/10}$
-1/2	-1/2	0	$-\sqrt{2/6}$	$+\sqrt{2/10}$
-3/2	-1/2	1	$+\sqrt{3/6}$	$-\sqrt{1/10}$
3/2	1/2	-1	$+\sqrt{3/6}$	$+\sqrt{1/10}$
1/2	1/2	0	$-\sqrt{2/6}$	$-\sqrt{2/10}$
-1/2	1/2	1	$+\sqrt{1/6}$	$+\sqrt{3/10}$
-3/2	1/2	2	0	$-\sqrt{4/10}$

a. Random orientation of the quantization axes with respect to the γ-ray direction

Such a random orientation is encountered in polycrystalline absorbers. In that case we have to integrate $P_{ab}(\underline{k})$ (Eq. 3.32) over the spherical angles θ and ϕ. Because the rotation matrices obey the orthogonality rule [Br62]

$$\int_0^{2\pi} \int_0^{2\pi} \int_0^{\pi} [D_{MM'}^I (\alpha,\beta,\gamma)]^{\star} D_{NN'}^J (\alpha,\beta,\gamma) \sin\beta \; d\beta \; d\alpha \; d\gamma$$

$$= \frac{8\pi^2}{2I+1} \; \delta(M,N) \; \delta(M',N') \; \delta(I,J) \qquad , \qquad (3.34)$$

the interference (Eq. 3.32c) between different multipole orders (I,J) disappears and the factors $\Theta(\ell_1,m_1,\ell_2,m_2)$ with $\ell_1=\ell_2=\ell$ integrate to $8\pi^2$. Thus we obtain for a powder absorber:

$$P_{ab} \propto \{ \sum_{m_i} \sum_{m_i'} \sum_{m_j} \sum_{m_j'} (C_{m_i}^{1/2})^{\star} \; C_{m_i'}^{1/2} \; C_{m_j}^{3/2} \; (C_{m_j'}^{3/2})^{\star} \qquad (3.35a)$$

$$\times < \frac{3}{2},m_j;\ell_1=1,m|\frac{1}{2},m_i > < \frac{3}{2},m_j';\ell_2=1,m'|\frac{1}{2},m_i' > \} \qquad (3.35a)$$

$$+ \; \delta^2 \; \{\text{same expression with } \ell_1=\ell_2=2\} \qquad . \qquad (3.35b)$$

When an electric field gradient and a magnetic field are present, it is always possible to obtain pure m_I-states for the $I = \frac{1}{2}$ level by choosing the quantization axis along the magnetic field. In that case the summations over m_i and m_i' in Eq. 3.35 contain only one term and we obtain for the transition from the $m_I = \pm \frac{1}{2}$ levels to one of the $I = \frac{3}{2}$ levels:

$$P(m_I = \pm \frac{1}{2} \to I = \frac{3}{2}) \propto \{\sum_{m_j} |C_{m_j}^{3/2}|^2 < \frac{3}{2},m_j;\ell=1,m|\frac{1}{2},\pm\frac{1}{2} >^2\}$$

$$+ \; \delta^2 \; \{\text{same expression with } \ell=2\}$$

$$= \frac{1}{2}\left| c_{\pm 3/2}^{3/2} \right|^2 + \frac{1}{3}\left| c_{\pm 1/2}^{3/2} \right|^2 + \frac{1}{6}\left| c_{\mp 1/2}^{3/2} \right|^2 \qquad (3.36a)$$

$$+ \delta^2 \left\{ \frac{1}{10}\left| c_{\pm 3/2}^{3/2} \right|^2 + \frac{1}{5}\left| c_{\pm 1/2}^{3/2} \right|^2 + \frac{3}{10}\left| c_{\mp 1/2}^{3/2} \right|^2 + \frac{2}{5}\left| c_{\mp 3/2}^{3/2} \right|^2 \right\} \qquad (3.36b)$$

The second equality is found by substituting the Clebsch-Gordan coefficients of Table 3.5.

When the nuclear levels are perturbed by a quadrupole interaction only, a quadrupole pair is observed, where both lines have the same intensity as follows by inserting the coefficients of Eq. 3.8 into Eq. 3.36.

b Oriented quantization axes

This situation occurs for instance, when the absorber is a single crystal. Eq. 3.36 has then to be used. The formula is simplified, when the quantization axis is parallel to the γ-ray direction ($\theta=0$). Then all off-diagonal terms in Tables 3.2 and 3.3 disappear and of Table 3.4 only the terms $(m_1,m_2) = (\pm 1,\pm 1)$ are retained.

When an external orientation is imposed on a polycrystalline sample by application of a magnetic field, we have to integrate over all directions of the applied field with respect to the crystal axes. In chapter 7 we shall encounter the special situation, where the direction of the γ-rays is parallel to a magnetic field. The magnetic hyperfine coupling is assumed to be isotropic. In that case $\theta=0$ and $I = \frac{1}{2}$ are pure m_I-states. The relative intensity of the transition between the $m_I = \pm \frac{1}{2}$ level and one of the $I = \frac{3}{2}$ levels is then given by·

$$P(m_I = \pm \frac{1}{2} \rightarrow I = \frac{3}{2}, \theta = 0) =$$

$$\left[3\left| c_{\pm 3/2}^{3/2}(\theta',\phi') \right|^2 + \left| c_{\mp 1/2}^{3/2}(\theta',\phi') \right|^2 \right]$$

$$+ \delta^2 \left[\left| c_{\pm 3/2}^{3/2}(\theta',\phi') \right|^2 + 3\left| c_{\mp 1/2}^{3/2}(\theta',\phi') \right|^2 \right]$$

$$+ \delta \left[2\sqrt{3}\left| c_{\pm 3/2}^{3/2}(\theta',\phi') \right|^2 - 2\sqrt{3}\left| c_{\mp 1/2}^{3/2}(\theta',\phi') \right|^2 \right] \qquad (3.37)$$

The coefficients $c_i^{3/2}(\theta',\phi')$ depend on the direction (θ',ϕ') of the magnetic field with respect to the crystal axes. For a polycrystalline absorber P (Eq. 3.37) is integrated over θ' and ϕ'.

3.3 Lattice vibrations

Two parameters of the Mössbauer spectrum are directly related to the vibrations of the absorbing and emitting nuclei in a solid. These include the probability of the Mössbauer effect (the Mössbauer fraction f), by which the relative absorption intensity of the spectrum is determined, and the second order Doppler shift, by which the spectral lines are shifted towards lower energy.

a. The Mössbauer fraction

We recall from chapter 1 that the probability of recoilless absorption or emission is given by:

$$f = |<L|e^{i\vec{q}\vec{r}}|L>|^2 \quad , \tag{3.38}$$

L describes the state of the lattice, $\vec{q}$ is the wavevector of the photon involved and $\vec{r}$ is the coordinate vector of the centre of mass of the decaying or absorbing nucleus.

The most simple description of L is a linear harmonic oscillator of mass m and frequency ω. The ground state wavefunction is given by:

$$\psi_o(x) = \sqrt[4]{m\omega/\pi\hbar} \, \exp(-\frac{m\omega x^2}{2\hbar}) \quad , \tag{3.39}$$

where $\hbar = h/2\pi$ is Planck's constant.
Replacing L (Eq. 3.38) by $\psi_o(x)$ yields after integration:

$$f = \exp(-\frac{\hbar q^2}{2m\omega}) \quad , \tag{3.40}$$

which can also be written as:

$$f = \exp(- <x^2>_o /\hbar^2) \qquad , \qquad\qquad\qquad (3.41)$$

where $<x^2>_o$ is the mean square vibrational amplitude associated with $\psi_o(x)$ and $\hbar = 1/q$. Eq. 3.41 clearly shows that to observe an appreciable Mössbauer effect the vibrational amplitude should be small with respect to the γ-ray wavelength.

For an actual solid at temperature T the procedure is more complicated, because of the occurrence of different modes of vibration, but it can be shown [Ka62] that Eq. 3.41 still holds as long as the amplitude of each mode is small compared with $\hbar$ and the nuclei are bound by harmonic forces:

$$f = e^{- <x^2>_T /\hbar^2} \qquad , \qquad\qquad\qquad (3.42)$$

where $<x^2>_T$ is the mean squared vibrational amplitude in the direction of emission at temperature T. This reduces the problem to the calculation of $<x^2>_T$, which can be written in terms of a continuous phonon frequency distribution $g(\omega)$. For a cubic lattice, where $<x^2> = \frac{1}{3} <\vec{r}^2>$, one obtains [We65]:

$$<x^2>_T = \frac{\hbar}{2m} \frac{1}{3N} \int_o^\infty \frac{g(\omega)}{\omega} \{ \frac{2}{\exp(\hbar\omega/kT)-1} + 1 \} d\omega \qquad , \qquad\qquad (3.43)$$

where m is the atomic mass, k the Boltzmann constant and N is the number of atoms in the lattice with

$$3N = \int_o^\infty g(\omega) d\omega \qquad . \qquad\qquad\qquad (3.44)$$

For complicated lattices $g(\omega)$ can have a complicated form. However, the Mössbauer effect measures only a weighted thermal average of the phonon spectrum, and for practical purposes $g(\omega)$ is approximated by one of the following models. In the Einstein model all atoms are assumed to vibrate with one characteristic frequency ω_E, thus:

$$g_E(\omega) = 3N \delta(\omega - \omega_E) \qquad , \qquad\qquad\qquad (3.45)$$

where δ is the Dirac-δ-function. The Einstein model gives for the Mössbauer fraction after insertion of Eq. 3.45 and Eq. 3.43 in Eq. 3.42:

$$f_E(T) = \exp \left\{ - \frac{\hbar^2}{2m\lambda^2} \frac{1}{k\Theta_E} \left(\frac{2}{\exp(\Theta_E/T)-1} + 1 \right) \right\} \quad , \qquad (3.46)$$

where $\Theta_E = \hbar\omega_E/k$ is the Einstein temperature.

In the Debye model $g(\omega)$ is quadratic in the frequency, with a cut-off at a maximum frequency ω_D:

$$g_D(\omega) = \frac{9N}{\omega_D^3} \omega^2 \quad (0 \leqslant \omega \leqslant \omega_D) \quad . \qquad (3.47)$$

Now we obtain for the Mössbauer fraction by the same procedure:

$$f_D(T) = \exp \left\{ - \frac{\hbar^2}{2m\lambda^2} \frac{3}{2k\Theta_D} \left(1 + 4 \frac{T^2}{\Theta_D^2} \int_0^{\Theta_D/T} \frac{x \, dx}{e^x - 1} \right) \right\} \quad , \qquad (3.48)$$

where $\Theta_D = \hbar\omega_D/k$ is the Debye temperature. Eq. 3.48 is frequently used to define an effective Debye temperature for the Mössbauer effect, since only one parameter (Θ_D) is involved. A detailed discussion of the applicability of the Debye theory to the Mössbauer effect is given by Nussbaum [Nu66].

b. Second order Doppler shift

The second order Doppler shift ΔE_s is a relativistic effect, that results from the non-vanishing mean square velocity $< v^2 >_T$ of the vibrating atoms in the lattice and is given by [We65]:

$$\frac{\Delta E_s}{E_o} = \frac{< v^2 >_T}{2c^2} \quad . \qquad (3.49)$$

Expressing $\Delta E_s/E_o$ in an equivalent Doppler velocity v_s, which should be imparted to make up for this shift, we obtain:

40

$$v_s = \frac{< v^2 >_T}{2c} \quad , \qquad\qquad (3.50)$$

$< v^2 >_T$ is directly related to the average internal energy of the vibrating lattice, which can be calculated with the Debye theory of lattice vibrations. One obtains [We65]:

$$v_s = \frac{1}{2mc} [\frac{9}{8} k\theta_D + 3T f(\frac{T}{\theta_D})] \quad , \qquad\qquad (3.51)$$

with

$$f(y) = 3y^3 \int_o^{1/y} \frac{x^3 \, dx}{e^x - 1} \quad , \qquad\qquad (3.52)$$

θ_D is the Debye temperature as obtained from specific heat measurements. For $T \ll \theta_D$ we may extend the upper limit of the integration to infinity with the result:

$$v_s (T \ll \theta_D) = \frac{1}{2mc} [\frac{9}{8} k\theta_D + \frac{3}{5} \pi^4 k \frac{T^4}{\theta_D^3}] \quad . \qquad\qquad (3.53)$$

The calculated second order Doppler shift for ^{197}Au, when the temperature is increased from 0°K to 50°K, with $\theta_D = 200^{\circ}$K, which is the order of magnitude for gold metal, is equal to 0.00321 mm/sec. For two samples at $T = 0^{\circ}$K with a Debye temperature difference of 100°K, which is the order of magnitude of the difference between gold metal and gold in molecular crystals, we obtain a shift of 0.00792 mm/sec, assuming that in both samples we deal with the atomic mass of gold. These shifts are in most cases negligible.

CHAPTER 4

ANALYSIS OF MOSSBAUER ABSORPTION SPECTRA

The measured spectra were analysed in terms of a number of lines, corresponding with transitions between discrete energy levels. In the next sections we shall treat the transmission lineshape function and the consequences of a thin-absorber-approximation. The fitting procedures, carried out on a IBM 370/155 computer, are treated in the subsequent section. In the last section of this chapter attention is given to the determination of the Mössbauer fraction.

4.1 Transmission lineshape function

a. Formulation

The number of γ-quanta $N(v_s)$ that reach the detector as function of the velocity v_s of the source with respect to the absorber can be written as:

$$N(v_s) = N_x + [1 - f_s] N_\gamma(\infty) + f_s N_\gamma(\infty) T(v_s) \quad , \tag{4.1}$$

$N_\gamma(\infty)$ is the number of quanta corresponding with the 77 keV Mössbauer transition measured far from resonance, N_x represents all other radiation and f_s is the fraction of 77 keV quanta, emitted by the source without recoil. $T(v_s)$ is the fraction of the recoillessly emitted quanta, that is transmitted by the absorber. Because in our experiments no distinction is made between the first and second term of Eq. 4.1, it can be re-written in a more convenient form:

$$N(v_s) = B [1 - F_s \{ 1 - T(v_s) \}] \quad , \tag{4.2}$$

where B and F_s are given by:

$$B = N_x + N_\gamma(\infty) \tag{4.3}$$

$$F_s = \frac{f_s N_\gamma(\infty)}{N_x + N_\gamma(\infty)} \quad . \tag{4.4}$$

The energy distribution of the Mössbauer radiation is assumed to have a Lorentzian shape with natural linewidth Γ_o:

$$S(v,v_s) = \frac{2}{\pi\Gamma_o} \frac{[\Gamma_o/2]^2}{[v-v_s]^2 + [\Gamma_o/2]^2} \qquad . \qquad (4.5)$$

The energy variable has been expressed in the equivalent Doppler velocity v with Eq. 1.1. v_s is the velocity of the source with respect to the absorber and Γ_o the full width at half height. The same assumption is made for the energy distribution of each of the n_a transitions in the absorber:

$$A(v) = \sum_{i=1}^{n_a} w_i \frac{[\Gamma_o/2]^2}{[v-v_i]^2 + [\Gamma_o/2]^2} \qquad , \qquad (4.6)$$

where w_i and v_i are the probability and the energy of the transition, respectively, with $\sum_{i=1}^{n_a} w_i = 1$. The energy distribution of the transmitted intensity is then given by

$$T(v,v_s) = S(v,v_s) \exp[-t_a A(v)] \qquad . \qquad (4.7)$$

The absorption coefficient t_a, commonly called the effective absorber thickness, is given by:

$$t_a = f_a t_o \sigma_o \frac{1}{1+\alpha} \qquad , \qquad (4.8)$$

where f_a is the recoilless fraction of the absorber and α is the internal conversion coefficient. The areal density of gold is given by t_o and σ_o is the maximum resonance cross section:

$$\sigma_o = \frac{\lambda^2}{2\pi m} \frac{2I_e + 1}{2I_g + 1} \qquad , \qquad (4.9)$$

where λ is the wavelength of the γ radiation, I_e and I_g are the nuclear spins of excited and ground state respectively and m is the mass of the gold atom.

As all γ quanta are counted, which fall in the energy range of the γ-detector, we have to integrate the transmitted intensity over this energy range, which is very large compared to the energy width of the emitted radiation. Therefore the measured intensity is given by:

$$T(v_s) = \int_{-\infty}^{\infty} T(v,v_s)\,dv \quad .$$

(4.10)

Combining the equations 4.2, 4.5, 4.6, 4.7 and 4.10 we obtain:

$$N(v_s) = B \left[1 - F_s \left[1 - \sum_{-\infty}^{\infty} \frac{2}{\pi\Gamma_o} \frac{[\Gamma_o/2]^2}{[v-v_s]^2 + [\Gamma_o/2]^2} \right. \right.$$

$$\left. \left. \times \exp\left\{-t_a \int \sum_{i=2}^{n_a} w_i \frac{[\Gamma_o/2]^2}{[v-v_i]^2 + [\Gamma_o/2]^2}\right\} dv \right] \right] \quad .$$

(4.11)

This equation is a special case of the general formulation given by Margulies and Ehrman [Ma61]. It applies, when the linewidth of both source and absorber are the same and equal to the natural linewidth and resonant absorption in the source is neglected. Furthermore we have neglected a dispersion term, due to interference of magnetic dipole and electric quadrupole radiation, which has been observed by Erickson et al. [Er73] in thick ($t_a > 5$) absorbers of gold metal.

b. Evaluation

The calculation of Eq. 4.11 is straightforward except for the so called transmission integral of Eq. 4.10:

$$T(v_s) = \int_{-\infty}^{\infty} S(v,v_s)\, X(v)\,dv \quad ,$$

(4.12)

with

$$X(v) = \exp\left[-t_a A(v)\right] \quad .$$

(4.12a)

44

For the evaluation of the transmission integral the integration range is subvided in two wing-contributions and a middle part:

$$T(v_s) = W_L(v_s) + N(v_s) + W_R(v_s) \quad , \tag{4.13}$$

with

$$W_L(v_s) = \int_{-\infty}^{v_L} S(v,v_s) \, X(v) \, dv \quad , \tag{4.13a}$$

$$M(v_s) = \int_{v_L}^{v_R} S(v,v_s) \, X(v) \, dv \quad , \tag{4.13b}$$

and

$$W_R(v_s) = \int_{v_R}^{\infty} S(v,v_s) \, X(v) \, dv \quad . \tag{4.13c}$$

The left and right boundaries v_L and v_R, respectively, are chosen in such a way, that $X(v) \sim 1$ for $v < v_L$ and $v > v_R$. Then the wing-contributions can be evaluated analytically with $X(v) = 1$ and we obtain:

$$W_L(v_s) = \frac{1}{\pi} \, \text{arctg} \, \frac{2 \, [\, v_s - v_L \,]}{\Gamma_o} + \frac{1}{2} \quad , \tag{4.14}$$

and a similar expression for $W_R(v_s)$.
$M(v_s)$ is calculated with a numerical technique, described by Cranshaw [Cr74], which is fast and very accurate [Sh74]. In this method, the integral Eq. 4.13b is replaced by the sum

$$M(v_j) = \Delta v \sum_{i=1}^{n} S(v_i, v_j) \, X(v_i)$$

$$= \Delta v \sum_{i=1}^{n} S(v_{i-j}) \, X(v_i) \quad , \tag{4.15}$$

where $v_{i-j} = v_i - v_j$ and $\Lambda v = v_{i+1} - v_i$. Eq. 4.15 is commonly called a convolution

sum of the two sequencies S and X [Op75]. It was pointed out by Cranshaw that in comparing $M(v_j)$ with an experimental spectrum Δv should be taken equal to the velocity increment corresponding with one channel of the multi-channel analyzer. The advantage of Eq. 4.15 over previously used methods [Sh74] is that $M(v)$ is obtained for all points of the spectrum, while $S(v)$ and $X(v)$ have to be calculated only once. The non-linear velocity channel number relation (see section 2.5) is corrected for by a linear interpolation. The computer programme used is based on the programme given by Lin and Preston [Li74].

4.2 Thin absorber approximation and saturation effects

When the effective absorber thickness is small ($t_a \ll 1$) the exponential in Eq. 4.7 can be expanded to first order in a Taylor series:

$$\exp \{-t_a A(v)\} \simeq [1-t_a A(v)] \quad . \tag{4.16}$$

Then we obtain for the transmission integral:

$$T(v_s) = \int_{-\infty}^{\infty} S(v,v_s) [1 - t_a A(v)] dv \quad . \tag{4.17}$$

This expression can be evaluated analytically [We65] and one gets after insertion of the result in Eq. 4.2:

$$N(v_s) = B \{1 - F_s \sum_1^{n_a} \frac{t_a}{2} \frac{[\Gamma/2]^2}{[v_1-v_s]^2 + [\Gamma/2]^2}\} \quad , \tag{4.18}$$

with $\Gamma = 2\Gamma_o$. Margulies and Ehrman [Ma61] have shown that a Lorentzian shape is a good approximation to the measured spectrum when $t_a < 4$. However, the intensity is no longer linearly related to the thickness and the linewidth should be replaced by an effective width $\Gamma > 2\Gamma_o$. The deviation of the Lorentzian shape as function of t_a (the so called saturation effect) has been discussed by several authors [By63,La63,Ma61,Sh61,Wi75], mostly from a theoretical point of view. We have used a more empirical approach and have calculated single line absorption spectra with Eq. 4.11 for values of t_a up to

12 over a velocity range equal to five times the linewidth $2\Gamma_o$. These spectra were subsequently fitted with a Lorentzian. In Figure 4.1 we have plotted the intensity, linewidth and area of these Lorentzians, normalized by $F_s t_a/2$, $2\Gamma_o$
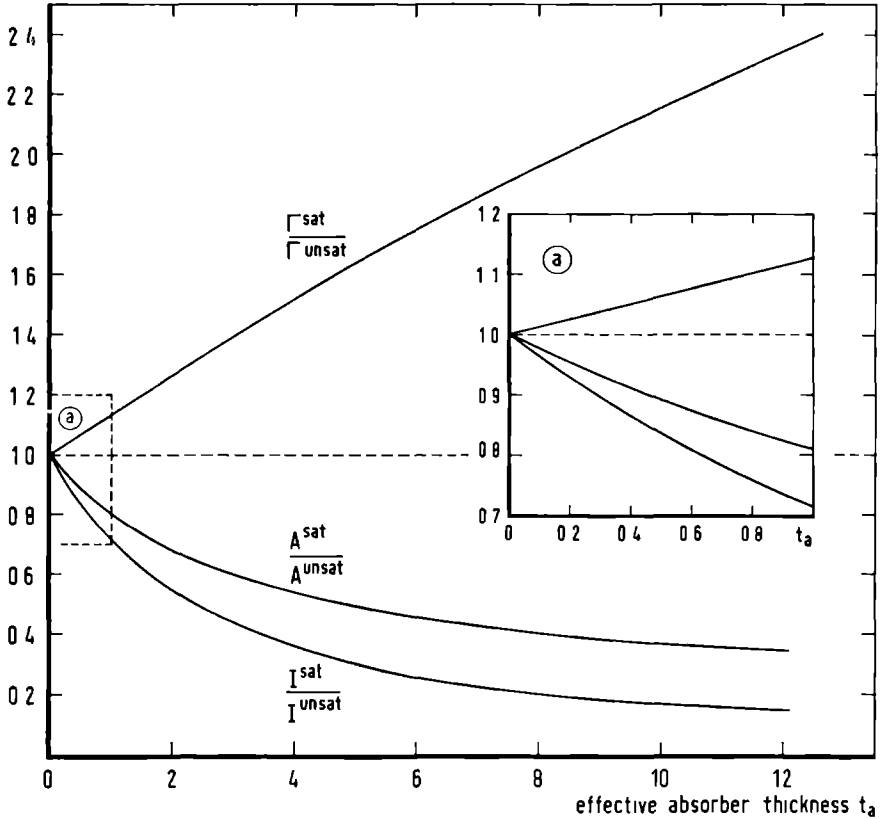

Figure 4.1   The effect of saturation on the linewidth Γ, the intensity I and the area A as function of the effective absorber thickness t_a. The saturated parameters are the values of least-square-fitted Lorentzians. The unsaturated parameters are given by $\Gamma^{unsat} = 2\Gamma_o$, $I^{unsat} = F_s t_a/2$ and $A^{unsat} = \frac{\pi}{2} \Gamma_s t_a \Gamma_o$. Numerical data are given in Table 4.1.

and $\frac{\pi}{2} F_s t_a \Gamma_o$, respectively, these being the intensity, linewidth and area of the Lorentzian in Eq. 4.8. For $t_a = 0.2$ the normalized peak intensity is 0.939 and the normalized area is 0.953 indicating the importance of saturation even for thin absorbers: in case of gold metal $t_a = 0.2$ corresponds with a thickness

Table 4.1   *Relation between the effective absorber thickness t_a and the normalized linewidth Γ, intensity I and area A. The saturated values are the parameters of least-square-fitted Lorentzians. The unsaturated parameters are given by $\Gamma^{unsat} = 2\Gamma_o$, $I^{unsat} = F_s t_a/2$ and $I^{unsat} = \frac{1}{2}\pi F_s t_a \Gamma_o$ (see Eq. 4.18).*

t_a	$\Gamma^{sa}/_{unsat}$	$I^{sat}/_{I^{unsat}}$	$A^{sat}/_{A^{m~at}}$		t_a	$\Gamma^{sat}/_{unsat}$	$I^{sat}/_{I^{unsat}}$	$A^{sa}/_{A^{unsat}}$
0.01	1.0011	0.9963	0.9974		1.1	1.143	0.6894	0.7880
0.03	1.0037	0.9889	0.9926		1.2	1.156	0.6690	0.7734
0.06	1.0075	0.9779	0.9853		1.3	1.170	0.6496	0.7598
0.10	1.012	0.9635	0.9756		1.4	1.183	0.6311	0.7463
0.13	1.016	0.9530	0.9665		1.5	1.196	0.6135	0.7338
0.16	1.020	0.9426	0.9615		1.8	1.236	0.5654	0.6989
0.20	1.026	0.9290	0.9527		2.0	1.263	0.5368	0.6778
0.23	1.029	0.9201	0.9460		2.5	1.329	0.4755	0.6322
0.26	1.033	0.9092	0.9393		3.0	1.394	0.4257	0.5936
0.30	1.018	0.8964	0.9304		3.5	1.458	0.3849	0.5612
0.33	1.042	0.8870	0.9240		4.0	1.521	0.3508	0.5334
0.36	1.046	0.8777	0.9176		5.0	1.643	0.2977	0.4884
0.40	1.051	0.8655	0.9096		6.0	1.754	0.2585	0.4533
0.45	1.057	0.8507	0.8995		7.0	1.861	0.2284	0.4250
0.50	1.064	0.8362	0.8897		8.0	1.963	0.2047	0.4018
0.55	1.070	0.8222	0.8801		9.0	2.060	0.1856	0.3823
0.60	1.077	0.8084	0.8707		10.0	2.153	0.1697	0.3654
0.70	1.090	0.7021	0.8524		12.0	2.348	0.1455	0.3417
0.80	1.103	0.7567	0.8351					
0.90	1.117	0.7334	0.8188					
1.00	1.130	0.7109	0.8029					

of 9.4 mgr/cm^2 at 4.2°K. A practical application of Figure 4.1 will be discussed in section 4.4.

4.3   Least squares fitting procedures

At several instances of this research the best estimate of a number of parameters is obtained in a numerical fitting procedure. We used the method of least squares, where the sum of squared differences (SSD) between the measured and calculated points is minimized as function of the parameters.

a   Linear hypothesis

The measured points f_i ($i = 1,..n$) are assumed to be a linear function of the parameters x_i ($i = 1,..m$). In matrix notation we have:

$$\underline{F} = \underline{A}\underline{X} + \underline{E} \quad , \tag{4.19}$$

where e_1 is the random error associated with f_1 and $\underline{A}$ is called the design matrix. For the calculated points we have:

$$\hat{\underline{F}} = \underline{A}\underline{X} \quad . \tag{4.20}$$

If we define a vector of residuals $\underline{V}$:

$$\underline{V} = \underline{F} - \hat{\underline{F}} \quad , \tag{4.21}$$

the best estimate of the parameters: $\hat{\underline{X}}$ is obtained when the quadratic form:

$$S = \underline{V}.\underline{V} \quad , \tag{4.22}$$

is minimal. All observations f_1 are here assumed to be independent and to have equal weight. It can be shown [Ha64], that $\hat{\underline{X}}$ is given by:

$$\hat{\underline{X}} = [\underline{A}'\underline{A}]^{-1} \underline{A}'\underline{F} \quad , \tag{4.23}$$

and that the variance-covariance matrix for the parameters is given by:

$$\underline{M} = [\underline{A}'\underline{A}] \frac{\underline{V}.\underline{V}}{n-m} \quad , \tag{4.24}$$

where $\underline{A}'$ is the transposed of $\underline{A}$.

An example of the applicability of Eq. 4.23 is the fitting of a polynomial to the measured velocity (see section 2.5). In this case we used a computer programme, based on a code given by McCracken and Dorn [Mc64].

In case of a non-linear problem one may use a Taylor expansion of f_1 to first order around f_1^o, where f_1^o corresponds with a first estimate x_1^o of the parameters x_1:

$$f_1 - f_1^o \simeq \sum_{j=1}^{m} \frac{\partial f_1}{\partial x_j} (x_j^1 - x_j^0) \quad . \tag{4.25}$$

49

Thus we have now:

$$\underline{F} = \{f_i - f_i^O\} \quad , \quad (4.26a)$$

$$\underline{A} = \{\frac{\partial f_i}{\partial x_j}\} \quad , \quad (4.26b)$$

$$\underline{X} = \{x_i^1 - x_i^0\} = \{\Delta x_i\} \quad . \quad (4.26c)$$

After calculation of $\hat{\underline{X}}$ (Eq. 4.23) we obtain a better estimate x_i:

$$x_i^1 = x_i^0 + \Delta x_i \quad .$$

This procedure is repeated until the changes in the parameters are smaller than some convergence criterium.

This procedure was used to fit a sum of Lorentzians to the Mössbauer spectrum:

$$f_i = \sum_{j=1}^{n_d} d_j v_i^{j-1} - \sum_{j=1}^{n_a} \frac{t_j}{\{\frac{b_j - v_i}{c_j} \cdot 2\}^2 + 1} \quad . \quad (4.27)$$

The n_d polynomial constants of the baseline: d_j, and the intensities t_j, the positions b_j and the widths c_j of the n_a Lorentzians are the parameters to be optimized. The parameters can also be fixed at an arbitrary value. Furthermore it is possible to relate the parameters linearly by means of a set of matrices D, T, B and C, required by the programme as input:

$$d_j = \sum_{i=1}^{n_\delta} D_{ji} \delta_i \quad , \quad (4.28a)$$

$$t_j = \sum_{i=1}^{n_\tau} T_{ji} \tau_i \quad , \quad (4.28b)$$

$$b_j = \sum_{i=1}^{n_\beta} B_{ji} \beta_i \quad , \quad (4.28c)$$

$$c_j = \sum_{i=1}^{n_\gamma} C_{ji} \gamma_i \quad . \tag{4.28d}$$

In that case δ_i, τ_i, β_i and γ_i are optimized. The standard deviations, as calculated with Eq. 4.24 are quoted with the results.

b Non linear methods

In those cases where it was not possible to obtain a closed form expression for f_i (e.g. the transmission integral of Eq. 4.11 or the Debye integral of Eq. 3.43) we have used three methods to minimize the SSD value: A Monte Carlo minimum search [Ja68], a gradient minimalization [Ro60], and a parabole fit of the SSD function [Da68]. The derivatives, necessary in the last method, were calculated numerically. The three methods are part of a computer programme (MINUIT) obtained from CERN [Ja69]. The standard deviations in the parameters, calculated by MINUIT, proved not always to be reliable, in particular when the parameters were strongly correlated. The errors, quoted with the results, were then estimated by a comparison with duplicate measurements.

4 4   Determination of the Mossbauer fraction f_a

The value of f_a is obtained from the effective absorber thickness t_a (Eq. 4.8).

For thick absorbers ($t_a > 2$) it was possible to determine t_a from a fit of Eq. 4.11 to the experimental spectrum with B, F_s and t_a and v_j as parameters. The linewidth Γ_o was held fixed at the value of 0.923 mm/sec [Er71]. In first instance the positions were kept at the values found by means of a fit with Lorentzian lines. After convergence of B, F_s and t_a, the positions v_j were also allowed to vary together with B, F_s and t_a.

For thin absorbers F_s and t_a are strongly correlated. In fact, as can be seen from Eq. 4.18, F_s and t_a cannot be determined independently by a single fit, when the thin absorber approximation really applies. In those cases one can make use of the results given in Figure 4.1, which are presented in a modified and more useful way in Figure 4.2 for $t_a < 2$. In this figure intensity and area are normalized by $F_s/2$ and $\frac{\pi}{2} F_s \Gamma_o$ respectively. The
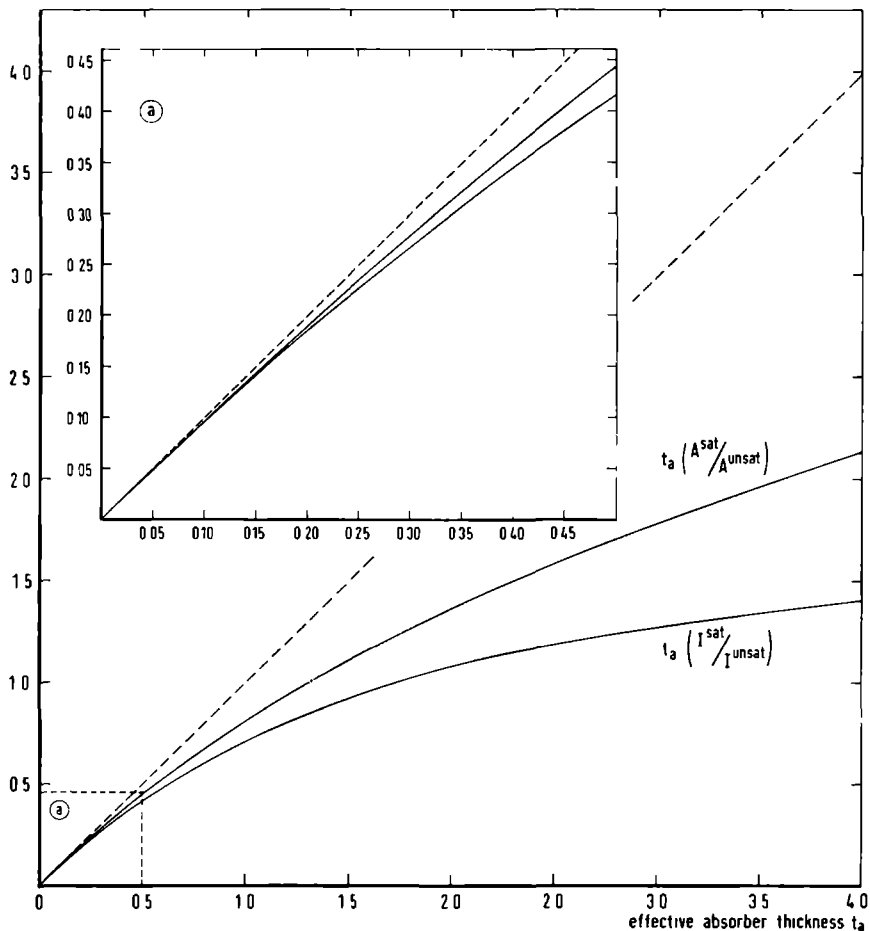
51

Figure 4.2   Saturation curve used for the determination of t_a from the measured (saturated) absorption. For a definition of the parameters see Figure 4.1.

vertical scale is now proportional to the measured values and can be cali-
brated using a sample of known thickness (t_a). In practice the area should be
used, as this quantity is less sensitive to source parameters and experi-
mental broadening. In applying this procedure we assumed, that the fraction
of 77 keV Mössbauer radiation, contributing to the detector current, is
independent of the absorber, which means, that the differences in non-
resonant absorption are neglected. This is justified because the largest
contribution to the detector current comes from the 77 keV Mössbauer

52

transition and from Pt and Au X-rays in the same energy range.

Because of the different half-lives of the various isotopes in the
source, F_s is a function of time (see section 2.2) and the measured areas must
be corrected for this time dependence before comparing with each other. This
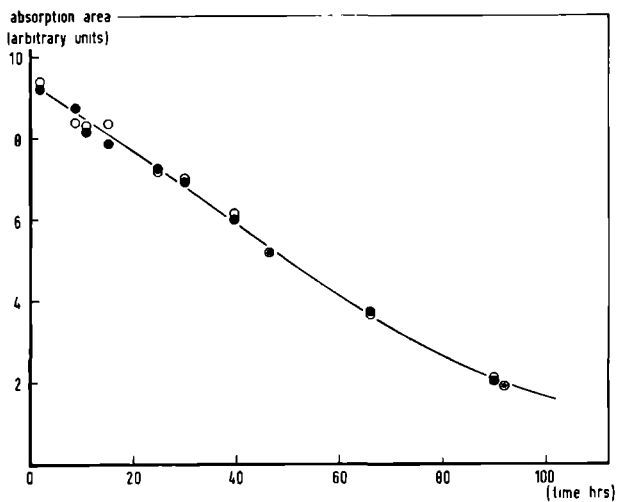was done with measured decay curves as shown in Figure 4.3.

Figure 4.3   Time dependence of the absorption area of a least-
square-fitted Lorentzian relative to the background
level, using the 45 mg, 46% ^{196}Pt source and an arbitrary
sample. This area is proportional to the contribution of
the 77.345 keV Mössbauer radiation to the total radiation
to which ^{199}Au mainly contributes. Open and closed circles
correspond with the two spectra obtained in one measurement.
The drawn line is a least squares fit of the function: $A(t) =$
$a/ [b + exp(ct)]$, where a and b are free parameters and
depend on the nature of the absorber, the specific activities
of the different isotopes and the efficiency of the detector.
The constant c has been fixed at $c = -ln2$ $\{1/t_{\frac{1}{2}}(^{199}Au) - 1/t_{\frac{1}{2}}$
$(^{197}Pt)\} = 0.0293$ (t in hrs). Such decay-curves were determined
for each series of measurements with one source, in order to
correct the observed absorption areas for the decay of the
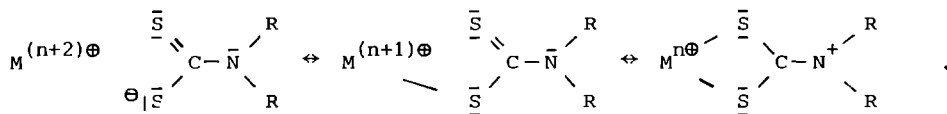source, when the Mössbauer fraction had to be obtained.

CHAPTER 5

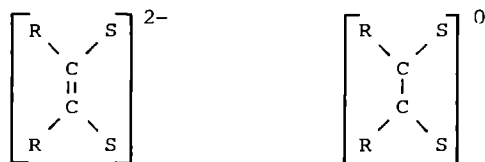# DIAMAGNETIC GOLD(I) AND GOLD(III) COMPOUNDS

5 1 Introduction

The chemistry of gold is mainly one of coordination compounds, in which gold occurs in the oxidation states I and III [Co72]. Other oxidation states are very uncommon. Only one paramagnetic gold(II) compound has been isolated in pure form (see chapter 7) and an oxidation state V has recently been established [Le72,Ka73].

The first Mössbauer investigations of gold compounds were reported by Roberts et al. [Ro62] and by Shirley [Sh64]. Since these early investigations Quadrupole Splittings (QS) and Isomer Shifts (IS) have been observed to vary over a wide range. A correlation between the IS- and QS values of both Au^I and Au^{III} compounds has been established by Faltens and Shirley [Fa70] and by Charlton and Nichols [Ch70]. These authors described the bonding of gold in terms of sp (Au^I) and dsp^2 (Au^{III}) hybridization. The electric field gradient is attributed to the number of 5d and 6p electrons in the hybrid-orbitals, which varies with the degree of covalency. Faltens [Fa70] has tried to obtain a quantitative estimate of the covalency. However, the $< r^{-3} >$ value for 6p electrons, which was assumed to be independent of the charge of the gold atom, came out much too large to be credible. Bartunik, Potzel, Mössbauer and Kaindle [Ba70] found a correlation between the IS and the spectrochemical series for a number of Au^I and Au^{III} compounds. An explanation was given on the basis of an LCAO-MO model.

We have extended the series of Au^I and Au^{III} compounds studied by Mössbauer spectroscopy. Our particular interest has been focused on complexes of gold with sulphur-donor-ligands, which have been the subject of extensive chemical [B165,Li73], structural [No71a] and EPR [Re74] investigations in our institute. The compounds were made available to us by Dr. Van der Linden [Li76]. As emphasized by Willemse, Cras, Steggerda and Keijzers [Wi76], dithiocarbamates can stabilize "unusually" high oxidation states. These authors attribute this property to resonance structures in which the actual charge on the metal is lower than the formal oxidation state:

$$M^{(n+2)\oplus} \quad \overset{\overset{\displaystyle \bar{\underline{S}}}{\diagdown}}{\underset{\overset{\displaystyle \ominus|\bar{\underline{S}}}{\diagup}}{C} - \bar{N}} \overset{\diagup R}{\diagdown R} \quad \leftrightarrow \quad M^{(n+1)\oplus} \quad \overset{\overset{\displaystyle \bar{\underline{S}}}{\diagdown}}{\underset{\overset{\displaystyle \bar{\underline{S}}}{\diagup}}{C} - \bar{N}} \overset{\diagup R}{\diagdown R} \quad \leftrightarrow \quad M^{n\oplus} \quad \overset{\overset{\displaystyle \bar{\underline{S}}}{\diagup}}{\underset{\overset{\displaystyle \bar{\underline{S}}}{\diagdown}}{C} - N^{+}} \overset{\diagup R}{\diagdown R} \quad .$$

In complexes with dithiolene ligands the assignment depends on whether the ligand is considered as dinegative or neutral:

$$\begin{bmatrix} R \diagdown & \diagup S \\ & C & \\ & \| & \\ & C & \\ R \diagup & \diagdown S \end{bmatrix}^{2-} \qquad \begin{bmatrix} R \diagdown & \diagup S \\ & C & \\ & | & \\ & C & \\ R \diagup & \diagdown S \end{bmatrix}^{0} \qquad .$$

Reviews concerning the chemistry and structure of complexes with these ligands are given by Coucouvanis [Co70] and Eisenberg [Ei70]. We have also investigated two novel tetrathiotungstato $(WS_L)^{2-}$ complexes of gold, synthesized by Dornfeld [Do76]. Thio-anions of tungsten as ligands in coordination compounds are rather new and have been reviewed by Dieman and Müller [Di73]. Finally we have measured the Mössbauer parameters of some organogold compounds, made available to us by Van Koten [Ko76a]. In these compounds aryl groups are directly bound to gold. The degree of covalency is expected to be larger than in previously studied gold compounds. The results of our measurements are summarized in the next section.

At the present time it is not possible to give a quantitative explanation of the observed hyperfine interactions in complexes with heavy elements, because of the lack of adequate self-consistent field calculations. An attempt by Van Rens [Re74] to calculate the EPR parameters of silver and gold compounds with an LCAO-MO method using the Extended Hückel theory led to a poor agreement with the experimental parameters. A qualitative interpretation, however, may elucidate some aspects of the chemical bonding. Such interpretation is simplified by the fact that the coordination symmetry of gold is strongly correlated with the oxidation state. Generally Au^{III} has a planar 4-coordination like most d^8 compounds, whereas Au^{I} (d^{10}) complexes have a linear 2-coordination. Therefore we shall give a simple MO model, assuming D_{4h} and $D_{\infty h}$ coordination symmetry for Au^{III} and Au^{I} compounds respectively. Within the framework of this model the results will be discussed.

Table 5.1 Abbreviations used in the chemical formulas

Me = methyl, Et = ethyl, Pr = n-propyl, Bu = n-butyl, Hep = heptyl,
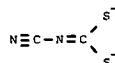Oct = octyl, Ph = phenyl, Bu_4N^+ = tetra-butylammonium

R_2dtc =
N,N-di-alkyl(aryl)dithiocarbamate
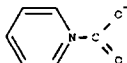
Rxan =
O-alkylxanthate

cdc =
N-cyanodithiocarbimate
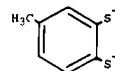
pip =
piperidyl

OC(O)pip =
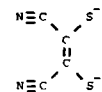N-piperidyl-carbamate

ac =
acetate

dtp =
di-alkyldithiophosphate
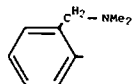
tdt =
toluene-3,4-dithiolate

mnt =
maleonitriledithiolate

nds =
naphthalene-1,8-dithiolate

dmamp =
2-[(dimethylamino)methyl]phenyl

dmap =
2-dimethylaminophenyl

otf = O_3SCF_3

The Mössbauer parameters of the individual compounds are considered in some detail in the last section of this chapter.

5.2   Compilation of results

For the sake of clarity the studied compounds have been put together in seven groups (a-g) of related composition and structure. Together with our results we list values obtained by other investigators. The abbreviations, used in the chemical formulas, are listed in Table 5.1.

a. AuX_4^- with X = Br,Cl

Table 5.2   Mössbauer parameters of AuX_4^- with $X = Br,Cl$.

Compound		Isomer Shift [1] (mm/sec)	Quadrupole Splitting (mm/sec)	Number in Figure 5.15	Ref. for preparation and basic properties
(N-Et.pip)AuCl$_4$	[2]	1.02 ± 0.02	1.4 ± 0.1	1	De90
Bu$_4$N AuCl$_4$	[3]	1.02 ± 0.06	1.31 ± 0.14		
Ph$_4$As AuCl$_4$	[4]	1.03 ± 0.04	1.88 ± 0.07		
NH$_4$ AuCl$_4$	[3]	0.87 ± 0.03	1.18 ± 0.06		
NH$_4$ AuCl$_4$.xH$_2$O	[4]	0.86 ± 0.05	1.7 ± 0.1		
KAuCl$_4$	[5]	0.44 ± 0.06	1.27 ± 0.08		
KAuCl$_4$	[3]	0.81 ± 0.03	1.11 ± 0.06		
KAuCl$_4$.2H$_2$O	[4]	0.87 ± 0.08	1.4 ± 0.1		
NaAuCl$_4$.2H$_2$O	[3]	0.81 ± 0.05	1.21 ± 0.10		
NaAuCl$_4$.xH$_2$O	[4]	0.81 ± 0.05	1.4 ± 0.2		
HAuCl$_4$.4H$_2$O	[3]	0.66 ± 0.04	0.94 ± 0.08		
HAuCl$_4$.xH$_2$O	[4]	0.60 ± 0.08	unresolved		
Bu$_4$N AuBr$_4$	[2]	0.92 ± 0.02	1.5 ± 0.1	2	De90
Ph$_4$As AuBr$_4$	[4]	0.85 ± 0.11	1.5 ± 0.2		
KAuBr$_4$.2H$_2$O	[2]	0.67 ± 0.02	1.3 ± 0.1	3	De90
KAuBr$_4$.2H$_2$O	[5]	0.67 ± 0.02	1.13 ± 0.02		
KAuBr$_4$.2H$_2$O	[4]	0.56 ± 0.02	unresolved		
KAuBr$_4$	[3]	0.60 ± 0.02	1.13 ± 0.06		

[1] With respect to the source of ^{197}Au in Pt

[2] This work

[3] [Ba70]

[4] [Ch70]

[5] [Fa70]

The Mössbauer parameters of compounds, containing the anionic species $AuCl_4^-$ and $AuBr_4^-$ are summarized in Table 5.2. Because most of these compounds are readily available and well characterized, a large number was already measured. The crystallographic structures of $NaAuCl_4 \cdot 2H_2O$ [Bo65], $HAuCl_4 \cdot 4H_2O$ [W169] and $RbAuCl_4$ [St70] revealed a square planar coordination of gold with an average Au-Cl bond length of 2.28 Å. $AuBr_4^-$ in $KAuBr_4 \cdot 2H_2O$ is also square planar with a bond length of 2.55 Å [Co36]. The first coordination sphere of gold in the other compounds is assumed to be similar.

Because of the small quadrupole splitting (Figure 5.1) the spectra were fitted with two Lorentzians constrained to have an equal intensity and an
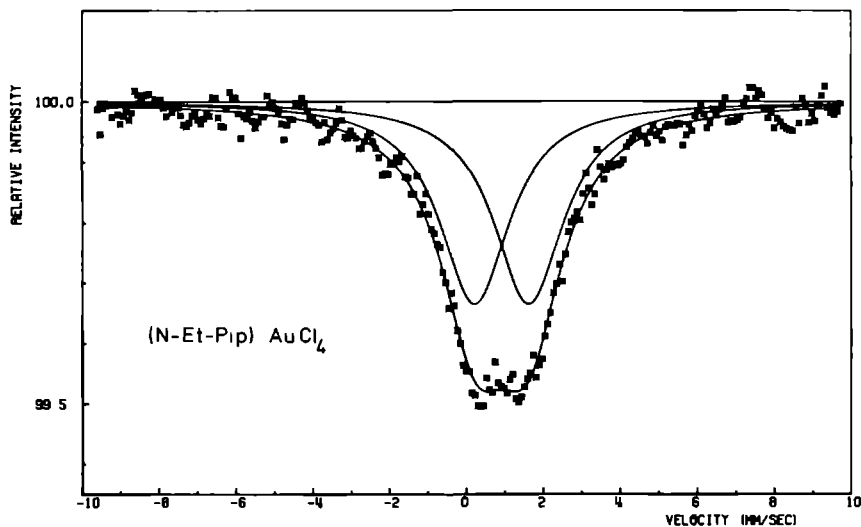

Figure 5.1   Mössbauer spectrum of (N-Et-pip) AuCl$_4^-$. The drawn line is a least squares fit of two Lorentzians, constrained to have equal intensity and width.

equal width. Strong correlation exists between the splitting and the width of the two lines. This introduces an additional uncertainty in the QS, which is accounted for in the error, quoted with our results.

b Bis-dithiolato Au^{III} complexes

Table 5.3 presents the Mössbauer parameters of Au^{III} compounds with

bidentate sulphur-donor-ligands. The spectra were fitted witn two Lorentzians, constrained to have equal intensity and width. A large number of compounds

Table 5.3 *Mössbauer parameters of bis-dithiolato* Au^{III} *complexes.*

Compound	Isomer Shift [1] (mm/sec)	Quadrupole Splitting (mm/sec)	Number in Figure 5.15	Ref. for preparation and basic properties
Bu_4N $Au(tdt)_2$	2.99 + 0.02	2.73 ± 0.02	4	Da67
$Au(mnt)(dtc)$	2.64 ± 0.02	2.57 ± 0.02	5	Li71b
Bu_4N $Au(mnt)_2$	2.92 ± 0.01	2.33 ± 0.01	6	Da63
$Au(H_2dtc)_2Br$	2.26 ± 0.02	3.01 ± 0.04	7	Li71a
$Au(Me_2dtc)_2Br$	2.04 ± 0.04	2.60 + 0.05	8	Li71a
$Au(Et_2dtc)_2Br$	2.24 ± 0.03	3.06 ± 0.05	9	Li71a
$Au(Pr_2dtc)_2Br$	2.22 + 0.02	3.02 ± 0.04	10	Li71a
$Au(Bu_2dtc)_2Br$	2.20 ± 0.08	2.8 ± 0.2	11	Be70a
$Au(Ph_2dtc)_2Br$	2.06 + 0.03	2.89 ± 0.05	12	Li71a
Bu_4N $Au(cdc)$	2.15 ± 0.05	2.71 ± 0.07	13	Li71a

[1] With respect to the source of ^{197}Au in Pt

containing the $Au(R_2dtc)_2$-ion has been isolated with different anions [Be68a Be70a,Be70b,Cr70,Li71a]. The geometry of the cation in one of these compounds is shown in Figure 5.2. The molecular structure of $Bu_4N^+Au(mnt)_2^-$ is not known,

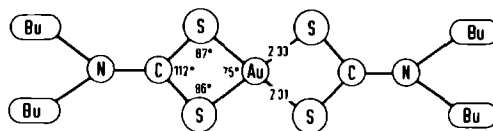Figure 5.2 *Geometry of the cation in $Au(Bu_2dtc)_2Br$ [Be70a].*
A few relevant bond distances are given in Å.

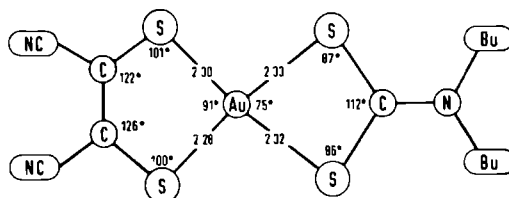but assumed to be the same as the Cu-analogon [Da63,Fo64]. Figure 5.3 shows the molecular structure of the mixed complex Au(dtc)(mnt).

Figure 5.3   Geometry of Au(dtc)(mnt) [No73]. A few relevant
bond distances are given in Å. The gold atom is
situated 0.035 Å below the plane through the four
sulphur atoms. The angle between the plane of the
mnt molecule and the plane of the dtc molecule is
8.5^{o}.

c. Di-halo and dimethyl-gold(III) dithiocarbamates

Table 5.4   Mössbauer parameters of di-halo and dimethyl-gold(III)
dithiocarbamates.

Compound	Isomer Shift [1] (mm/sec)	Quadrupole Splitting (mm/sec)	Number in Figure 5.15	Ref. for preparation and basic properties
$(CH_3)_2Au(Me_2dtc)$	3.97 ± 0.01	5.07 ± 0.02	14	B164
$(CH_3)_2Au(Pr_2dtc)$	3.95 ± 0.01	4.98 ± 0.01	15	B164
$(CH_3)_2Au(Bu_2dtc)$	3.99 ± 0.01	5.11 ± 0.02	16	B164
$I_2 Au(Bu_2dtc)$	1.26 ± 0.03	2.10 ± 0.05	17	B164
$Br_2 Au(Bu_2dtc)$	1.47 ± 0.01	2.20 ± 0.01	18	B164
$BrI Au(Bu_2dtc)$	1.28 ± 0.01	1.77 ± 0.02	19	B164
$Cl_2 Au(Hep_2dtc)$	1.35 ± 0.01	1.95 ± 0.02	20	B164

[1] With respect to the source of ^{197}Au in Pt

The structure of the compounds, listed in Table 5.4 has to be formulated as
[B165]:
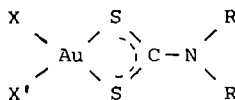
where X,X' = Br, Cl, I or Me and R = alkyl. The molecular structure of
Au(dtc)Br$_2$ [Be68b] revealed a planar four-fold coordination of gold. Typical

*Figure 5.4   Mössbauer spectra of $Cl_2Au(Hep_2dtc)$ and $(CH_3)_2Au(bu_2dtc)$.
The two Lorentzians were constrained to have equal intensity
and width.*

d. Gold(I) complexes with bidentate sulphur-donor-ligands

The Au^I compounds with bidentate sulphur-donor-ligands, of which the
structure has been reported, are dimeric (Figures 5.5 and 5.6). The Au–Au
distances of 2.8 Å and 3.0 Å are extraordinary short compared with the Au–Au
distance in gold metal of 2.88 Å [Su58] or with the covalent radius of 1.33 Å
for Au^I [Co67]. The coordination at the site of the gold atom is approximately
linear. The Mössbauer parameters are listed in Table 5.5 and the spectrum of
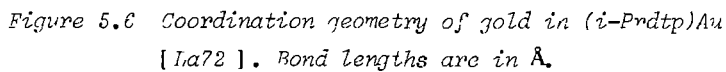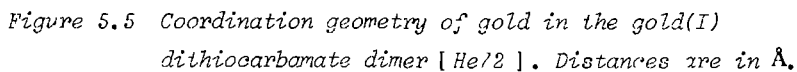
Figure 5.5 Coordination geometry of gold in the gold(I)
dithiocarbamate dimer [He72]. Distances are in Å.

Figure 5.6 Coordination geometry of gold in (i-Prdtp)Au
[La72]. Bond lengths are in Å.

Au(Pr₂dtc) is shown in Figure 5.7.

Compound	Isomer Shift [1] (mm/sec)	Quadrupole Splitting (mm/sec)	Number in Figure 5.15	Ref. for preparation and basic properties
Au(Et$_2$dtc)	1.70 + 0.01	5.98 + 0.02	21	Ak59
Au(Pr$_2$dtc)	1.80 ± 0.01	6.39 ± 0.02	22	Ak59
Au(Bu$_2$dtc)	1.62 + 0.01	5.94 + 0.01	23	Ak59
Au(Oct.xan)	1.42 + 0.01	6.16 ± 0.02	24	Li71a
Au(atb)	0.96 + 0.01	6.09 ± 0.02	25	La72
Ph$_4$P Au WS$_4$	0.86 ± 0.01	5.58 + 0.02	26	Vi76
Ph$_4$As Au WS$_4$	1.10 + 0.01	5.71 _ 0.02	27	Vi76
Ph$_4$P Au CS$_3$	1.91 + 0.01	6.43 + 0.01	28	Vi76

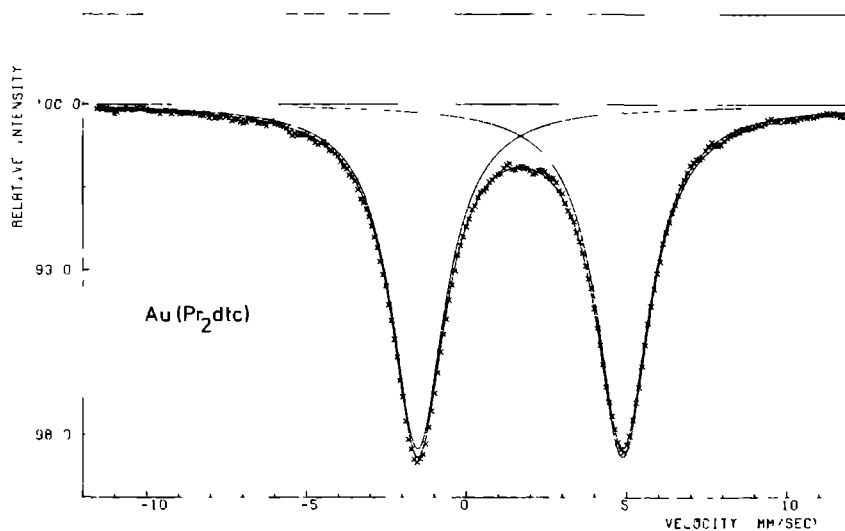[1] With respect to the source of ^{197}Au in Pt

Figure 5.7 Mössbauer spectrum of Au(Pr$_2$dtc).

e. Triphenylphosphine gold(I) complexes

In the compounds listed in Table 5.6 the gold atom is two-coordinated. The molecular structures of Ph$_3$PAuCN [Be69] and Ph$_3$PAuCl [So73] reveal P-Au-C and P-Au-Cl angles of 169° and 179° respectively. Some typical Mössbauer spectra are shown in Figure 5.8 .

Table 5.6   Mössbauer parameters of Triphenylphosphine gold(I) complexes.

Compound		Isomer Shift [1] (mm/sec)	Quadrupole Splitting (mm/sec)	Number in Figure 5.15	Ref. for preparation and basic properties
Ph$_3$P AuI	[2]	1.24 ± 0.06	8.3 ± 0.1		
Ph$_3$P AuBr		2.77 + 0.01	7.35 ± 0.01	29	Co62
Ph$_3$P AuBr	[2]	2.76 ± 0.06	7.40 ± 0.10		
Ph$_3$P AuCl		2.93 ± 0.01	7.50 ± 0.01	30	Co62
Ph$_3$P AuCl	[2]	2.96 + 0.07	7.47 ± 0.13		
Ph$_3$P AuSCN		2.85 + 0.01	7.65 ± 0.01	31	Co62
Ph$_3$P AuSC(S)pip		2.79 ± 0.02	7.60 ± 0.03	32	P174
Ph$_3$P Au(Ph$_2$dtc)		2.95 ± 0.02	7.79 ± 0.04	33	W172
Ph$_3$P AuSeC(O)pip		3.16 + 0.02	7.93 ± 0.02	34	P174
Ph$_3$P Au SC(O)pip		3.24 ± 0.02	8.35 ± 0.03	35	P174
Ph$_3$P Au(ac)	[2]	3.3 ± 0.2	7.6 ± 0.2		
Ph$_3$P AuN$_3$	[2]	3.3 + 0.2	8.4 ± 0.2		
Ph$_3$P Au(nds)		3.74 ± 0.02	8.42 ± 0.02	36	L171a
Ph$_3$P AuCN		3.82 + 0.01	10.11 + 0.01	37	N169
Ph$_3$P AuCN	[2]	3.9 ± 0.2	10.5 ± 0.2		
Ph$_3$P Au(Me)	[2]	4.93 ' 0.04	10.35 + 0.06		

[1] With respect to the source of ^{197}Au in Pt

[2] [Ch70]

The monothio-, monoseleno- and dithiocarbamate ligands are expected to be monodentate in the present compounds as is the case in Ph$_3$PAuSC(S)N(C$_2$H$_5$)$_2$ (see Figure 5.9).
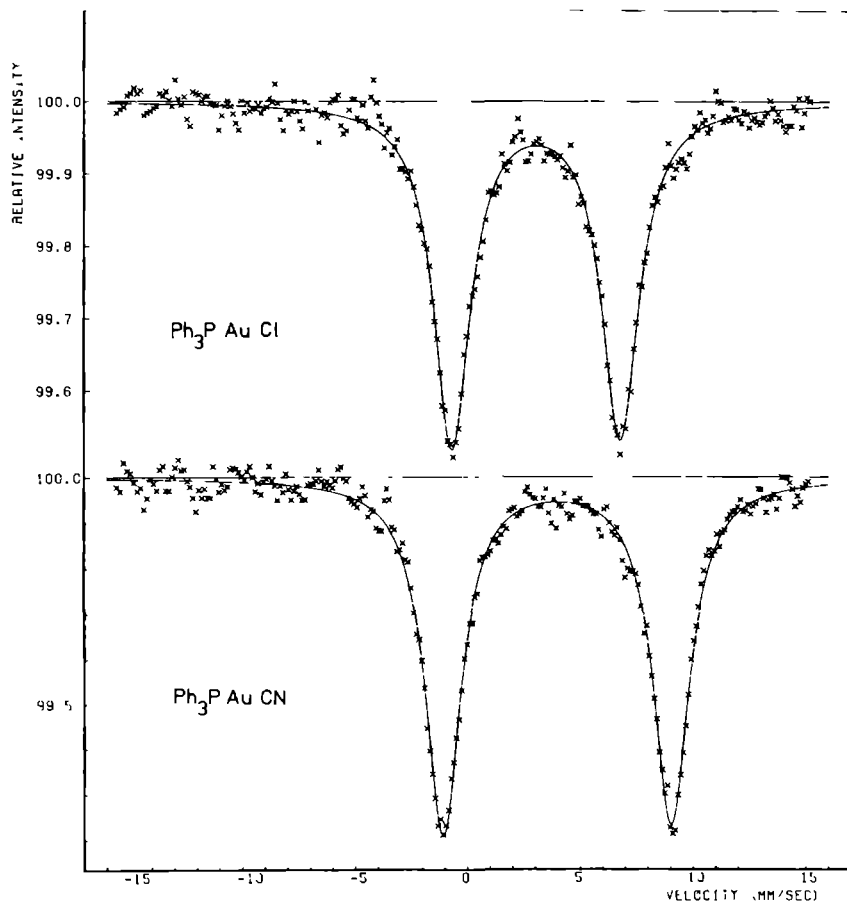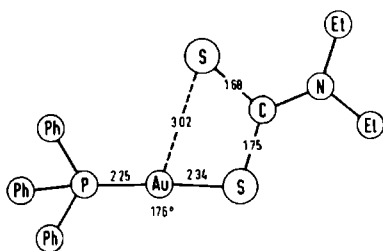
Figure 5.8   Mössbauer spectra of Ph₃PAuCl and Ph₃PAuCN.

Figure 5.9   The coordination of gold in Ph₃PAu(Et₂dtc) [Wi72].
*Distances are given in Å.*

The results of our Mössbauer measurements on some polynuclear organo-gold compounds are given in Table 5.7.

Table 5.7   Mössbauer parameters of polynuclear organo-gold compounds.

Compound	Isomer Shift [1] (mm/sec)	Quadrupole Splitting (mm/sec)	Number in Figure 5.15	Ref. for preparation and basic properties
$(dmap)_4Au_2Cu_4I_2$	4.00 ± 0.01	9.37 ± 0.01	38	Ko76
$(dmap)_4Au_2Cu_4(otf)_2$	3.88 ± 0.01	9.14 ± 0.01	39	Ko76
$(dmap)_4Au_2Cu_2$	4.42 ± 0.01	9.86 ± 0.01	40	Ko74a, Ko72
$(dmamp)_4Au_2L_{12}$	5.27 ± 0.01	11.29 ± 0.01	41	Ko74a, Ko72
$(dmap)_4Au_2L_{12}$	5.65 + 0.01	12.01 + 0.01	42	Ko76, Ko72
$(dmap)Au$	3.69 ± 0.01	6.73 ± 0.01	43	Ko76
$(dmamp)Au$	4.44 ± 0.01	7.32 ± 0.01	44	Ko76, Ko74b

[1]   With respect to the source of ^{197}Au in Pt.

For (dmap)Au and (dmamp)Au the following structure has been proposed [Ko76] :
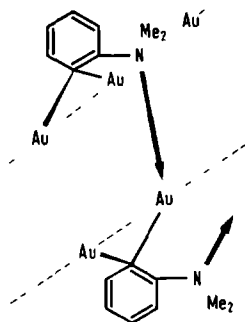
This polymeric structure is based on the Cu-analogue of (dmap)Au and the low solubility of the compounds.

Substitution of copper in $(dmap)_4Cu_6I_2$ by gold invariably results in the species $(dmap)_4Au_2Cu_4I_2$ [Ko76] . In the hexanuclear copper cluster of $(dmap)_4Cu_6I_2$ (see Figure 5.10) the four equatorial copper atoms have an approximately trigonal coordination and the two apical atoms a linear one
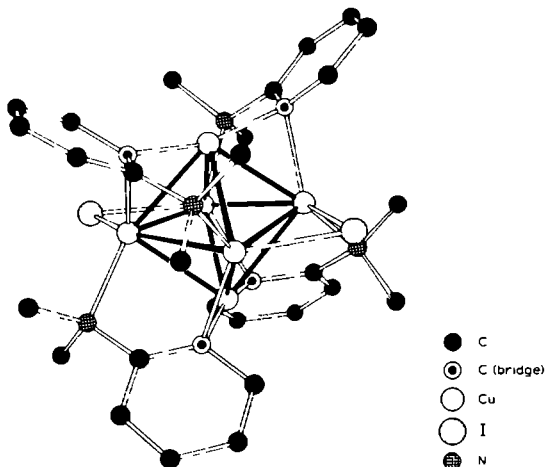
Figure 5.10   Structure of the hexanuclear copper cluster [Gu72].

(not taking into account copper-copper bonding). It is highly probable that
the two gold atoms occupy the two apical positions, because of the tendency
of Au^I to have a linear coordination. We have also measured the Mössbauer
spectrum of a similar compound containing otf⁻ instead of I⁻.

Figures 5.11 and 5.12 show the largest quadrupole splittings ever
observed for gold. For the compounds in question the following structure
has been proposed [Ko76] :
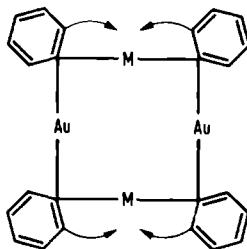
The proposal is based on the analogous compound in which Au is replaced by
Cu and where M = Li.

Figure 5.11   Mössbauer spectrum of $(dmap)_4Au_2Li_2$. The compound decomposes
by exposure to air. The decomposition product has been
identified by its QS and IS to be $(dmap)Au$.

Figure 5.12   Mössbauer spectrum of $(dmamp)_4Au_2Li_2$. The asymmetry is probably
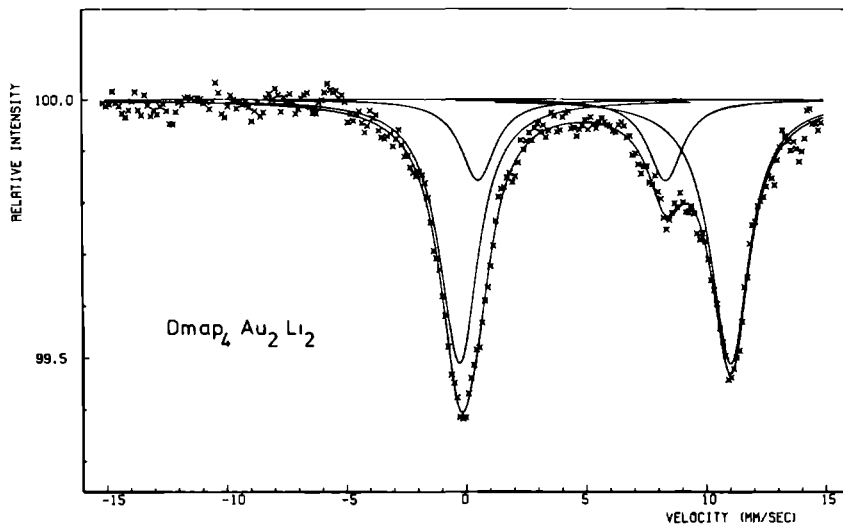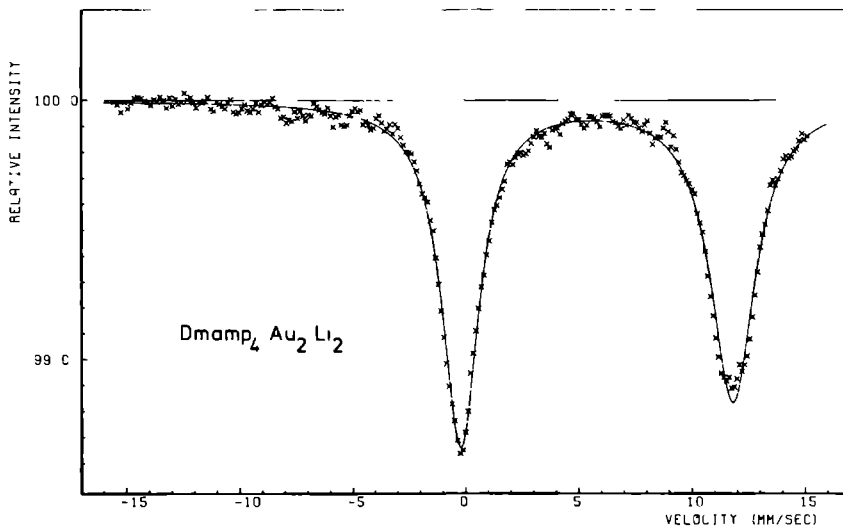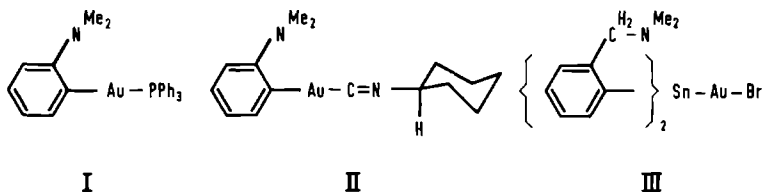caused by slight decomposition. The area of both absorption
lines is the same.

g. Some additional compounds

The coordination of Au^I in the compounds: $(dmap)AuP(Ph)$ (I), $(dmap)AuCN$ C_6H_{11} (II) and $(dmamp)SnAuBr$ (III) is presumably linear:

In the compounds I and II there exist a possibility of three-fold coordination through the amino group. However, for gold(I) 3-coordination is rarely found. The only example is $(Ph_3P)_2AuCl$, the molecular structure of which has recently been solved (Figure 5.13). The Mössbauer parameters are summarized in Table 5.8 and the spectrum of $(Ph_3P)_2AuCl$ is shown in Figure 5.14.

Table 5.8 Mössbauer parameters of some additional gold compounds.

Compound	Isomer Shift [1] (mm/sec)	Quadrupole Splitting (mm/sec)	Number in Figure 5.15	Ref. for preparation and basic properties
$AuCl(PPh_3)_2$	1.15 ± 0.01	8.03 ± 0.01	45	Ba74
$(dmap)AuPPh_3$	4.84 + 0.01	10.11 ± 0.01	46	Ko76
$(dmap)AuCN(C_6H_{11})$	4.62 + 0.01	10.35 ± 0.01	47	Ko76
$(dmap)SnAuBr$	2.34 ± 0.02	6.51 ± 0.03	48	Ko76
AuCN	2.35 ± 0.01	7.97 ± 0.01	49	Jo57
AuCN [2]	2.30 ± 0.05	8.0 ± 0.1		
AuCN [3] [5]	1.6 ± 0.2	8.09 ± 0.03		
AuCN [4]	2.37 ± 0.02	8.39 ± 0.02		

[1] With respect to the source of ^{197}Au in Pt

[2] [Ba70]

[3] [Fa70]

[4] [Ch70]

[5] The IS is probably erroneous.
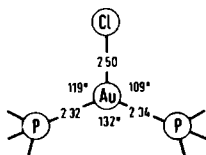
Figure 5.13   Coordination geometry of gold in (Ph₃P)₂AuCl [Ba/4].
Distances are in Å.
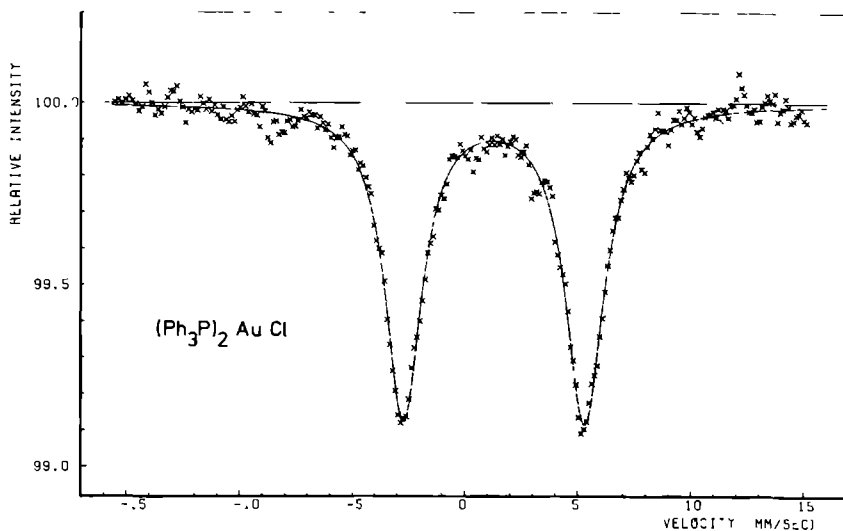
Figure 5.14   Mössbauer spectrum of (Ph₃P)₂AuCl.

5.3 General remarks on the results

In Figure 5.15 the QS is plotted against the IS. The Mössbauer parameters
of compounds, previously reported in the literature, are also shown. It is
clear that even with the addition of a large number of new compounds the
linear relationship between QS and IS still exists. This relation is on the
average given by

$$QS [Au^{I}] = 1.06 \ IS + 5.05 \quad (mm/sec) \tag{5.1}$$

$$QS [Au^{III}] = 1.74 \ IS - 0.22 \quad (mm/sec) \tag{5.2}$$
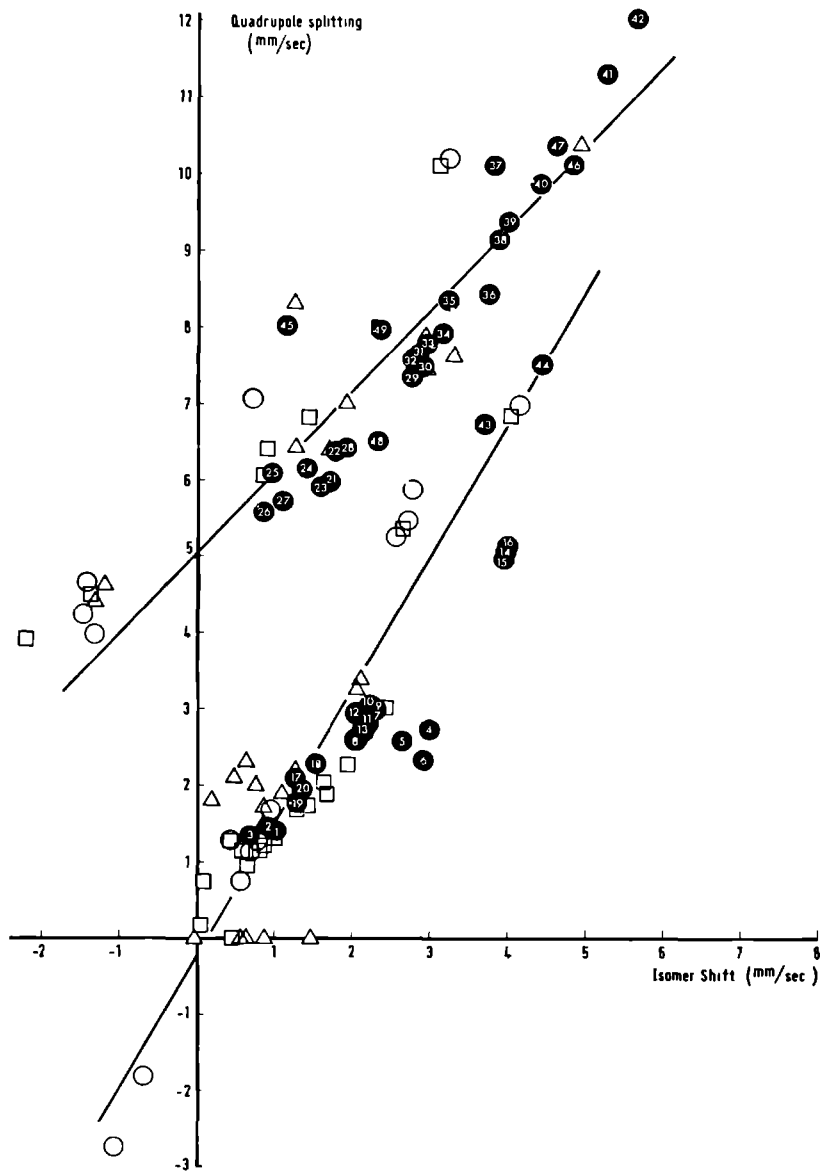
Figure 5.15 QS-IS correlation for Au^I and Au^{III} compounds. The numbers refer
to our measurements on the compounds listed in Tables 5.2-5.8
○ [Fa70], □ [Ba70], △ [Ch70]. The sign of QS is discussed
in section 5.4.

Comparing a Au^{I} with a Au^{III} complex with the same ligands, the IS of the latter is larger and its QS is smaller. The Mössbauer parameters are largest, when the coordinating atoms belong to the Group-IV-elements, and smallest for the Group-VII-elements. Furthermore an average-environment-rule seems to apply, in the sense that the Mössbauer parameters of compounds with mixed ligands are averages of those of the pure complexes.

Although the lines approach each other for large IS and QS values, it still appears possible to determine the oxidation state of gold from the QS and IS values taken together.

5.4 Interpretation

In an attempt to quantify IS and QS in terms of covalency parameters we consider in first instance σ-bonding only. For Au^{I} complexes we assume

Table 5.9 Irreducible represen-
tations (IR) and
orbitals for ML_2
$(D_{\infty h})$ complexes.

| IR	metal	ligand σ	ligand π
Γ_g^+	s, d_{z^2}	σ_s	
$_g^-$	d_{xz}, d_{yz}		π_{xz}, π_{yz}
Δ_g	$d_{xy}, d_{x^2-y^2}$		
Σ_u^+	p_z	σ_z	
Π_u	p_x, p_y		π_x, π_y

$$\sigma_s = \sqrt{\tfrac{1}{2}}\,(\sigma_1 + \sigma_2)$$
$$\sigma_p = \sqrt{\tfrac{1}{2}}\,(\sigma_1 - \sigma_2)$$
$$\pi_{xz} = \sqrt{\tfrac{1}{2}}\,(\pi_1 - \pi_2)$$
$$\pi_{yz} = \sqrt{\tfrac{1}{2}}\,(\pi_1' - \pi_2')$$
$$\pi_x = \sqrt{\tfrac{1}{2}}\,(\pi_1 + \pi_2)$$
$$\pi_y = \sqrt{\tfrac{1}{2}}\,(\pi_1' + \pi_2')$$

Table 5.10 Irreducible representations (IR)
and orbitals for ML_4 (D_{4h}) .

IR	metal	ligand σ	ligand π
A_{1g}	s, d_{z^2}	σ_s	
A_{2g}			π_a'
B_{1g}	$d_{x^2-y^2}$		$\pi_{x^2-y^2}'$
B_{2g}	d_{xy}	σ_{xy}	
E_g	d_{xz}, d_{yz}		π_{xz}, π_{yz}
A_{2u}	p_z		π_z
B_{1u}			π_b
E_u	p_x, p_y	σ_x, σ_y	π_x', π_y'

$$\sigma_s = \tfrac{1}{2}\,(\sigma_1 + \sigma_2 + \sigma_3 + \sigma_4)$$
$$\sigma_{xy} = \tfrac{1}{2}\,(\sigma_1 - \sigma_2 + \sigma_3 - \sigma_4)$$
$$\sigma_x = \sqrt{\tfrac{1}{2}}\,(\sigma_1 - \sigma_3)$$
$$\sigma_y = \sqrt{\tfrac{1}{2}}\,(\sigma_2 - \sigma_4)$$
$$\pi_{xz} = \sqrt{\tfrac{1}{2}}\,(\pi_1 - \pi_3)$$
$$\pi_{yz} = \sqrt{\tfrac{1}{2}}\,(\pi_2 - \pi_4)$$
$$\pi_z = \tfrac{1}{2}\,(\pi_1 + \pi_2 + \pi_3 + \pi_4)$$
$$\pi_b = \tfrac{1}{2}\,(\pi_1 - \pi_2 + \pi_3 - \pi_4)$$
$$\pi_a' = \tfrac{1}{2}\,(\pi_1' + \pi_2' + \pi_3' + \pi_4')$$
$$\pi_{x^2-y^2}' = \tfrac{1}{2}\,(\pi_1' - \pi_2' + \pi_3' - \pi_4')$$
$$\pi_x' = \sqrt{\tfrac{1}{2}}\,(\pi_1' - \pi_3')$$
$$\pi_y' = \sqrt{\tfrac{1}{2}}\,(\pi_2' - \pi_4')$$
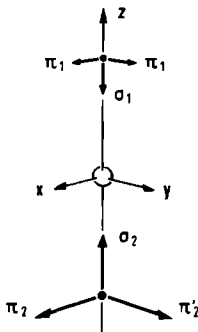
Figure 5.16   Arrangement of the ligand orbitals in linear ML_2 complexes.
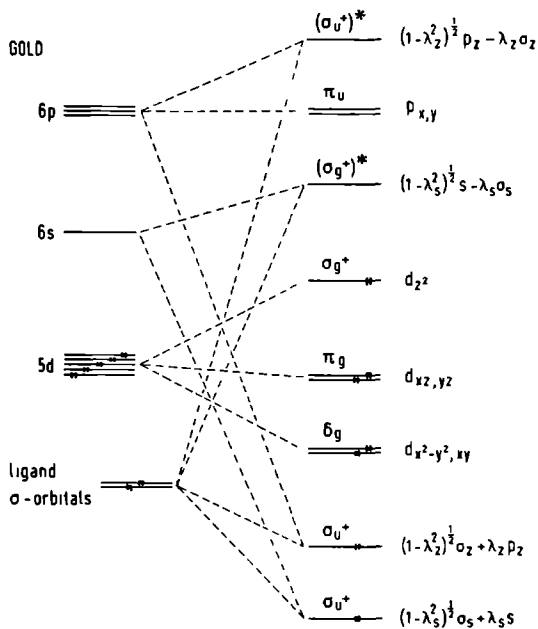
Figure 5.17   Molecular orbital energy level diagram for linear $(D_{\infty h})$ gold(I) complexes. Only σ-bonding is taken into account.

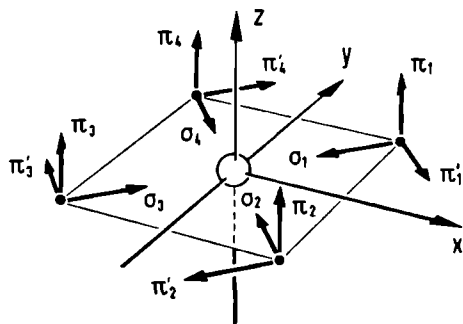*Figure 5.18 Arrangement of the ligand orbitals in square planar ML_4 complexes*
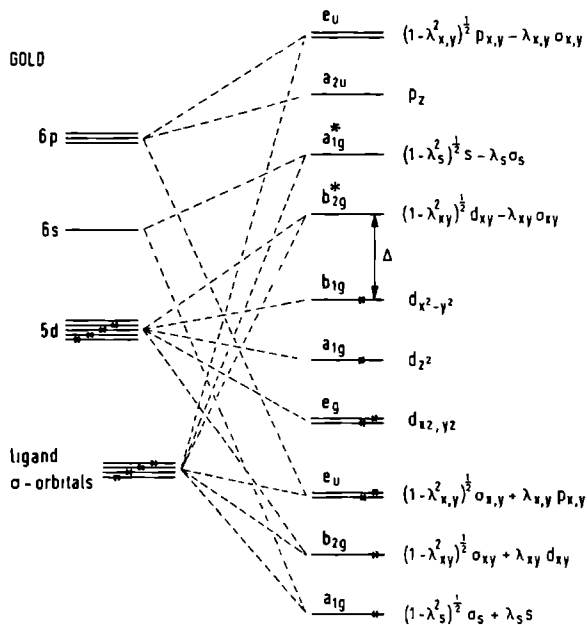

Figure 5.19 Molecular orbital energy level diagram for square planar (D_{4h}) gold(III) complexes. The arrangement is based on the results of MO calculations on $PtCl_4^{2-}$ [Ba67]. Only σ-bonding is taken into account. Indicated is the ligand field splitting parameter Δ.

$D_{\infty h}$ coordination symmetry and D_{4h} symmetry for Au^{III} complexes. Table 5.9 and 5.10 contain the irreducible representations and associated orbitals for linear ML_2 and square planar ML_4 complexes of the metal M and the ligands L. The ligand orbitals are defined as shown in Figures 5.16 and 5.18. The general form of the resulting MO-diagram is shown in Figure 5.17 for Au^I and in Figure 5.19 for Au^{III} complexes. For the moment only σ-bonding is taken into account. Eigenfunctions and respective covalency parameters (see section 3.1) are also given in these Figures.

We consider the $5d_{z^2}$ orbitals in both diagrams as non-bonding. Actually $5d_{z^2}$ mixes with 6s and the total symmetric combination of ligand orbitals, all belonging to the same irreducible representation, but MO calculations indicate this mixing to be small [Ba67,Re74].

a Isomer shift

The nuclear radius R, which appears in the expression for the IS (Eq. 3.2) is given by [Ko58]

$$R = 1.2 \; A^{\frac{1}{3}} \; 10^{-13} \; cm$$
$$= 6.98 \quad 10^{-13} \; cm \quad , \tag{5.3}$$

where $A = 197$ is the atomic mass. After substitution, Eq. 3.2 becomes:

$$IS = 5.40 \; 10^{-23} \; (\Delta R/R) \; \Delta|\Psi(0)|^2 \; mm/sec \quad , \tag{5.4}$$

where $\Delta|\Psi(0)|^2 = |\Psi_a(0)|^2 - |\Psi_s(0)|^2$ is given in units of cm^{-3}. Estimates of $\Delta R/R$, as reviewed by Roberts [Ro74], range from 0.15×10^{-3} to 0.25×10^{-3}

$|\Psi(0)|^2$ mainly depends on the atomic 6s and 5d populations. Increase of the latter causes a decrease of $|\Psi(0)|^2$ by shielding of the s-electrons off the nucleus. The positive contribution of 6p electrons through relativistic effects is almost cancelled by the negative contribution through screening [Fa69]. Therefore it will be neglected. $|\Psi(0)|^2$ also depends on the total charge of the gold atom. Thus following a method used by de Vries, Trooster and Ros [Vr75] for Sn and Fe we can write:

$$|\Psi(0)|^2 = P_o + P_s N_s + P_d(N_d-8) + P_c N_s [N_s + (N_d-8) + N_p], \tag{5.5}$$

where P_o, P_s, P_d and P_c are adjustable constants and N_s, N_d and N_p the number of 6s, 5d and 6p electrons respectively. Using the relativistic Dirac-Fock values of the s-electron density $|\Psi(0)|^2$, given by Faltens [Fa69] for a number of configurations (see Table 5.11), we determined the constants P by a least squares fit:

$$|\Psi_s(0)|^2 = \{129102.19 + 13.25 \ N_s - 1.45 \ (N_d-8)$$
$$- 1.79 \ N_s \ [\ N_s + (N_d-8) + N_p \ ] \} \cdot 10^{26} \ cm^{-3} \quad . \quad (5.6)$$

Table 5.11 *s-electron density at the nucleus of gold*

Configuration	$10^{31} \sum\limits_{n=1}^{5,6} |\Psi_{ns}(0)|^2$ (cm^{-3}) [1]	calculated with Eq. 5.4
$5d^{10}6s$	1.291068257	1.291072
$5d^9 6s$	1.29110182	1.291104
$5d^8 6s$	1.29113758	1.291136
$5d^9 6s^2$	1.29116725	1.291165
$5d^9 6p$	1.29100509	1.291007
$5d^{10}$	1.29099743	1.290993

[1] [Fa69]

With Eq. 5.4 and 5.6 and the atomic populations given by the covalency parameters of Figure 5.17, we obtain for the IS of Au^{I} compounds with respect to the configuration $5d^8$:

$$IS(Au^{I}) = 5.40 \ \{26.50 \ \lambda_s^2 - 2.90 - 7.16 \ \lambda_s^2 \ [\ \lambda_s^2 + 1 + \lambda_z^2 \ ]$$
$$\times \ (\Delta R/R) \ 10^3 \ mm/sec \qquad , \qquad (5.7)$$

and in the same way for Au^{III} compounds with the covalency parameters of Figure 5.19:

$$IS(Au^{III}) = 5.40 \ \{26.50 \ \lambda_s^2 - 2.90 \ \lambda_{xy}^2$$
$$- 7.16 \ \lambda_s^2 \ [\ \lambda_s^2 + \lambda_{xy}^2 + 2\lambda_{x,y}^2 \ ] \} \ (\Delta R/R) \ 10^3 \ mm/sec \quad .$$
$$(5.8)$$

b. Quadrupole Splitting

With a nuclear quadrupole moment of $Q = 0.594 \ 10^{-24} \ cm^2$ [Ch66] Eq. 3.7 yields:

$$QS \ (mm/sec) = 1.15 \ 10^{-22} \ V_{zz} \quad , \tag{5.9}$$

where V_{zz} is given in units of V/m^2 and $\eta = 0$ because of the assumed axial symmetry. A complete treatment of the electric field gradient according Eq. 3.10 gives:

$$V_{zz} = [1 - R] \ V_{zz}^{val} + [1 - \gamma] \ V_{zz}^{latt} \quad , \tag{5.10}$$

where the two terms describe the contributions of the valence electrons and the charges in the lattice. A relativistic value of $\gamma = -65.58$ has been calculated by Feiock and Johnson [Fe69]. With this value we obtain in case of four charges of one electron in a square around the nucleus at a distance of 2.3 Å (the geometry of $AuCl_4^-$) : $(1 - \gamma)V_{zz}^{latt} = 3.05 \ 10^{22} \ V/m^2$ resulting in a QS of 3.5 mm/sec (Eq. 5.9). The charges in covalent compounds are generally much smaller. Therefore the lattice contribution is estimated to be an order of magnitude smaller than the contribution of the valence electrons and will be neglected. The shielding factor R is not known. In fact it is included in the value of the quadrupole moment given above, which has been determined by atomic beam experiments on the $5d^9 6s^2 \ ^2D_{5/2}$ [Ch66] and $5d^9 6s^2 \ ^2D_{3/2}$ [B167] state of gold without taking into account this shielding.

Using Eq. 5.9 and Eq. 3.14, the values of Table 3.1 and the covalency parameters of Figure 5.17 we obtain for Au^I complexes:

$$QS(Au^I) = -1.79 \ \lambda_z^2 < r^{-3} >_{6p} \ mm/sec \quad . \tag{5.11}$$

In the same way we obtain for Au^{III} complexes using the covalency parameters of Figure 5.19:

$$QS(Au^{III}) = 1.28 \ (\lambda_{xy}^2 - 1) < r^{-3} >_{5d} + 1.79\lambda_{x,y}^2 < r^{-3} >_{6p} \ mm/sec \quad , \tag{5.12}$$

where $< r^{-3} >$ is given in units of a_o^{-3}. An experimental value of $< r^{-3} >_{5d}$ = 12.3 a_o^{-3} was obtained from the magnetic dipole hyperfine interaction constants of both $5d^96s^2$ ^2D_J states of gold. Relativistic calculations yielded 14.4 a_o^{-3} and revealed a minor charge dependence of $< r^{-3} >_{5d}$ [Fa69]. We shall adopt the experimental value for the calculations in section 5.4.c.

It proved to be difficult to obtain a reliable value of $< r^{-3} >_{6p}$. From the fine structure and the magnetic hyperfine coupling constants of the $5d^{10}6p$ $^2P_{3/2}$- and $5d^{10}6p$ $^2P_{1/2}$-states, given by Goldman et al. [Go69], we derive the values 4.45 a_o^{-3}, 6.30 a_o^{-3} and 2.49 a_o^{-3} respectively. For only three states the relativistic Dirac-Fock values are available: $< r^{-3} >_{6p}$ ($5d^76p$) = 21.30 a_o^{-3}, $< r^{-3} >_{6p}$ ($5d^86p$) = 15.55 a_o^{-3} and $< r^{-3} >_{6p}$ ($5d^96p$) = 9.72 a_o^{-3} [Fa69]. Extrapolation to $5d^{10}6p$ yields a value of 3.9 a_o^{-3}, which agrees well with the experimental values. Thus for neutral gold $< r^{-3} >_{6p}$ ~ 4 a_o^{-3}, increasing substantially with increasing charge. As there are no reliable values for other states available, we shall treat $< r^{-3} >_{6p}$ as a parameter.

c QS IS variation with covalency

The number of unknowns in the right hand side of Eqs. 5.7, 5.8, 5.11 and 5.12 is too large for a meaningful comparison with the experimentally measured QS and IS. As a first simplification we may assume all covalency parameters to be equal and given by one parameter λ^2. Essentially the same approach was used by Faltens and Shirley. These authors calculated the difference in IS and QS for Au^I complexes with configurations $5d^{10}$ and $5d^{10}6s6p$ respectively, and similarly for Au^{III} complexes with configurations $5d^8$ and $5d^96s6p^2$. $\Delta R/R$ and $< r^{-3} >_{6p}$ were used as parameters. This is equivalent with λ^2 = 0 and 0.5 in Eqs. 5.7 and 5.11, and Eqs. 5.8 and 5.12 respectively. Comparison of the calculated ratios $\Delta IS/\Delta QS$ with Eq. 5.1 and 5.2 then gives values of $\Delta R/R$ and $< r^{-3} >_{6p}$.

However the IS is a quadratic function of λ^2 (Eq. 5.7 and 5.8) whereas QS has a linear dependence on λ^2 (Eq. 5.11 and 5.12) assuming $< r^{-3} >_{6p}$ is constant. Therefore the method used by Faltens and Shirley cannot lead to a meaningful result. Moreover the assumed configuration for the most covalent Au^I compound ($5d^{10}6s6p$) should have an IS approximately equal to that of gold metal ($5d^{10}6s$), which is -1.2 mm/sec. It can be seen in Figure 5.15 however that practically every gold complex has an IS larger than this value.

A possible explanation of the observed IS and QS values can be found if we assume that for a given oxidation state the effective charge on the gold atom does not vary significantly due to π-back-donation. This means first of all that the terms in square brackets in Eq. 5.7 and 5.8 are approximately constant, which explains the observed linear relationship between IS and QS. Secondly the proposed mechanism results effectively in a transfer of d-electrons into the s-shell of the gold atoms, which explains at least qualitatively the values of the IS with respect to gold metal.

A further indication for the importance of π-back-donation can be obtained from the range of QS values observed within one oxidation state. If these were to be explained by Eq. 5.11 and 5.12 unreasonably large values of $< r^{-3} >_{6p}$ are required. With π-back-donation part of the QS is due to reduction of the electronic charge in a plane perpendicular to the coordination axis in case of linear coordinated Au^I compounds and along the symmetry axis in case of planar 4-coordinated Au^{III} compounds.

To account for π-back-donation in the expressions for IS and QS even more covalency parameters are required. A few general observations are none the less possible: Both IS and absolute value of QS increase with covalency. For Au^{III} QS is negative for highly ionic compounds as it is due to a d_{xy}-hole in the 5d-shell. This negative contribution to QS is outweighted by the positive contribution of the 6p electrons in more covalent gold compounds (Eq. 5.12). For Au^I compounds the absolute value of the QS increases with increasing covalency (Eq. 5.11), but is negative. This negative sign of QS has recently been confirmed experimentally by Mössbauer measurements on single crystals of $KAu(CN)_2$ [Pr75].

On the basis of the theory we may arrange the ligands according to increasing covalency in σ-bonding with gold corresponding with increasing Mössbauer parameters. Such arrangement concurs with increasing σ-donor power or inductive effect of the ligands towards gold. Due to the scatter of the data in Figure 5.15 the order is only approximate:

$$F < I, Br, Cl < S, Se, O < N, C \quad . \tag{5.13}$$

In the spectrochemical series, the ligands are arranged according to increasing d-MO splitting Δ [Jo62]. The order of the bonding atoms of the ligands is:

$$I < Br < Cl < S < F < O < N < C \quad . \tag{5.14}$$

The close similarity with the series (5.13) is noteworthy. As pointed out by Bartunik et al. [Ba70] the inductive effect of the ligands increases also the ligand field splitting Δ (Figure 5.19) by lowering the energy of the bonding orbitals and raising the energy of the anti-bonding orbitals, in particular b_{2g}^{*}. The apparent exception of Fluorine in Eq. 5.14 compared with Eq. 5.13) cannot be understood within this picture. It is not clear whether electrostatic- or π-bonding effects or the influence of the coordination geometry are responsible for the position of Fluorine.

5 5 Considerations in some detail

a AuX_4^- with X = Br,Cl (Table 5 2)

The average IS and QS of $AuCl_4^-$ are 0.82 mm/sec and 1.35 mm/sec and for $AuBr_4^-$ 0.71 mm/sec and 1.31 mm/sec respectively. The difference between these average values is smaller than the variation with the cation. Therefore the Mössbauer effect cannot reveal differences in bonding between bromine and chlorine in AuX_4^-. The variation with the cation reflects the influence of the lattice on the Mössbauer parameters, which is here more important than in the more covalent compounds.

b Bis-dithiolato Au^{III} complexes (Table 5 3)

The Mössbauer parameters of the (cdc) compound are comparable with the average IS and QS of the (dtc) compounds· 2.17 mm/sec and 2.90 mm/sec respectively. This can be understood as follows: although (dtc) is a mono-negative ligand and (cdc) a dinegative one, they are the same at the site of the gold atom.

cdc   dtc
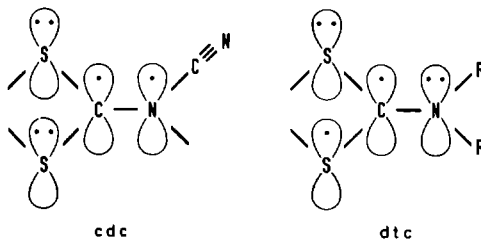
Both ligands have comparable σ-donor capacity, for which the binding atoms are of paramount importance. Secondly, the planar π-systems have the same geometry and contain in both molecules six electrons. The similarity between the Mössbauer parameters of the (dtc) and (cdc) compounds indicates a minor influence of the cyanide group on the π-bonding of the latter.

The larger IS in the 1,2-dithiolene compounds (mnt and tdt) as compared with 1,1-dithiolates must be attributed to a larger π-back-bonding. This agrees with the redox behaviour, studied by Van der Linden [L173]. There it was concluded that the extend of electron delocalization in 1,1-dithiolates is less important than in 1,2-dithiolenes. The expected increase of QS with increased π-back-donation is not observed. However, the QS is more sensitive to the coordination geometry than the IS and the deviation of D_{4h} symmetry in the AuS_4-moiety of the 1,1-dithiolate compounds is larger than in the 1,2-dithiolenes.

It appears from Figure 5.15 that all the compounds, listed in Table 5.3 have IS and QS values, which fall in the range, expected for planar 4-coordinated Au^{III} compounds. Thus no indication is found for an ambiguity in the oxidation state as suggested in the introduction of this chapter.

c Di halo and dimethyl dithiocarbamates (Table 5 4)

The Mössbauer parameters of $X_2Au(R_2dtc)$ with X = Br,Cl are approximately equal to the arithmetical average between the parameters of AuX_4^- (Table 5.2) and $Au(R_2dtc)_2^+$ (Table 5.3), in agreement with the average-environment-rule mentioned in section 5.3. The large inductive effect of the methyl groups towards gold increases the QS as well as the IS compared with bromine and chlorine.

d Gold(I) complexes with bidentate sulphur-donor ligands (Table 5 5)

The ligands in the compounds listed in Table 5.5 coordinate through sulphur atoms of which the σ-donating character is increased by the π-acceptor properties of the complete ligand. Thus an arrangement corresponding with increasing IS shift will reveal the increasing -acceptor properties

$$WS_4^{2-} < dtp < xan < CS_3^{2-} < dtc \quad . \tag{5.15}$$

The QS increases in the same order. This is expected, when the coordination geometry is the same. Thus in the WS_4^{2-}, xan and CS_3^{2-} compounds the gold atom will be linear coordinated with two sulphur atoms. Hence the compounds must have a polymeric nature. Since the dtp and dtc compounds are known to be dimers, we propose the following structures:
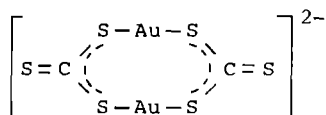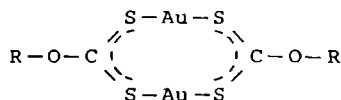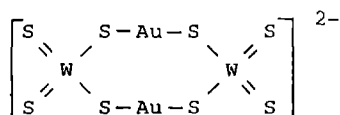
The SWS (or SCS) planes might be rotated with respect to each other, resulting in a short metal-metal distance, as is the case in Au(dtc) (Figure 5.5).

The short Au-Au distance in dtc and dtp has led to discussions on a metal-metal interaction [He61,La72]. A Raman-study of Au(dtc) [Fa71] suggests that this interaction is fairly weak. Chemical bonding between the gold atoms should increase the electronic charge perpendicular to the coordination axis and thus reduce the QS. It can be seen in Figure 5.15 that QS and IS fall in the range of other linear coordinated Au^I compounds. Thus no evidence is obtained for a gold-gold bond.

From the structures of the compounds, given in section 5.2, it appears that a Au-S-C (or Au-S-P) angle of about $90°-100°$ is highly favourable. This angle is somewhat smaller in the strained four-membered-rings of the Au^{III}-dtc compounds than in more-membered-rings. Thus σ-donation is accomplished through the p-orbitals of sulphur rather than through sp^2 hybrids. Therefore we believe, that the short Au-Au distance is a consequence of this preferred Au-S-C angle combined with a linear coordination of gold(I), rather than caused by a metal-metal bond. Indeed the corresponding 1,2-dithiolene dimer appeared sofar to be inaccessible [Li76]: a S-S distance of 3.25 Å, combined with linear coordination at the gold site with Au-S = 2.25 Å and a Au-S-C angle of

$110°$ would result in a Au–Au distance of 1 Å, whereas the covalent radius of Au^I is 1.33 Å [Co67].

e Triphenylphosphine gold(I) complexes (Table 5 6)

Neglecting π-bonding effects we can arrange the ligands of the complexes in Table 5.6 according to increasing σ-donating power, corresponding with an increasing IS. For the bonding atoms we obtain:

$$I < Br < Cl \sim S \sim Se \sim O \sim N < C \qquad . \qquad (5.16)$$

Because the compounds are related, this arrangement is more detailed than the one obtained from the general observation about the results in section 5.3. For the QS the same order is observed with the apparent exception of Ph_3PAuI (see also section 5.5.g, below).

f Polynuclear organo-gold compounds (Table 5 7)

As expected, both the isomer shifts and quadrupole splittings listed in Table 5.7 are very large, due to the high degree of covalency when carbon is bound to gold.

For the bridging carbon atoms in these compounds a two-electron three-centre bond has been proposed [Ko74] as illustrated in Figure 5.20. Such an

○ C
○ Cu, Li
● Au
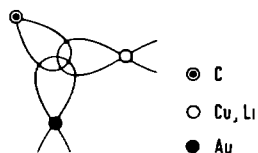
Figure 5.20 Two-electron three-centre bond of the bridging carbon atoms.

electron deficient bond cannot account for an IS and QS, which are larger than for example in $KAu(CN)_2$ (3.1 and 10.1 mm/sec [Fa70]), unless this bond is strongly polarized towards Li^+ or Cu^+ in agreement with the high electronegativity of gold. It can be seen in Table 5.7 that when carbon forms a bridge between Au and Cu smaller values of IS and QS are found than in case of Au

and Li, which agrees with the electronegativity difference between Li and Cu. Because of the availability of large π-systems in the phenyl-rings π-back-bonding must be considered in an explanation of the large QS and IS.

Except for the compounds (dmap)Au and (dmamp)Au the IS and QS values fall in the range of linear coordinated Au^I compounds (see Figure 5.15). Thus in the hexameric cluster the gold atoms must occupy the apical positions, in agreement with the high tendency of Au^I to have a linear coordination. Moreover there is no indication for a metal-metal bond on the same grounds as in Au(dtc). The small difference between the Mössbauer parameters of $(dmap)_4 Au_2 Cu_4 I_2$ and $(dmap)_4 Au_2 Cu_4 (otf)_2$ indicates a weak interaction or no interaction at all between the equatorial copper atoms and the apical gold atoms. Comparing $(dmamp)_4 Au_2 Li_2$ and $(dmap)_4 Au_2 Li_2$ it is not clear whether inductive- or conjugation-effects of $- N(CH_3)_2$ at the α-position of the phenyl-ring increase the Mössbauer parameters of the latter. The more so as the influence of the coordination of nitrogen with lithium on the QS and IS of the gold atom cannot be estimated.

In the compounds (dmap)Au and (dmamp)Au a relatively small QS is found compared with the other compounds in Table 5.7. This is indicative for a more spherical surrounding in agreement with the proposed polymeric structures.

g. Some additional compounds (Table 5.8)

The IS of the trigonal planar Au^I compound $AuCl(PPh_3)_2$ is exceptionally small compared with $AuCl \cdot PPh_3$. This cannot be understood in terms of three equivalent σ-bonds involving the gold 6s and 6p orbitals, because in that case about the same QS and IS values should be found as in the case of two σ-equivalent bonds. It is worthwhile to note that a similar combination of large QS and small IS is found for Ph_3PAuI (Table 5.6). It is tempting to speculate that a trigonal complex was measured instead of the two coordinated one.

5.6 Summary

The Mössbauer parameters of linear gold(I) and square planar gold(III) compounds were found to obey the previously established linear correlation between the IS and QS. This relationship could be explained using a MO model

with covalency entered as parameter.

To understand the large extend of the IS and QS variations within one oxidation state as well as the linearity of the IS-QS relationship it was necessary to take into account π-back-donation, by which the charge of the gold atom remains approximately constant. One can picture the effect of σ-bonding and π-back-bonding in the following way: for linearly coordinated Au^I there is an electron charge flow along the coordination axis towards gold, but at the same time the same amount of electronic charge is withdrawn from a plane, perpendicular to the symmetry axis. Once the Au^{1+} ion is linearly coordinated in this way, there is no possibility for additional bonding, even though there might be a close approach of other atoms. Similarly in planar 4-coordinated Au^{III} compounds an increase of electronic charge in the coordination plane is accompanied by a decrease of the electronic charge along the symmetry axis.

In a more detailed inspection of related compounds it was found that the Mossbauer effect could not reveal a difference in bonding between bromine and chlorine in AuX_4^-. The Mössbauer parameters of bis-dithiolato gold(III) complexes fall in the range, expected for Au^{III} compounds and we observed no special effect of the extended π-system in these ligands. The Au^I complexes with bi-dentate sulphur-donor-ligands were proposed to be dimers having a short Au-Au distance as is the case in Au(dtc) and Au(dtp). However, no evidence was obtained for a Au-Au bond. The bi-dentate sulphur-donor-ligands could be arranged according to increasing π-acceptor properties.

Exceptionally large Mossbauer parameters were found when gold was bound to a carbon atom of a phenyl-ring, indicating a high degree of covalency as expected in organo-gold compounds.

Finally the trigonal Au^I compound $(Ph_3P)_2AuCl$ was found to be characterized by a small IS and a large QS.

CHAPTER 6

DYNAMICAL BEHAVIOUR OF GOLD IN MOLECULAR CRYSTALS

6 1 Introduction

The crystals of most gold compounds are built up from molecules. The dynamical behaviour of atoms in such systems of generally low symmetry is quite complicated. Some aspects of it may be clarified by the Mössbauer effect, which probes the mean square displacement $< x^2 >$ of one particular kind of atom (the Mossbauer nucleus) in the lattice. The value of $< x^2 >$ is obtained from the Mossbauer fraction f by means of Eq. 3.42, and f can be determined from the relative absorption intensity of the lines in the spectrum as explained in section 4.4.

Our interest in this subject stemmed from the observation, that in the mixed valence gold compounds, studied by us, the relative absorption intensity of the square planar 4-coordinated Au^{III} site is about twice the absorption intensity of the linear 2-coordinated Au^{I} site, whereas we found in a compound, containing two 4-coordinated Au^{III} sites, approximately equal intensities for both sites. This is illustrated in Figure 6.1. A correlation between the Mossbauer fraction and the coordination number of the gold atom seemed a possible explanation· a 2-coordinated atom might have a larger vibrational amplitude than a 4-coordinated one. However the intramolecular binding forces are typically two orders of magnitude larger than the inter-molecular (Van der Waals) forces and molecular crystals can therefore be thought of as constructed from rigid molecules, which vibrate as a whole. This is a rather generally held viewpoint [Go68] , strongly advocated in the work of Herber and Hazony [Ha73,Ha74,Re75] . Nevertheless the intramolecular vibrations cannot be neglected. The arguments, used by Kagan and Iosilevskii [Ka62] for impurities in a crystal, may be applied here For the 3N (N = number of molecules in the lattice) intermolecular vibrational modes, the energy assignable to a single molecule is of the order of 1/N of each mode. On the other hand, a considerable part of the energy of localized intra-molecular vibrations, although few in number, is associated with the motion of the Mossbauer nucleus. Thus the contribution of inter- and intramolecular vibrations to $< x^2 >$ can be expected to be of the same order of magnitude.

To determine the characteristic frequencies of the inter- and intra-
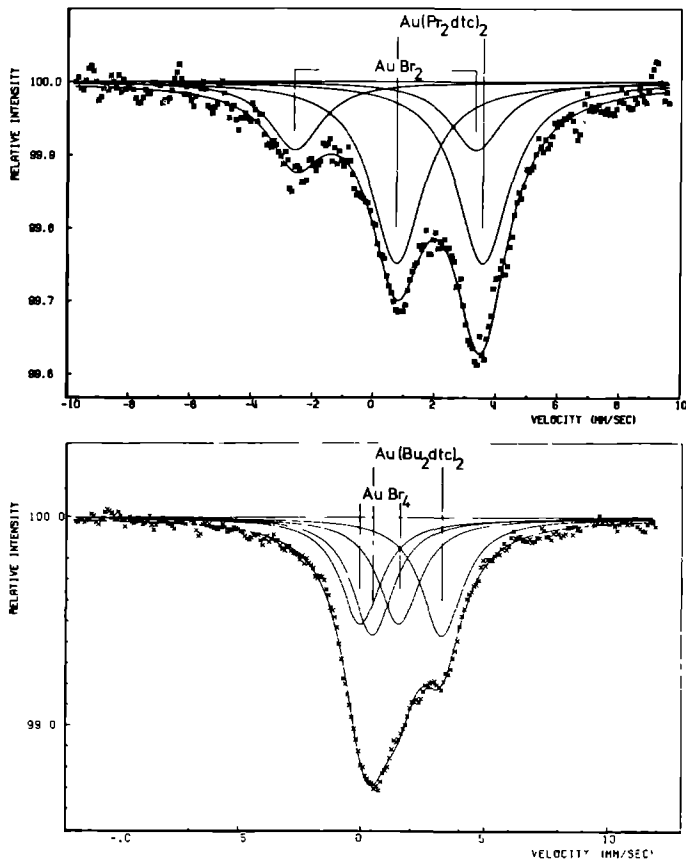
Figure 6.1 Mössbauer spectra of $[Au^{III}(Pr_2dtc)_2]^+ \cdot [Au^IBr_2]^-$ (top) and $[Au^{III}(Bu_2dtc)_2]^+ \cdot [Au^{III}Br_4]^-$ (bottom). The drawn line is a least squares fit with two pairs of Lorentzian shaped absorption lines. The lines of each pair were constrained to have equal intensities and widths. The values of the Quadrupole Splitting (QS) and Isomer Shift (IS) of a number of gold compounds containing two sites are given in Table 6.1 together with the intensity ratios of both sites. The absorption lines are assigned on the basis of the close agreement of the QS and IS values with those of the compounds containing only one of the gold complexes (see chapter 5).

87

Table 6.1 Mössbauer data of mixed valence gold compounds at $4.2^{\circ}K$.

Compound	Quadrupole Splitting (mm/sec)	Isomer Shift (mm/sec)	Intensity ratio [1] Au^{III}/Au^{I}
$[AuCl_2]^-$ ·	6.43 ± 0.08	0.74 ± 0.05	3.3
$[(Bu_2dtc)_2Au]^+$	2.75 ± 0.08	2.00 ± 0.05	
$[AuI_2]^-$ ·	5.75 ± 0.08	0.53 ± 0.05	2.2
$[(Bu_2dtc)_2Au]^+$	2.76 ± 0.08	2.00 ± 0.05	
$[AuBr_2]^-$ ·	6.2 ± 0.3	0.4 ± 0.1	2.6
$[(Pr_2dtc)_2Au]^+$	2.7 ± 0.1	2.0 ± 0.1	
$[AuBr_2]^-$ ·	6.5 ± 0.2	0.5 ± 0.1	4.0
$[(Ph_2dtc)_2Au]^+$	2.29 ± 0.03	1.83 ± 0.03	
$(C_7H_7)_2SAuCl$ ·	6.35 ± 0.02	1.05 ± 0.01	2.0
$(C_7H_7)_2SAuCl_3$	2.16 ± 0.02	1.38 ± 0.01	
$(C_7H_7)_2SAuBr$ ·	5.92 ± 0.03	0.57 ± 0.02	2.0
$(C_7H_7)_2SAuBr_3$	1.93 ± 0.03	0.94 ± 0.02	
$[AuBr_4]^-$ ·	1.53 ± 0.08	0.91 ± 0.05	1.2 [2]
$[(Bu_2dtc)_2Au]^+$	2.81 ± 0.08	2.04 ± 0.05	

[1] area ratio of the least-square-fitted Lorentzians

[2] area ratio of cation : anion

molecular vibrations from the temperature dependence of the Mössbauer fraction
we developed a simple model, which is presented in the next section. Benzyl-
sulphide dihalo gold compounds present a suitable test case. They consist of
separate molecules of $(C_7H_7)_2SAu^IX$ and $(C_7H_7)_2SAu^{III}X_3$ (X = Br,Cl), packed
in rows in which alternating gold atoms have valencies I and III [Br52]. As
usual the Au^I site has a linear 2-coordination and the Au^{III} site a planar
4-coordination. Moreover the monovalent and trivalent species can be studied
in pure form. The results of our measurements on these compounds as well as
some other compounds are discussed in this chapter.

6.2 Inter- and intramolecular vibrations

In the following it is assumed that intra- and intermolecular vibrations
do not couple [Go62], so that we can write:

$$< x^2 > = < x^2 >_1 + < x^2 >_m \tag{6.1}$$

According to Eq. 3.42 this leads to:

$$f = f_l \cdot f_m \qquad\qquad (6.2)$$

Here $< x^2 >_m$ is the mean square displacement of the Mossbauer nucleus from its equilibrium position within the molecule and $< x^2 >_l$ is the mean square displacement of the molecule as a whole due to the lattice vibrations. The approximation of Eq. 6.1 is based on an assumed energy gap between the low lying intermolecular vibrations and the high energy intramolecular vibrations. Symmetry arguments can sometimes be used to argue this separation, but are not applicable here, because of the low symmetry, encountered in Au compounds studied by us.

For reasons of simplicity we assume that all vibrations are isotropic, so that Eq. 3.43 for $< x^2 >$ applies. Later we will briefly discuss some consequences of this assumption. According to Eq. 3.43 $g(\omega)$ is weighted by ω^{-1}. Thus f_l will be determined mainly by the low frequency (acoustical) intermolecular vibrations, for which we shall use the Debye model given in Eq. 3.48. Here m has to be replaced by the molecular mass M, so that the temperature dependence of f_l is given by.

$$f_l(T) = \exp\left\{-\frac{\hbar^2}{2M\lambda^2} \cdot \frac{3}{2k\theta_D}\left(1 + 4\frac{T^2}{\theta_D^2}\int_0^{\theta_D/T}\frac{xdx}{e^x-1}\right)\right\} \qquad (6.3)$$

The intramolecular vibrations are discrete. Thus for each of these vibrational modes the Einstein model can be applied as given in Eq. 3.46 and $f_m(T)$ is given by:

$$f_m(T) = \exp\left\{-\frac{\hbar^2}{2m'\lambda^2} \cdot \frac{1}{k\theta_E}\left(\frac{2}{\exp(\theta_E/T)-1} + 1\right)\right\} \qquad (6.4)$$

where m' is the effective mass, associated with the mean square displacement $< x^2 >_m$. With the definition of $< x^2 >_m$, given above, m' is defined by:

$$< x^2 >_m = \frac{\hbar}{2m'\omega_o}(n + \tfrac{1}{2}) \qquad (6.5)$$

89

This is the expression for $< x^2 >$ of an harmonic oscillator with frequency ω_o and quantum number n (see for example White [Wh66]).

For the calculation of m' it is illustrative to consider the molecule AB_4 in which A has a planar 4-coordination. The nine normal modes of this molecule are measured for $AuBr_4^-$. In four modes $(A_{1g}, B_{1g}, B_{2g}$ and $B_{2u})$ the amplitude of the central atom is zero. Of the remaining five modes we retain only the one with the lowest frequency (A_{2u}).

A_{1g}, 212 cm^{-1} A_{2u}, 87 cm^{-1} B_{1g}, 102 cm^{-1} B_{2g}, 196 cm^{-1}

B_{2u} E_u, 252 cm^{-1} E_u, 139 cm^{-1}
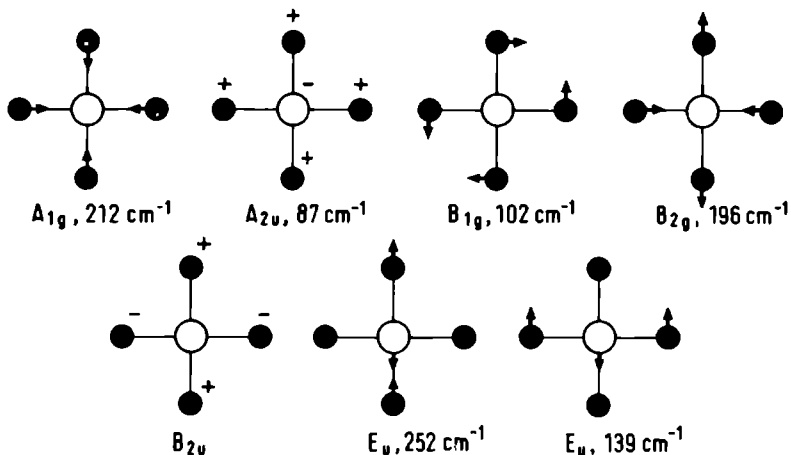
Figure 6.2 Normal modes of AB_4 (D_{4h}). The frequencies given are those of $AuBr_4^-$ [Si66].

Keeping the centre of mass at rest, the frequency ω_o, the reduced mass μ and the mean square displacement $< d^2 >$ of the harmonic oscillator A_{2u} are given by the familiar expressions (see for example Gans [Ga71]).

$$\omega_o = \sqrt{\frac{4q}{\mu}} \qquad , \qquad (6.6)$$

$$\mu = \frac{4m_B m_A}{4m_B + m_A} \qquad , \qquad (6.7)$$

$$< d^2 > = \frac{\hbar}{2\mu\omega_o} (n + \tfrac{1}{2}) \qquad , \qquad (6.8)$$

where q is the force constant of one A-B bond, m_A and m_B are the masses of atoms A and B and d is defined in Figure 6.3
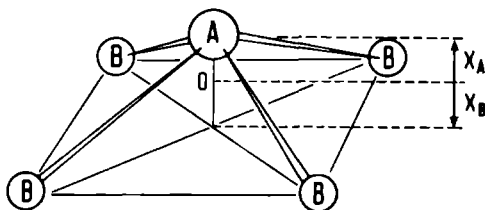
Figure 6.3   The A_{2u} vibrational mode of AB_4. The origin O of
the coordinate system is at the centre of mass.
The coordinates of the atoms are shown as x_A and
x_B; $d = x_A - x_B$.

We are interested in the mean square displacement of atom A, which is given by (compare Figure 6.3):

$$< x_A^2 > = \{ \frac{4m_B}{4m_B + m_A} \}^2 < d^2 > \quad . \tag{6.9}$$

By comparing this equation with Eq. 6.5 we see with the aid of Eqs. 6.7 and 6.8 that:

$$m' = \frac{m_A + 4m_B}{4m_B} \cdot m_A \tag{6.10}$$

A similar expression can be derived for linearly coordinated Au^I compounds.

When complex ligands are coordinated we shall include in the calculation of m' (Eq. 6.10) only the coordinating atoms of the ligands. This simplification is generally used as a first approximation in the calculation of force constants from Infra Red- and Raman data [Si66] .

The implications of Eqs. 6.2, 6.3 and 6.4 may be better understood in the low temperature limit. For $T \ll \theta_D$ and $T \ll \theta_E$ we may approximate the integral in Eq. 6.3 by $\pi^2/6$ and obtain:

$$f_1 \ (T \ll \theta_D) = \exp \left\{ -\frac{\hbar^2}{2M\lambda^2} \cdot \frac{3}{2k\theta_D} \ (1 + \frac{2\pi^2}{3} \frac{T^2}{\theta_D^2}) \right\} \quad , \tag{6.11}$$

$$f_m \ (T \ll \theta_E) = \exp \left\{ -\frac{\hbar^2}{2m'\lambda^2} \cdot \frac{1}{k\theta_E} \right\} \tag{6.12}$$

In these equations it can be seen that for molecular solids the effect of a lower θ_D, due to weaker binding compared with ionic or covalent solids, is offset by a larger mass of the structural units. Because $\theta_D < \theta_E$, the temperature dependence of f will be mainly determined by f_1, whereas f_m contributes a constant factor through the zero point vibrations.

If the Mossbauer nucleus is coordinated with atoms, which are light with respect to the atomic mass of the Mossbauer nucleus, m' tends to become very large and f_m approaches 1. However, in that case it is not proper to consider only the binding atoms of the ligands in the calculation of m'. The lower limit of m' is the atomic mass of the Mossbauer nucleus, which limit is reached when atoms are coordinated, which are very heavy compared with the Mossbauer nucleus. Thus in gold compounds f_m is expected to be large unless θ_E is small. It should be noted, however, that for light Mossbauer nuclei, e.g. Fe and Sn, m' is smaller and consequently f_m is more important.

6 3 Results and discussion

a Temperature dependent measurements

Temperature dependent measurements were carried out on the compounds listed in Table 6.2. The Quadrupole Splitting (QS) and Isomer Shift (IS) values, also given in Table 6.2, agree well with the QS-IS relations for Au^I and Au^{III} compounds, discussed in chapter 5. The difference between the QS and IS of the bromo-gold-dibenzylsulphides in the pure- and mixed valence compounds is small, indicating that we are dealing with the same structural units.

In case of a clear overlap of the absorption lines, as illustrated in Figure 6.4, we could determine the effective absorber thickness and conse- quently the Mossbauer fraction from a least squares fit with the transmission integral (Eq. 4.11), even for thin samples. The initial values of the free
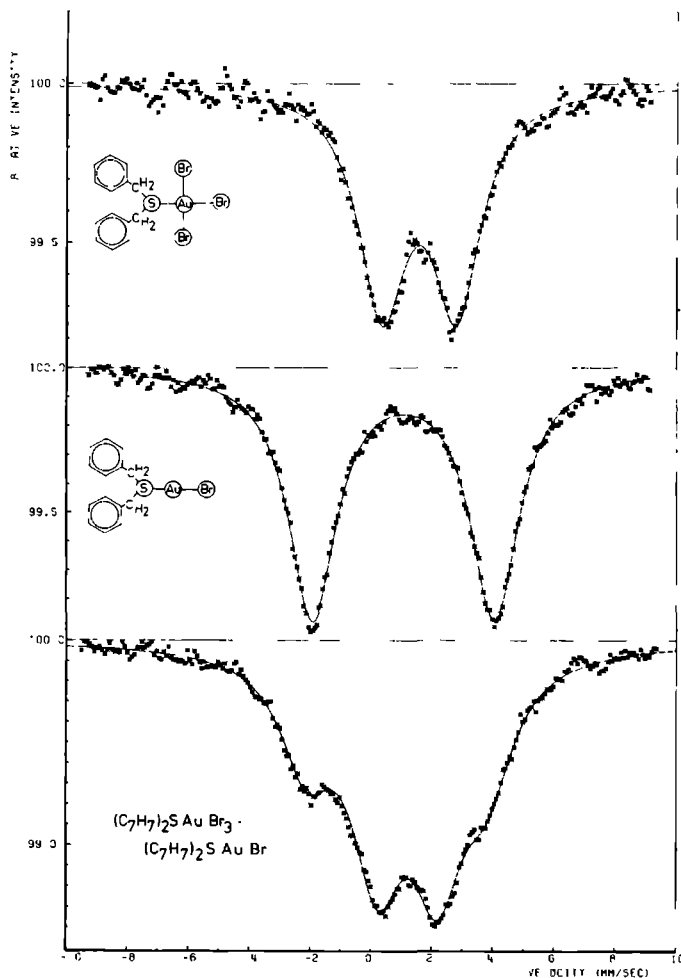
Figure 6.4 Mössbauer spectrum of the mixed valence gold compound: $(C_7H_7)_2SAuBr_2$ (bottom). The spectra of the monovalent and tervalent species are shown at the top. The drawn lines are least squares fits of the transmission integral.

parameters B, F_s, t_a and v_i were obtained from a least squares fit of Lorentzians and from the measured time dependence of F_s, as explained in section 4.4. In other cases, when the spectra consisted of well separated absorption lines, the effective absorber thickness was determined from the area of the least square fitted Lorentzians (see section 4.4).

93

The two spectra, obtained in one measurement, were treated independently and the results agreed within the limits of the estimated (see section 4.3) errors. The average of the values of f, obtained from both spectra, are given in Figure 6.5. The values of f(T) thus found were subsequently fitted with
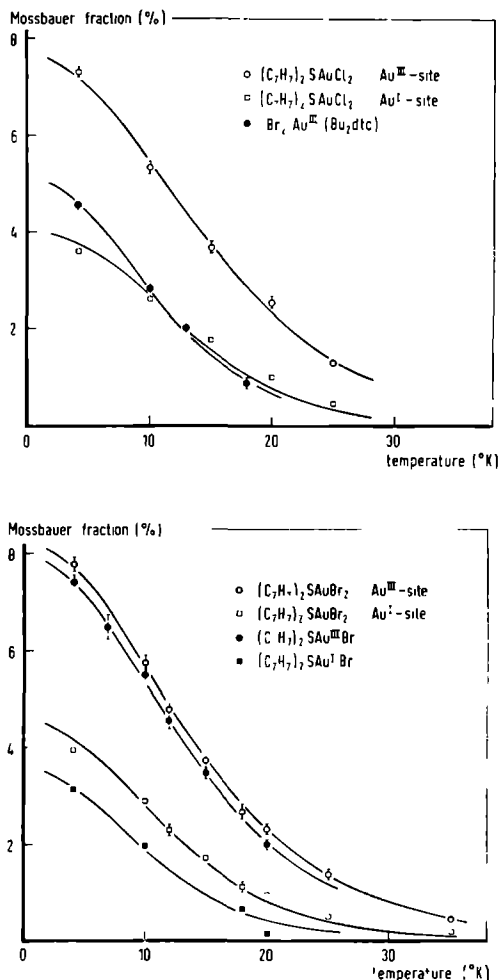
Figure 6.5   Temperature dependence of the Mössbauer fraction.
The drawn lines are least squares fits, discussed
in the text.

Eq. 6.2, using Eq. 6.3 for f_l and Eq. 6.4 for f_m. θ_D and θ_E were the only

Table 6.2 Mössbauer data for temperature dependent measurements.

Compound	Ref. for preparation and basic properties	Gold content (mg/cm²)	QS (mm/sec)	IS (mm/sec)	M	m'	θ_D (°K)	θ_E (°K)	$f'_l(4°K)$ %	$f'_u(4°K)$ %	$f'(4°K)$ %
Au^I-site			5.92	0.57	491	543		72	10.9	38.8	4.2
$(C_7H_7)_2SAuBr_2$	Br52	136.3					53				
Au^{III}-site			1.93	0.94	651	340		124	18.7	41.2	7.7
$(C_7H_7)_2SAuBr$	Br52	186.8	5.99	0.96	491	543	48	71	8.5	38.0	3.2
$(C_7H_7)_2SAuBr_3$	Br52	70.4	2.46	1.47	651	340	52	125	17.9	41./	7.5
Au^I-site			6.35	1.05	447	772		43	11.6	32./	3.8
$(C_7H_7)_2SAuCl_2$	He05,Br52	169.3					60				
Au^{III}-site			2.16	1.38	518	477		101	15.6	46.4	7.2
$(Bu_2dtc)AuBr_2$	Be70b	185.9	2.20	1.47	561	370	47	116	11.0	42.2	4.6

[1] Calculated with the values of the previous four columns

free parameters. The integral appearing in Eq. 6.3 was evaluated numerically using the Simpson integration technique [Cr66] The best values of θ_D and θ_E are given in Table 6.2 together with the values of M and m', used in Eqs. 6.3 and 6.4 respectively. In the mixed valence compounds the curves of both sites were fitted simultaneously, using one value of θ_D, because both molecules are confined in the same lattice.

The agreement between the values of θ_E found for the molecules $(C_7H_7)_2S$ AuBr and $(C_7H_7)_2SAuBr_3$ in the mixed valence and pure compounds is remarkably good.

As far as the Einstein temperatures is concerned, the measurements have been carried out in a temperature range, where Eq. 6.12 holds. From this equation can be seen that the value of θ_E, obtained from a least squares fit is inversely proportional to the choice of m'. Because we took into account only the binding atoms, the value of m' may be overestimated. This is certainly the case in $(C_7H_7)_2SAuCl_2$, where the binding atoms are relatively light, resulting in an underestimation of θ_E. Yet the values of θ_E indicate a higher intramolecular frequency for a 4-coordinated Au^{III} atom than for a 2-coordinated Au^I atom as expected, when the binding force constants are comparable. But one should consider these results with caution In the first place because of the approximations involved in the calculation of m'. Secondly because of the assumed isotropy of the vibrational amplitude. A vibrational anisotropy can be revealed in a powder absorber by unequal intensities of the lines of a quadrupole doublet. the Goldanskii-Karyagin [Go68] effect. However in case of gold the expected effect is small due to the M_1/E_2 mixture of γ-irradiation as was pointed out by Prosser, Wagner, Wortmann and Kalvius [Pr75]. These authors measured an intensity ratio of 1/3 between measurements perpendicular and parallel to the c-axis, whereas in a powder absorber of $KAu(CN)_2$ the intensity difference between the quadrupole lines was only 5%. Furthermore the anisotropy in the intramolecular displacement may be offset by anisotropy in the intermolecular displacement. Thus the fact, that we did not observe a Goldanskii-Karyagin effect within the accuracy of our measurements, is not conclusive about the assumed isotropy.

From the values of θ_E and θ_D as well as M and m' one can calculate f_m $(T = 4^\circ K)$ and f_l $(T = 4^\circ K)$ the molecular and lattice contribution to the Mossbauer fraction respectively. These are also listed in Table 6.2. From these values it follows that the observed intensity differences for Au^I and Au^{III} in mixed valence compounds are due to the difference in mass of the respective molecules and are not related with difference in intramolecular

Table 6.3   *Mössbauer fraction f of some Au^I compounds.*

Number referring to Figure 6.6	Compound	Formula weight (g/mol)	f (%)
1	$(dmap)_4Au_2Cu_4(otf)_2$	1427	8.3
2	$(dmap)_4Au_2Cu_4I_2$	1383	7.7
3	$(dmap)_4Au_2Cu_2$	1002	6.7
4	$(dmap)_4Au_2Li_2$	889	5.3
5	$(Ph_3P)_2AuCl$	757	5.8
6	$(dmap)AuPPh_3$	597	4.2
7	$Ph_3P\ AuI$	586	4.0
8	$Ph_3P\ AuSCN$	517	4.0
9	$Ph_3P\ AuCl$	495	3.8
10	$(C_7H_7)_2SAuBr_2(Au^I\text{-site})$	491	4.0
11	$(C_7H_7)_2SAuBr$	491	3.2
12	$Ph_3P\ AuCN$	485	3.0
13	$(C_7H_7)_2SAuCl_2(Au^I\text{-site})$	447	3.6
14	$(dmap)AuCN(C_6H_{11})$	426	3.9
15	$Au(dtp)$	410	2.3

Table 6.4   *Mössbauer fraction f of some Au^{III} compounds.*

Number referring to Figure 6.7	Compound	Formula weight (g/mol)	f (%)
1	$(C_7H_7)_2SAuBr_2(Au^{III}\text{-site})$	651	7.8
2	$(C_7H_7)_2SAuBr_3$	651	7.4
3	$(Bu_2dtc)AuBrI$	608	5.1
4	$(Bu_2dtc)AuBr_2$	561	4.6
5	$(Hep_2dtc)AuCl_2$	556	6.5
6	$(C_7H_7)_2SAuCl_2(Au^{III}\text{-site})$	518	7.3
7	$Bu_4N^+[Au(mnt)_2]^-$	477 [1]	4.4
8	$(CH_3)_2Au(Bu_2dtc)$	431	3.2
9	$(CH_3)_2Au(Pr_2dtc)$	403	2.9
10	$(CH_3)_2Au(Me_2dtc)$	347	4.0

[1] Formula weight of the anion

vibrational amplitudes. These seem to contribute a constant factor. On the other hand, the absolute value of the Mössbauer fraction cannot be understood in terms of intermolecular vibrations alone.

b Different compounds at 4 2°K

We have measured f (T = 4.2°K) for a large number of other gold compounds which were described in section 5.2. The conclusion that molecular mass is the dominant factor for the Mossbauer fraction is supported by these measure-ments: there is a clear relation between molecular mass and Mossbauer fraction listed in Tables 6.3 and 6.4. Assuming f_m (T = 4.2°K) to be constant for all compounds with the same oxidation state of gold, the Mossbauer fraction f is proportional to f_1 and from Eq. 6.11 it follows that $-\ln f \; (:) \; \frac{1}{M}$. This relation is reasonably fulfilled for Au^I complexes as can be seen in Figure 6.6.

Apparently the approximations hold less well for Au^{III} compounds (see Figure 6.7). It is interesting to note that for Au(dtp) (compound 15, Figure 6.6) the mass of the monomer has to be taken, in contrast with the molecular structure, which was found to be dimeric [La72]. On the other hand the poly-nuclear organo-gold compounds (number 1,2,3 and 4 in Figure 6.6) vibrate with a molecular mass, which corresponds with the formula weight.
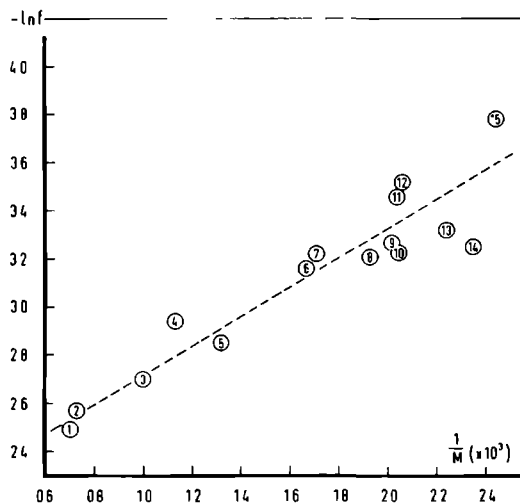
Figure 6.6 Relationship between 1/M (M = molecular weight) and lnf (f = Mossbauer fraction). The numbers refer to the Au^I compounds listed in Table 6.3.
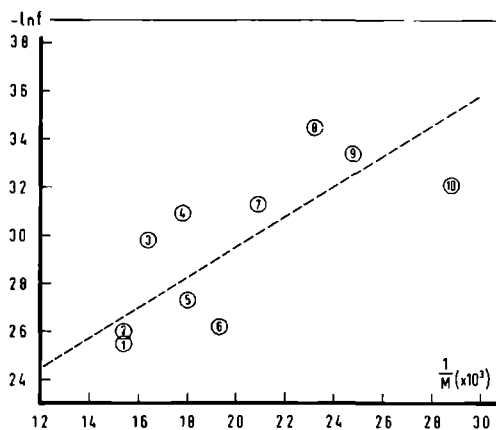
Figure 6.7 Relationship between 1/M (M = molecular weight) and lnf (f = Mossbauer fraction). The numbers refer to the Au^{III} compounds listed in Table 6.4.

6.4 Summary and conclusions

The model, described in section 6.2, has proven to be adequate to explain the temperature dependence of the Mössbauer fraction. Using this model we obtained the separate contributions of the inter- and intramolecular vibrations, which appeared to be comparable in magnitude. Thus the contribution of intramolecular vibrations to $< x^2 >$ cannot be neglected. As mentioned in section 6.2 this contribution is expected to be even larger in compounds with relatively light Mössbauer nuclei, e.g. Fe and Sn.

The established correlation between the Mössbauer fraction and the molecular weight has interesting implications for structural studies by means of the Mössbauer effect. With some care, imposed by the approximate nature of the theory, the mass of the structural units in molecular cyrstals can be determined from the relative absorption intensity of the Mössbauer spectrum.

CHAPTER 7

MAGNETIC SUSCEPTIBILITY AND MÖSSBAUER MEASUREMENTS
ON BIS (MALEONITRILEDITHIOLATO)GOLD(II)

7 1 Introduction

In all compounds, studied in the previous chapters, the gold atom has an even number of spin paired d electrons. Consequently the compounds are diamagnetic. The only paramagnetic compound of gold, isolated in pure form, is the complex $[(n-C_4H_9)_4N]_2 [Au^{II}(mnt)_2]$ (mnt = maleonitriledithiolate) [Wa65]. The crystal structure is unknown though it is expected that $Au(mnt)_2^{2-}$ has a square planar geometry similar to most Au^{III} compounds (see Figure 7.1).
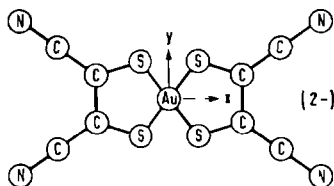
Figure 7.1 $Au^{III}(mnt)_2^{2-}$.

At room temperature the magnetic moment is reported to be 1.85 ± 0.05 μ_B [Wa65]. The electron spin resonance (ESR) spectrum of this complex diluted in the corresponding diamagnetic Ni^{II} complex has been extensively studied [Re70, Sc74,Re75a]. The results show the magnetic hyperfine interaction to be almost isotropic: $A_{xx} = -39.1$, $A_{yy} = -40.5$, $A_{zz} = -41.5$ $(\times 10^{-4}$ $cm^{-1})$. Expressed in Mossbauer units: $A_{av} = \sigma = -40.4$ 10^{-4} $cm^{-1} = 1.94$ mm/sec. The principal components of the quadrupole tensor are $P_{xx} = -18.8$, $P_{yy} = -7.4$ and $P_{zz} = +26.1$ $(\times 10^{-4}$ $cm^{-1})$. The corresponding quadrupole splitting (QS) is equivalent to 3.90 mm/sec and the asymmetry parameter of the electric field gradient (EFG): $\eta = 0.4$.

From the ESR spectra it follows that σ and q_{zz} (z component of the EFG) have opposite sign. A negative sign for σ was derived from theoretical considerations [Re75].

In this chapter we describe the Mössbauer spectra measured with and without the application of an external magnetic field on powders of the pure

undiluted Au^{II} complex. Also presented are the results of magnetic suscepti-
bility measurements between $0.009^{O}K$ and $100^{O}K$, which give evidence for
increasing short range ordering at very low temperatures.

7 2 Experimental

We refer to chapter 2 for details on the Mossbauer measurements.
The Au^{II} complex was synthesized by an electron exchange reaction between Au^{I}
and Au^{III} as described by Waters et al. [Wa71]. Repeated crystallization
from aceton/i-propylalcohol mixtures yielded a highly pure, light green micro-
crystalline product. The substance was carefully powdered to prevent a
preferential orientation of the crystallites.

The magnetic susceptibility between $3^{O}K$ and $100^{O}K$ was measured with a
Foner [Fo59] vibrating sample magnetometer (PAR 155). At lower temperatures
the susceptibility was measured by J.A.A.J. Perenboom at the Physics Labora-
tory at our institute with an AC mutual inductance bridge. For these measure-
ments both the Au^{II} sample and a powdered CMN $(Ce_2Mg_3(NO_3)_{12} \cdot 24H_2O)$ sample
are placed in mutual inductance coils. The coil systems are placed directly
in the mixing chamber of a dilution refrigerator. The CMN sample is used as
a thermometer and is calibrated during the experiment against a NBS standard
reference thermometer SRM 767. The temperatures have an accuracy of ± 2% (at
lowest temperatures ± 1 mK).

7 3 Magnetic susceptibility

In the temperature range from $3^{O}K$ to $100^{O}K$ the magnetic susceptibility
χ follows a Curie law [Vl32] ·

$$\chi = \frac{C}{T} \quad , \tag{7.1}$$

where C is known as the Curie constant (see Figure 7.2). Extension of the
measurements to very low temperatures, however reveals a decrease of the
susceptibility below ~ 26 mK as can be seen in Figure 7.3.

The experimental points were fitted with two theoretical models:
A Exchange coupled pairs.

Anticipating on a dimeric structure the spins are assumed to be coupled
in pairs by the Heisenberg Hamiltonian:
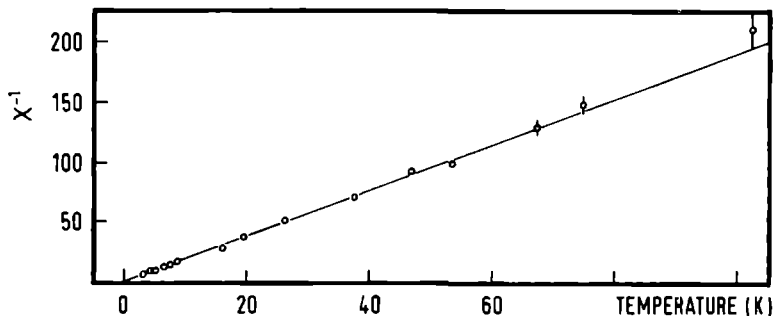
Figure 7.2 High temperature susceptibility of $Au^{II}(mnt)_2^{2-}$.

$$\mathcal{H}_H = J \; \vec{S}_1 . \vec{S}_2 \qquad , \tag{7.2}$$

where $S_1 = S_2 = \frac{1}{2}$ and J is consequently the singlet-triplet separation. The magnetic susceptibility of N pairs of molecules is then given by [V132] :

$$\chi(T) = \frac{2N \; g^2 \beta^2}{kT} \; \frac{1}{3 + \exp(J/kT)} \tag{7.3}$$

However, to obtain a reasonable fit, it was necessary to take into account an axial zero field splitting of the triplet level. Such splitting has been observed by ESR measurements on exchange coupled pairs in analogous complexes of Cu and Ag [Re75b] . It originates from the dipole dipole inter-action and second order spin orbit interaction terms. The spin hamiltonian that describes the energy level splitting is given by:

$$\mathcal{H} = J \; \vec{S}_1 \vec{S}_2 + D \; (S_z^2 - \frac{1}{3} S^2) \qquad , \tag{7.4}$$

where $\vec{S} = \vec{S}_1 + \vec{S}_2$. The resulting energy level scheme is shown in Figure 7.3. For the axial component $\chi_{\parallel}$ of the susceptibility tensor we derive:

$$\chi_{\parallel}(T) = \frac{2N \; g^2\beta^2}{kT} \; \frac{\exp \{-(J + \frac{1}{3} D)/kT\}}{1 + \exp \{-(J - \frac{2}{3} D)/kT\} + 2 \exp \{-(J + \frac{1}{3} D)/kT\}}$$

$$\tag{7.5}$$

and for the perpendicular component:

$$\chi_\perp (T) = - \chi_\parallel (T) \cdot \frac{kT}{D} \{1 - \exp(D/kT)\} \qquad (7.6)$$
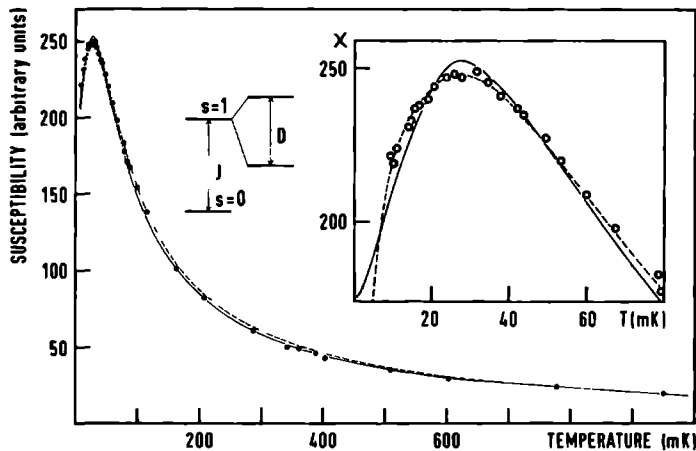
Figure 7.3   Susceptibility χ of $Au^{II}(mmt)_2^{2-}$. Circles: experimental
points; solid line: linear chain theory; dashed line:
exchange coupled pair theory. Also shown is the energy
level scheme for the exchange coupled pairs.

The susceptibility of a polycrystalline sample is then given by:

$$\chi (T) = \frac{1}{3} \chi_\parallel (T) + \frac{2}{3} \chi_\perp (T) \qquad . \qquad (7.7)$$

The parameters J and D and a vertical scale factor were adjusted and the best
fit was obtained for J/k = 67.9 mK and D/k = 96.5 mK.
B: Linear chain model with nearest neighbour Heisenberg exchange interaction.
The theoretical curve [Bo64,Ba64] is fitted by adjusting the exchange
constant J and a vertical scale factor. The best fit is obtained for J/k =
22.0 mK.

    The vertical scale offset, which is inherent to the measuring method, was

104

determined from extrapolation of χ to high temperatures, and this value was used in both cases.

As Figure 7.3 shows, the experimental data are best described by an exchange coupled pair model in particular at low temperatures. However, the pair model contains two adjustable parameters J and D, whereas the chain model contains only one parameter J (except for a scale factor in both models) Therefore the susceptibility data do not allow a definite conclusion concerning the magnetic structure.

7.4 Mossbauer spectra

a. No external field

The Mössbauer spectrum measured on a polycrystalline sample at 1.6^OK is given in Figure 7.4. Practically the same spectrum is observed at 4.2^OK. The
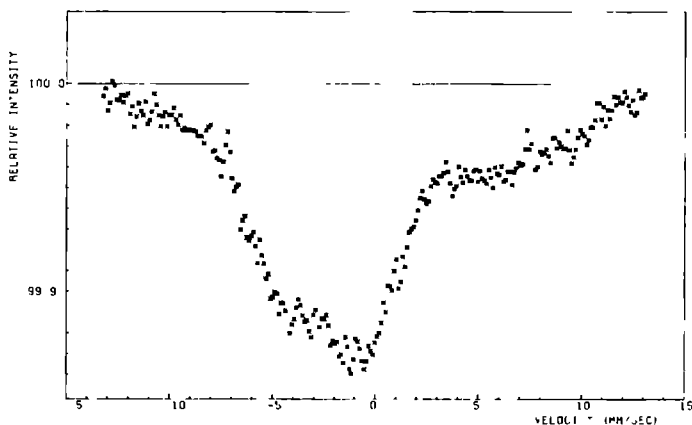
Figure 7.4   Mössbauer absorption spectrum of polycrystalline
[$(n-C_4H_9)_4N$] $_2$ [$Au(mnt)_2$] at 1.6^OK.

width of the spectrum suggests a magnetic interaction. However, a magnetic ordering at this temperature can be excluded on grounds of the magnetic susceptibility measurements described in the preceding section.

A qualitative explanation of the peculiar asymmetric shape of the

spectrum can be given if we assume slow electron spin relaxation. Slow spin relaxation spectra have been observed on a number of low spin iron(III) complexes and the theory has been discussed by Lang and Oosterhuis [La69]. When the electron spin relaxation time is long compared with one period of the nuclear Larmor precession, the magnetic interaction between nuclear and electron spin is similar to that in the free ion [Af63]. Neglecting the small anisotropy in the magnetic hyperfine coupling and in the absence of a quadrupole interaction the energy levels are given by the Hamiltonian:

$$\mathcal{H}_M = a \; \vec{I}.\vec{S} \quad . \tag{7.8}$$

The energy level scheme and the resulting Mössbauer spectrum calculated with $a = -1.94$ mm/sec as derived from the ESR spectra is given in Figure 7.5. A positive sign of a would result in a spectrum mirrored with respect to zero velocity. From this it follows that the sign of a can be unambiguously determined, which is a unique feature of these slow relaxation spectra.

When a quadrupole interaction is also present the Hamiltonian for the nuclear energy levels is:

$$\mathcal{H} = a \; \vec{I}.\vec{S} + \vec{I}.\overline{\overline{P}}.\vec{I} \quad . \tag{7.9}$$

For the sake of simplicity the energy levels were calculated with an axially symmetric electric field gradient tensor with $P_{zz} = 1.3$ mm/sec, and $a = -1.94$ mm/sec. The result is given in Figure 7.5 together with the intensities of the transitions. The spectrum is rather complicated, but the pronounced asymmetry is retained. For an EFG with $\eta = 0.4$ almost the same intensities and positions are found. Convolution of this "stick"-spectrum with Lorentzian shaped absorption lines of width $\Gamma = 2$ mm/sec results in a calculated Mössbauer spectrum as given in Figure 7.6b. Compared with the measured spectrum, the calculated spectrum has a larger overall width and rather discrete peaks. Because the spectra at 1.6°K and at 4.2°K are the same, the less pronounced features in the measured spectrum cannot be attributed to an intermediate relaxation rate.

If we assume, as we have done to explain the susceptibility data, that the gold atoms occur in exchange coupled pairs, the spectrum (shown in Figure 7.6) is a super position of a quadrupole doublet resulting from the singlet (S = 0) state and 24 transitions belonging to the triplet (S = 1) state. For
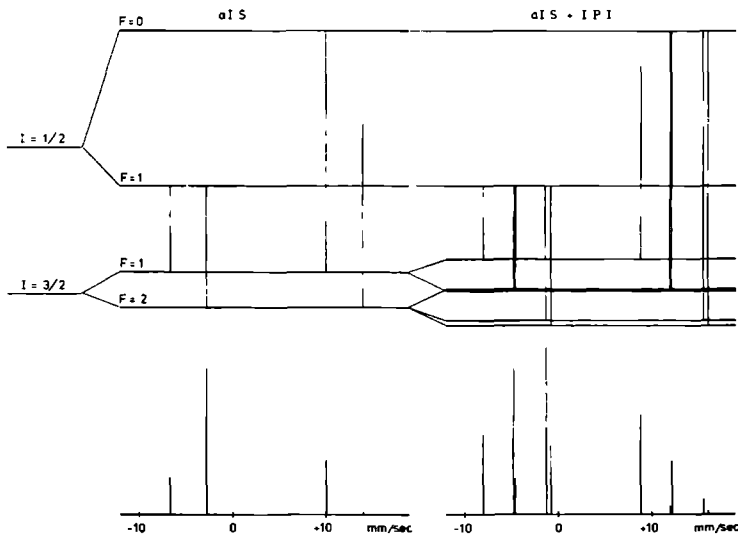
Figure 7.5 Energy levels ^{197}Au for combined magnetic hyperfine and electric quadrupole interaction in the case of slow relaxation, $\vec{F} = \vec{I} + \vec{S}$. Energies and intensities are calculated for a powder absorber using $a(I = 3/2) = -1.94$ mm/sec, $a(I = 1/2) = -16.8$ mm/sec and $P_{zz} = -2P_{xx} = -2P_{yy} = 1.3$ mm/sec.

the calculation of the spectrum the magnetic hyperfine coupling constant was taken equal to half the value of the monomeric case [Re60]. The agreement with the experimental spectrum is significantly improved. However, because the magnetic susceptibility data could be fitted with an exchange coupled pair model, only if zero field splitting was taken into account, we have also calculated the Mössbauer spectrum for a Hamiltonian including this zero field splitting:

$$\mathcal{H} = a \; \vec{I}.\vec{S} + \vec{I}.\bar{\bar{P}}.\vec{I} + \vec{S}.\bar{\bar{D}}.\vec{S} \quad , \tag{7.10}$$

$\bar{\bar{D}}$ was taken to be axially symmetric with the numerical value of $D_{zz} = 21.5$ mm/sec as derived from the susceptibility data. The agreement with the experimental spectrum is worse than for $D = 0$ (compare Figures 7.6 and 7.7). Rotation of the principal axes of $\bar{\bar{D}}$ with respect to $\bar{\bar{P}}$ gives no improvement
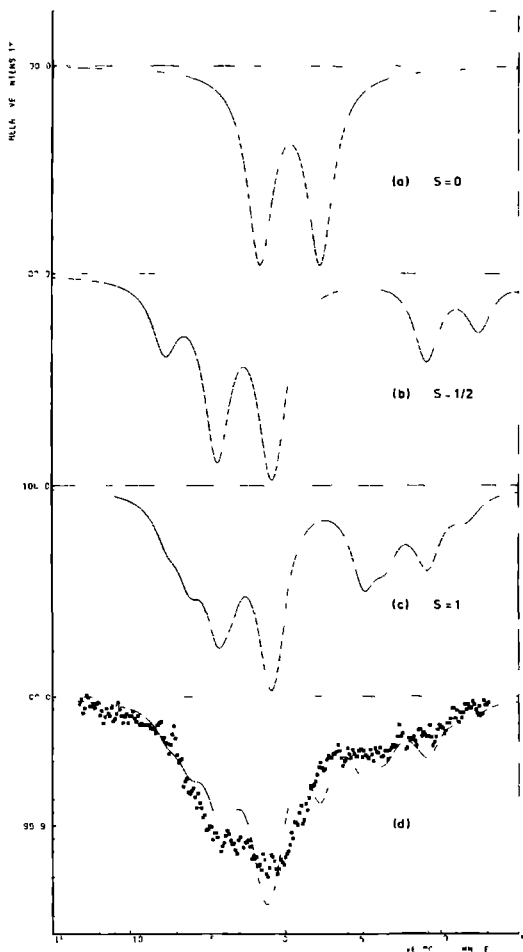
Figure 7.6   Slow relaxation Mössbauer spectra of a powder absorber, resulting
from an isotropic magnetic hyperfine interaction combined with an
axially symmetric electric quadrupole interaction, as given by Eq.
7.9, for different values of S. The parameters are:

(a) $S = 0$, $P_{zz} = 1.3$ mm/sec

(b) $S = 1/2$, $P_{zz} = 1.3$ mm/sec, $a(I = 3/2) = -1.94$ mm/sec,
$a(I = 1/2) = -16.8$ mm/sec

(c) $S = 1$, $P_{zz} = 1.3$ mm/sec, $a(I = 3/2) = -0.97$ mm/sec,
$a(I = 1/2) = -4.2$ mm/sec

(d) Measured spectrum. The drawn line is the sum of curves (a) and
(c) with an intensity ratio of $1 : 3$.

and reduces the asymmetry in the calculated spectrum. Thus it appears that the large zero field splitting of the exchange coupled electron spin pairs is not consistent with the Mossbauer spectrum and the obtained agreement with the susceptibility is fortuitous.
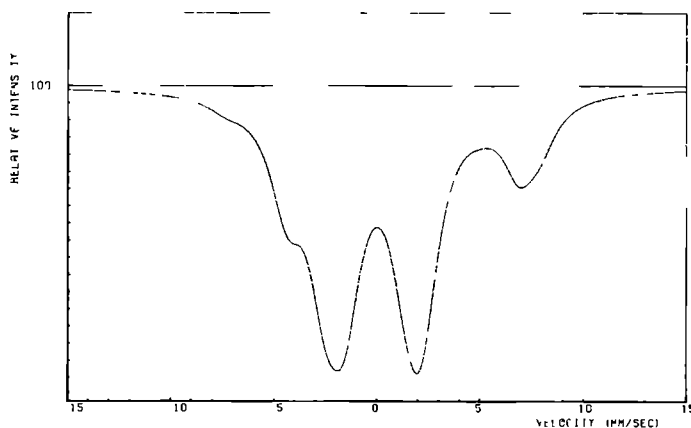
Figure 7.7   Slow relaxation Mössbauer spectrum of a powder absorber, resulting from the Hamiltonian, given by Eq. 7.10, in case of exchange coupled pairs and axial symmetry. The parameters are:

$a(I = 3/2) = -0.97$ mm/sec, $a(I = 1/2) = -4.2$ mm/sec, $P_{zz} = 1.3$ mm/sec, $D_{zz} = 21.5$ mm/sec.

Comparing the Mossbauer spectra for $S = \frac{1}{2}$ and $S = 1$ it can be expected that if a large number of electrons is coupled (as a linear chain) this results in a further smoothing of the discrete peaks in agreement with the experimental spectrum. The Mossbauer spectrum alone does not allow any meaningful numerical analysis in terms of larger spin multiplets as too many parameters are involved. The following definite conclusions can be drawn however:

1. There is evidence for slow spin relaxation
2. The magnetic hyperfine coupling constant a is negative
3. Electron spin coupling is necessary to explain the spectrum.

The negative sign of a shows that the dominant mechanism producing spin density at the gold nucleus is spin polarization [Mc67], as is also the case for the

corresponding Cu^{II} and Ag^{II} compounds [Ma64,We68,Ki71] .

b. Application of an external magnetic field

As has been pointed out by Lang and Oosterhuis [La69] , application of an external field results in a decoupling of electronic and nuclear spin and the Hamiltonian describing the hyperfine interaction becomes:

$$\mathcal{H} = a \; I_z S_z + \vec{I}.\bar{\bar{P}}.\vec{I} \quad , \tag{7.11}$$

where the z axis is parallel to the external field: H_{ext}.
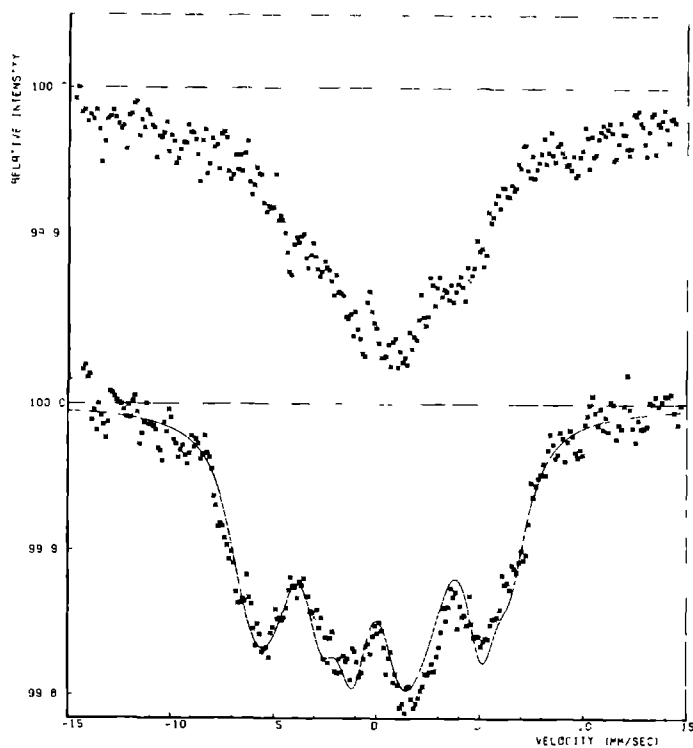
Figure 7.8   Mössbauer spectra of polycrystalline [(n-C_4H_9)$_4$N]$_2$ [Au(mnt)$_2$] at 1.4°K in external magnetic fields of 1T (top) and 5T (bottom). The drawn line is a least squares fit, discussed in the text.

The Mossbauer spectra of $Au^{II}(mnt)_2^{2-}$ in external fields of 1T and 5T are given in Figure 7.8. In an applied field of 5T at $1.4^{O}K$ the electron spin is almost completely polarized and the Hamiltonian of Eq. 7.11 can be written as·

$$\mathcal{H} = \vec{H}_{eff}.\vec{I} + \vec{I}.\bar{\bar{P}}.\vec{I} \quad , \tag{7.12}$$

where $\vec{H}_{eff} = \vec{H}_{ext} + \vec{H}_{int}$ and $\vec{H}_{int}$ is the internal field of Au^{II} corresponding with $S_z = \frac{1}{2}$. Because the measurements were carried out on a powder, one has to average over all possible directions of $\vec{H}_{eff}$ with respect to the principal axis of the quadrupole tensor $\bar{\bar{P}}$. The spectrum, calculated as explained in section 3.2b, is sensitive for the value of the IS, the QS and H_{eff} and insensitive fot the value of the assymetry parameter η and the sign of the QS. The calculation was carried out with the aid of a computer programme, which was incorporated in a least-squares-fitting procedure. A good fit of the experimental spectrum was obtained with QS, IS and H_{eff} as free parameters, together with a vertical scale factor and a baseline constant, η was set equal to zero. The result is shown in Figure 7.8 and the parameters are summarized in Table 7.1. They agree very well with the parameters obtained by ESR measurements on magnetically diluted single crystals.

Table 7.1   Results of Mossbauer experiments. The IS is given with
respect to the source of ^{197}Au in Pt.

Compound	IS (mm/sec)	QS (mm/sec)	H_{int} (kOe)
$[(n-C_4H_9)_4N]_2[Au^{II}(mnt)_2]$	0 12 ' 0 05	3 68 ' 0 10	815 '
$[(n-C_4H_9)_4N][Au^{III}(mnt)_2]$	2 92 ' 0 01	2 33 ' 0 01	

' H_{int} corresponds with a groundstate hyperfine coupling
constant a - 1 93 + 0 02 mm/sec

Also given in Table 7.1 are the parameters of the corresponding Au^{III} compound. In going from $Au^{III}(mnt)_2^-$ to $Au^{II}(mnt)_2^{2-}$ an increase in the QS of 1.7 mm/sec is observed. This is best understood if the unpaired electron

occupies the anti-bonding $5d_{xy}$ molecular orbital (b_{2g} in D_{4h} symmetry, see Figure 5.19). One $5d_{xy}$ electron gives a contribution to the QS of 7.8 mm/sec, as follows from Eq. 5.9 with the data in Table 3.1 and $< r^{-3} >_{5d} = 12.3\ a_o^{-3}$. From this one may infer that the orbital coefficient in the relevant molecular orbital is 0.4. It should be kept in mind that this number is based on σ-bonding only and neglects the importance of π-back-donation, for which strong evidence was obtained in chapter 5. The observed decrease of the IS in going from Au^{III} to Au^{II} agrees also with the MO picture, where the unpaired electron moves in a b_{2g} orbital. As can be seen in Eq. 5.6 an increase of the 5d population causes a decrease of $|\Psi(0)|^2$ and consequently a decrease of the IS.

7 5 Summary and conclusions

From the results of our magnetic susceptibility and zero field Mossbauer measurements, taken together, it must be concluded that the magnetic structure of $[\ (n-C_4H_9)_4N\ ]_2\ [\ Au(mnt)_2\ ]$ is best described by an Heisenberg linear chain with an exchange constant $J/k = 22.0$ mK. Furthermore we found experimental evidence from the asymmetry of the zero field spectrum for a negative sign of the magnetic hyperfine coupling and a positive sign of the electric field gradient along the symmetry axis in agreement with previous proposals on theoretical grounds.

The effects of electron spin relaxation and spin-spin coupling were eliminated by application of a large external magnetic field at low temperatures. The spin hamiltonian parameters, obtained from a least squares fit of the spectrum, agree very well with the parameters obtained by ESR measurements on magnetically diluted single crystals.

We did not yet succeed in growing single crystals suitable for X-ray investigation. But recently Plumlee et al. [P175] reported the crystallographic structure of the copper analogon, which consists of linear chains of $Cu(mnt)_2^{2-}$ ions separated by the bulky $(C_4H_9)_4N^+$ ions. For the interpretation of their ESR measurements the authors proposed an Heisenberg chain with $J = 11.0$ mK. The close similarity with the results of our measurements on the gold(II) compound makes it worthwhile to look for isomorphism between the copper and gold compounds, for which a comparison of the X-ray powder diffraction patterns may be sufficient.

CHAPTER 8

MÖSSBAUER SPECTROSCOPY OF SMALL GOLD PARTICLES

8 1 Introduction

Recently the properties of small particles have attracted much interest. New phenomena can be expected when the dimensions of the systems become comparable with the characteristic wavelengths of particular physical properties. One of the properties where changes can be expected is the phonon spectrum, and one of the experimental methods, which give information on the phonon frequency distribution is the Mossbauer Effect (ME). We recall from section 3.3 that the intensity of Mossbauer absorption is proportional to

$$f_a(T) = \exp\left[-\frac{4\pi^2 <x^2>_T}{\lambda^2}\right] \quad , \tag{8 1}$$

where $f_a(T)$ is the probability for recoilless absorption (the Mossbauer fraction) at temperature T, $<x^2>_T$ the mean square vibrational amplitude of the absorbing nucleus at temperature T and λ the wavelength of the absorbed radiation.

A sizable number of papers has reported on a study of the phonon spectrum of small particles with the Mossbauer Effect, but until now no consistent picture emerges. Marshall and Wilenzick [Ma66] measured the ME of gold particles with an average diameter of 60 Å and 200 Å. For the 60 Å particles an increase in $f_a(T)$ was found compared with bulk gold, which these authors attributed to a low frequency cut-off in the phonon spectrum. It is noteworthy that at that time no accurate experimental measurement of $f_a(T)$ in bulk gold had been made. Roth and Horl [Ro67] measured the ME in 30 Å tungsten particles suspended in frozen organic solvents and found at 78°K a decrease in f_a compared with the bulk value. Susdalev, Gen, Goldanskii and Makarov [Su66] studied tin particles in paraffin with diameters between 1550 Å and 250 Å and found f_a decreasing with decreasing particle size. Bogomolov and Klushin [Bo73] measured the ME of tin in porous glass with a pore diameter of 70 Å. At temperatures below 100°K f_a was found to be larger than in bulk tin, but at higher temperatures f_a was smaller than the bulk values at corresponding temperatures. However the values of $f_a(T)$ for bulk tin, given by Bogomolov and

113

Klushin, differ considerably from the very accurate measurements by Hohen-emser [Ho65], which makes the reliability of their data questionable. Akselrod, Pasternak and Bukshpan [Ak75] measured the temperature dependence of the ME of small (45 Å) tin particles embedded in amorphous SnO. The temperature gradient of $f_a(T)$ was found to be slightly larger than in bulk tin. These authors apparently have not corrected for any saturation effect in the measured absorption intensity presumably because the absorbers used were very thin. It is important to note, however, that an absorber thickness of 1 mg/cm^2 of natural tin at 77°K already leads to a lineshape, which when fitted with a Lorentzian gives an absorption area 7% smaller than without saturation (see section 4.2). Neglect of such effects can easily lead to apparent changes in the Debye temperature of the same order of magnitude as found by Akselrod et al. [Ak75]. Thus the conflicting results of the ME experiments are partly due to unreliable data, but sample preparation may also have effects on the results [Sc70]. Furthermore the role of the medium, supporting the particles, has not been discussed, although considerable differences in Mossbauer fraction were recently found for thin films of tin on different substrates [Ep74].

In this chapter we report a ME study of microcrystals of gold embedded in gelatin. This matrix is well suited to prepare high concentrations of particles with a narrow size distribution. In section 8.2 we give a survey of various models, which can be used to describe the effect of particle size on the phonon spectrum and present the results of a number of calculations. Much effort has been put in the preparation of well defined samples. These are described in section 8.3. The results are discussed in section 8.4 where we conclude that the matrix supporting the particles has to be taken into account.

8 2 Mossbauer spectroscopy and the phonon spectrum of small particles

In the harmonic approximation the probability for recoilless absorption is given by Eq. 8.1. For a mono-atomic lattice with a distribution $g(\omega)$ for the phonon frequencies one gets inserting Eq. 3.43 in Eq. 8.1

$$f_a(T) = \exp\left\{-\frac{\hbar^2}{2m\lambda^2} \cdot \frac{1}{3N} \int_0^\infty \frac{g(\omega)}{\omega} \left(\frac{2}{\exp(\frac{\hbar\omega}{kT})-1} + 1\right) d\omega\right\} \quad , \qquad (8.2)$$

where m is the atomic mass, k the Boltzmann constant, $\hbar = h/2\pi$ Planck's constant and N is the number of atoms in the lattice.

In the Debye continuum theory $g(\omega)$ of a cube with edge L is given by [Mo50]:

$$g(\omega) = \frac{3L^3}{\pi c^3} \omega^2 + \frac{9L^2}{2c^2} \omega + \frac{3L}{8c} \quad . \tag{8.3}$$

Here c is an average sound velocity. The first term in the right hand side of Eq. 8.3 represents the contribution of the bulk phonons, the second term the surface modes and the last term the edge modes. In bulk the first term on the right hand side of Eq. 8.3 dominates and is the only one retained. In this approximation there is an upper limit ω_m for the phonon frequency given by:

$$\omega_m = \frac{3N\pi c^3}{L^3} \quad , \tag{8.4}$$

because of the normalization condition:

$$\int_0^\infty g(\omega) d\omega = 3N \quad , \tag{8.5}$$

where N is the number of atoms in the cube.
The maximum phonon frequency is usually expressed in an equivalent temperature the Debye temperature Θ_D:

$$\Theta_D = \frac{\hbar \omega_m}{k} \quad . \tag{8.6}$$

Expressing L in Θ_D with help of Eqs. 8.4 and 8.6, $g(\omega)$ is given by:

$$g(\omega) = \frac{9N\hbar^3}{k^3 \Theta_D^3} \omega^2 \quad (0 < \hbar\omega < k\Theta_D) \quad . \tag{8.7}$$

Using this expression for $g(\omega)$ in Eq. 8.2 one obtains:

$$f_a(T) = \exp \left\{ - \frac{\hbar^2}{2m\lambda^2} \cdot \frac{3}{2k\Theta_D} \left(1 + \frac{4T^2}{\Theta_D^2} \int_0^{\Theta_D/T} \frac{x\,dx}{e^x - 1} \right) \right\} \quad , \tag{8.8}$$

which is the same expression as given in Eq. 3.48. If $g(\omega)$ deviates from the Debye spectrum, as is generally the case, Θ_D is temperature dependent. In that case Θ_D also differs from Θ_D^C determined from specific heat measurements, because both methods measure different moments of $g(\omega)$. For bulk gold, however, the temperature dependence of Θ_D as well as the difference between Θ_D and Θ_D^C is small [Er71]. In fact the temperature dependence of the Mossbauer fraction is very well reproduced by Eq. 8.8 with $\Theta_D = 168^\circ$K.

In case of small particles an obvious change in the phonon spectrum $g(\omega)$ compared with bulk material will be a low frequency cut-off, ω_L. The longest possible wavelength is of the order of the particle dimension L. If the boundaries of the particle are assumed to be at rest, ω_L is given by

$$\omega_L = \frac{\tau c}{L} \quad . \tag{8.9}$$

The normalization condition Eq. 8.5 now becomes

$$\int_{\omega_L}^{\infty} g(\omega)\,d\omega = 3N \quad , \tag{8.10}$$

resulting in a high frequency cut-off, ω_H, given by.

$$\omega_H^3 = \omega_m^3 + \omega_L^3 \quad , \tag{8.11}$$

where ω_m is given by Eq. 8.4. Expressing ω_H and ω_L in the equivalent temperatures Θ_H and Θ_L the phonon frequency distribution is given by

$$g(\omega) = \frac{9N\hbar^3}{k^3} \left(\frac{1}{\Theta_H^3 - \Theta_L^3} \right) \omega^2 \qquad (k\Theta_L \leqslant \hbar\omega \leqslant k\Theta_H) \quad . \tag{8.12}$$

With $g(\omega)$ given by Eq. 8.12 the Mossbauer fraction is given by.

$$f_a(T) = \exp\left\{ -\frac{h^2}{2m\lambda^2} \cdot \frac{3(\theta_H^2 - \theta_L^2)}{2k(\theta_H^3 - \theta_L^3)} \left[1 + \frac{4T^2}{\theta_H^2 - \theta_L^2} \int_{\theta_L/T}^{\theta_H/T} \frac{x\,dx}{e^x - 1} \right] \right\} \quad (8.13)$$

In general $\theta_L \ll \theta_D$ and $f_a(T)$ is, without loss of accuracy, given by Eq. 8.8 if we replace the lower limit in the integral by θ_L/T. Using Eq. 8.13 $f_a(T)$ was calculated for a number of values of θ_L. The results are given in Figure 8.1. The most conspicuous changes are an increase of $f_a(T)$ with increasing θ_L
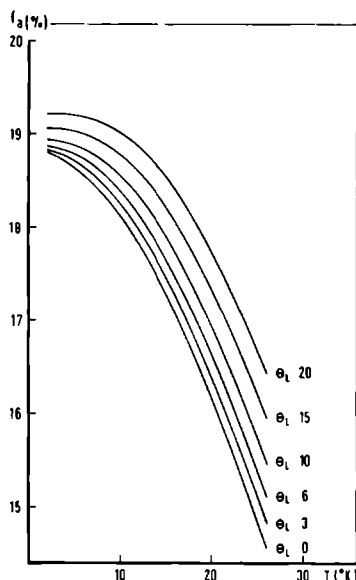
Figure 8.1 Temperature dependence of the Mossbauer fraction f_a according to the Debye theory (Eq. 8.13) with application of different low frequency cut-offs on the phonon spectrum, expressed in equivalent temperatures θ_L. θ_H was taken to be $170^\circ K$.

and a smaller temperature gradient at low temperatures with increasing θ_L. However, when L is small it is no longer allowed to neglect the contribution of surface and edge modes to $g(\omega)$, as we have done until now, and we show that this has important consequences for $f_a(T)$.

Substituting Eq. 8.3 into Eq. 8.2 one obtains

$$f_a(T) = \exp\left\{-\frac{h^2}{2m\lambda^2} \cdot \frac{1}{3N}\left(A + B(T) + C(T) + D(T)\right)\right\} \quad , \tag{8.14}$$

where

$$A = \frac{3\pi}{4k\Theta_L^3}(\Theta_H^2 - \Theta_L^2) + \frac{9\pi}{4k\Theta_L^2}(\Theta_H - \Theta_L) + \frac{9}{4k\Theta_L}\ln\left(\frac{\Theta_H}{\Theta_L}\right) \quad , \tag{8.14a}$$

$$B(T) = \frac{3\pi}{\Theta_L^3}T^2 \int_{\Theta_L/T}^{\Theta_H/T} \frac{x\ dx}{e^x - 1} \quad , \tag{8.14b}$$

$$C(T) = \frac{9\pi}{2\Theta_L^2}T \int_{\Theta_L/T}^{\Theta_H/T} \frac{dx}{e^x - 1} \quad , \tag{8.14c}$$

$$D(T) = \frac{9}{2\Theta_L} \int_{\Theta_L/T}^{\Theta_H/T} \frac{\frac{1}{x}\ dx}{e^x - 1} \quad , \tag{8.14d}$$

and the normalization condition gives

$$3N = \int_{\omega_L}^{\omega_H} g(\omega)\,d\omega = \frac{\pi}{2\Theta_L^3}(\Theta_H^3 - \Theta_L^3) + \frac{9\pi}{8\Theta_L^2}(\Theta_H^2 - \Theta_L^2) + \frac{9}{4\Theta_L}(\Theta_H - \Theta_L) \quad . \tag{8.14e}$$

In Figure 8.2 we give $f_a(T)$ calculated with Eq. 8.14 for various values of Θ_L. It is seen that the inclusion of surface and edge modes in the calculation of $f_a(T)$ leads to a decrease of the Mössbauer fraction at low temperatures with increasing Θ_L, contrary to the results given in Figure 8.1.

In the foregoing we have used an average sound velocity c and therefore through Eqs. 8.4 and 8.9 average cut-off frequencies. However different modes may have different velocities. For instance Love [Lo44] has calculated the maximum wavelength λ_m in a free elastic sphere of diameter d for rotary and radial vibrations and found d/λ_m = 1.8346 and 0.8160 respectively. For
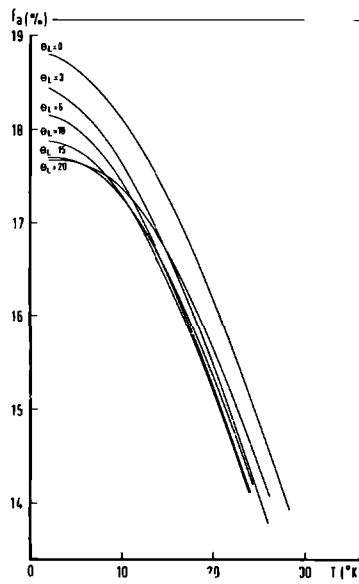
Figure 8.2 Temperature dependence of the Mössbauer
fraction f_a according to the Debye theory
including surface and edge modes (Eq. 8.14)
for different values of the low frequency
cut-off temperature Θ_L. Θ_L determines also
the relative contribution of the surface
and edge modes. Θ_H was taken to be $170^\circ K$.

Rayleigh surface modes one finds $C_R = 0.9149\ C_T$ where C_T is the velocity of bulk transverse waves [Lo44]. Maradudin et al. [Ma72] calculated for edge modes $C_E = 0.9013\ C_T$. Further reductions in the velocities of sound waves can be expected as a result of a weakening of binding forces for the surface atoms. Consequently the low frequency cut-off should be different for bulk, surface and edge modes. In comparing calculated and measured values of $f_a(T)$ a further limitation lies in the assumed cubic shape of the particles.

A more serious objection against using the formulas derived above is the fact that we have calculated an average vibrational amplitude which is taken the same for all atoms. In fact we have assumed that every vibrational mode contributes to the amplitude of every atom. Suzdalev et al. [Su66] and later Akselrod et al. [Ak75] have circumvented this problem by assigning different Mössbauer fractions f_a^B and f_a^S to bulk and surface atoms, respectively. In that

119

case:

$$f_a^{total}(T) = \alpha\; f_a^B(T) + (1 - \alpha)\; f_a^S(T) \quad , \tag{8.15}$$

where α is the fraction of bulk atoms. For gold this approach is supported by LEED measurements of Kostelitz and Domange [Ko73] . These authors find for the surface atoms an effective Debye temperature of $0_D^S = 83^\circ K$, which means that at $T \ll 0_D$ the mean squared vibrational amplitude of these surface atoms is two times that of bulk atoms. In Figure 8.3 we give $f_a^{total}(T)$ using $0_D^B = 170^\circ K$ and $0_D^S = 80^\circ K$ for various values of α. Obviously the Mossbauer fraction is strongly dependent on α.
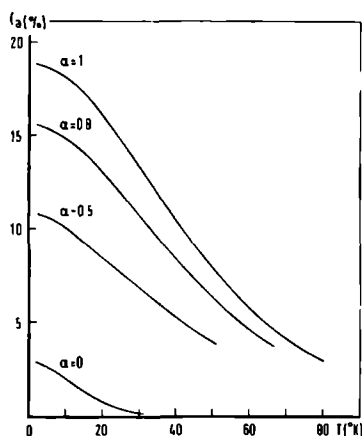
Figure 8.3 *Temperature dependence of the total Mössbauer*
fraction f_α, which is the sum of individual
contributions of bulk and surface atoms (Eq. 8.15).
$f_\alpha^B(T)$ and $f_\alpha^S(T)$ have been calculated according to
the Debye theory (Eq. 8.8) with $0_D^B = 80^\circ K$ and $\Theta_D^S =
$170^\circ K$. The fraction of bulk atoms is given by α.

8.3 Experimental details and results

a Sample preparations

The chemistry of hydrosols (colloidal dispersions of solid in water) has

been studied extensively [Kr52]. A hydrosol of gold can be prepared by striking an electric arc between gold wires under water or alternatively by reduction of an aquaous solution of auric chloride $AuCl_4^-$. The second method allows a better control of particle size. For this method the competing processes of nucleation and epitaxial growth have been investigated by Turkevich et al. [Tu51]. These authors found that depending on the nature of the reducing agent and the relative abundance of auric chloride either nucleation or growth is favoured.

Coagulation of the gold particles is prevented by a layer of chloride ions on the surface of the particles [Pa35]. The particles then behave like large negative ions and can only exist in very dilute solution. Stabilizers, like gelatin, replace the charged layer on the surface. After such protection of the sol the water can be removed resulting in a high concentration of gold particles. The samples studied in this work have been prepared using as reducing agent either a saturated solution of phosphorus in ether or a sodium citrate solution. To prevent the presence of trace impurities, which cause uncontrolled nucleation, a 1 liter glass vessel was cleaned first with aqua regia, then with a detergent and finally rinsed with distilled water. An 800 ml solution of auric chloride acid containing about 30 mg gold was made neutral with potassium carbonate and under vigorous stirring the reducing agent was added. Dropwise addition of 5 ml of the phosphorus solution over half an hour at room temperature yields an average particle diameter of about 60 Å. Rapid addition favours nucleation above growth and the resulting particles have a diameter of about 30 Å. To remove the excess phosphorus the solution is boiled for 3 hours after addition of 0.5 g gelatin. Particles with an average diameter of 150 Å were prepared with 100 ml of a 1% sodium citrate solution as reducing agent. The nuclei formed at room temperature grow to their final size of approximately 150 Å when heated for 2 hours at 80°C. After this the gelatin is added.

In order to remove impurities, especially chloride ions, which may still be bound to the surface of the particles, two techniques were used 1) dialysis with ½" cellulose tubes and 2) ion exchange with a mixed bed ion exchange resin. The latter method results in a complete removal of all ionic substances. Both techniques were carried out after the gelatin was added and did not affect the particle size distribution as measured with an electron microscope.

The solutions were dehydrated in a rotating film evaporator and put in lucite pill boxes. The samples contained approximately 8 weight % of gold.

Table 8.1

Sample	Reducing agent	Purification	Gold content (mg/cm^2)	Average diameter (Å)	Effective [1] average diameter (Å)	Coherence length (Å)	Bulk [2] fraction α (%)	Isomer [3] shift (mm/sec)	f_a (4.2°K) (%)
1	phosphorus	none	22.0 ± 0.7	52	62	43 ± 4	72	0.042 ± 0.005	17.1 ± 1.0
2	Na-citrate	none	26.3 ± 0.8	168	176	80 ± 3	91	0.065 ± 0.006	18.2 ± 1.1
3 [4]	phosphorus	dialysis + ion exchange	27.2 ± 0.8 10.5 ± 0.3	31	42	–	55	0.100 + 0.008	19.3 ± 0.9 20.6 ± 1.1
4	phosphorus	dialysis + ion exchange	6.5 ± 0.2	50	59	–	–	0.073 ± 0.008	19.4 ± 1.0
5	phosphorus	dialysis	28.5 ± 0.9	31	42	–	–	0.132 ± 0.008	17.7 ± 0.9
6	phosphorus	none	11.7 ± 0.4	31	42	–	–	0.131 ± 0.008	18.5 ± 0.9
7	phosphorus	ion exchange	20.4 ± 0.6	31	42	–	–	0.061 ± 0.008	20.4 ± 0.9
8	phosphorus	none	–	55	–	–	–	0.10 ± 0.02	–
9	phosphorus	none	–	55	–	–	–	0.20 ± 0.07	–

[1] weighted with the third power of the diameter.

[2] 1-α is the relative number of atoms in surface layer of thickness 2.5 Å averaged over size distribution.

[3] with respect to bulk gold. The values given are based on all measurements carried out at 4.2°K for each sample In case of sample 1 the IS of the main line is given.

[4] two absorbers were made from the same sample.

After all measurements were carried out the gold content of the samples was determined by atomic absorption. In Table 8.1 the preparation and purification treatments and the gold content of the samples are given.

b Particle size determination

A probe of each sample was examined with a Philips EM201 electron microscope. Figure 8.4 shows an electron micrograph of sample 4 deposited on

0.1 μ
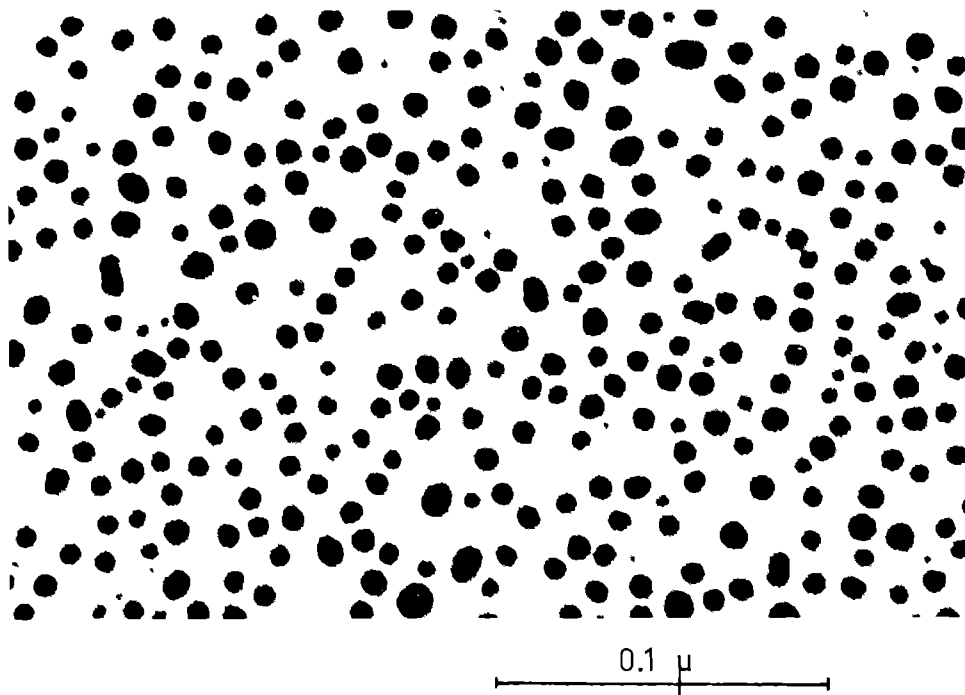
Figure 8.4   Electron micrograph of the gold particles in sample 4. Average particle diameter is 45 Å.

carbon coated formvar. The size distribution of each sample was determined by measuring the diameter of some 500 particles on similar micrographs. For samples 1, 2 and 3 histograms of the particle size distributions are given in Figure 8.5. The measured Mossbauer absorption is essentially a sum of the contributions of all individual atoms, therefore an effective average particle

123
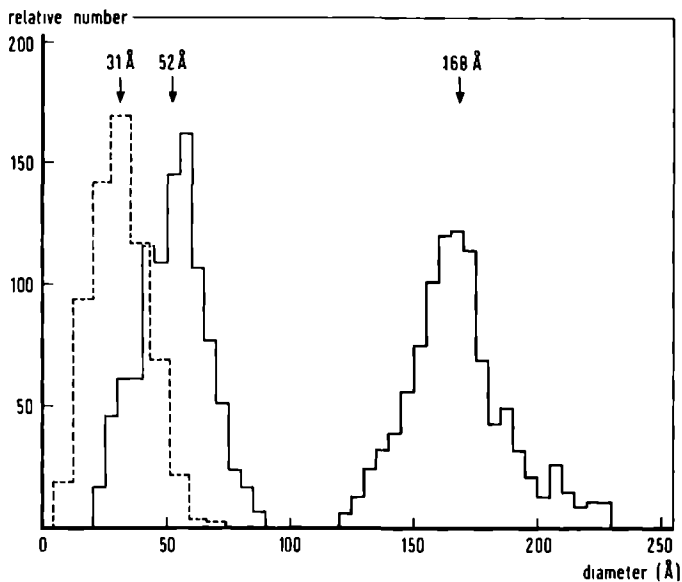
Figure 8.5   Size distribution of sample 3 (31 Å), sample 1 (52 Å) and
sample 2 (168 Å).
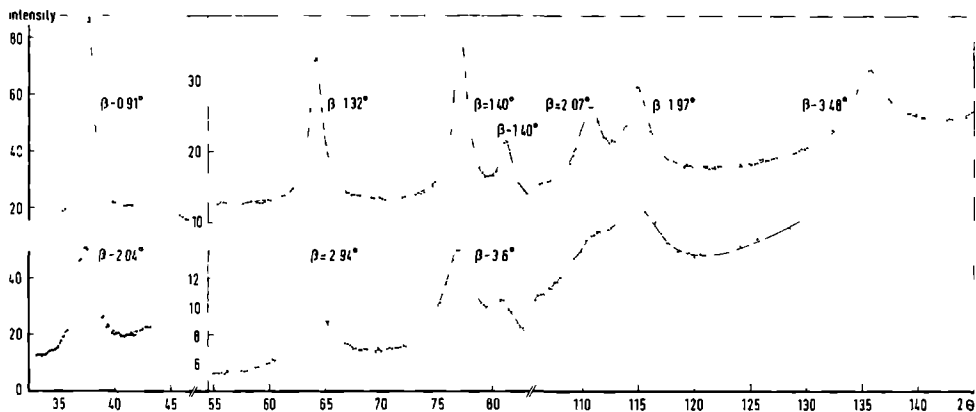
Figure 8.6   X-ray diffraction pattern of sample 2 (168 Å, upper curve) and
sample 1 (52 Å, lower curve). Values of β have been corrected
for instrumental and K_α-doublet broadening.

size should be used, obtained by weighting the number of particles of given diameter with the corresponding particle volume. Actual and volume weighted average diameters are given in Table 8.1.

An often used method to determine the particle size is measurement of the width β of the Bragg-diffraction peaks. The coherence length D_c for Bragg-diffraction is given by [K159]

$$D_c = K \lambda / \beta \cos\theta, \qquad\qquad (8.16)$$

where λ is the X-ray wavelength and θ the diffraction angle. $K = 1.0747$ for spherical particles, when β is the full width at half maximum in units of 2θ. The Bragg peaks as measured on sample 1 and 2 are shown in Figure 8.6. The indicated linewidth has been corrected for instrumental and K_α doublet broadening. The results, given in Table 8.1, differ considerably from the particle size measured with the electron microscope. There are two possible explanations for this: a gradient in the lattice constant, as found from molecular dynamic calculations carried out by Burton [Bu70], or a multiply twinned structure, which has been observed for gold, evaporated on cleaved rocksalt [Og72] and mica [Al67]. Multiply twinned structures in gold particles, prepared as described above, were recently observed in our institute by Perenboom [Pe76].

c Mossbauer measurements

To illustrate the quality of the data we give in Figure 8.7 the spectra of sample 3 measured at 4.2 and $40^\circ K$ and of a annealed gold foil (99 mg/cm^2) measured at $4.2^\circ K$ with the same source. The line position of the small particle samples with respect to this gold foil is given in Table 8.1. In the spectra there is no indication of broadening other than caused by saturation effects, except for sample 1 where an asymmetric lineshape was observed, see Figure 8.8.

The effective absorber thickness t_a (Eq. 4.8) was derived from the area of the least-square-fitted Lorentzians as explained in section 4.4, where we mentioned that it is assumed that the fraction of 77 keV Mossbauer radiation, contributing to the detector current, is independent of the absorber. To check this, samples 3 and 4 as well as the gold foil were measured together with a quadrupole split Au^{III} compound. The absorption lines of this compound are sufficiently separated from the single gold line to allow direct comparison of the absorption areas. The effective thickness t_a determined in this way agrees within accuracy ($\pm$ 2%) with that obtained by the first method.
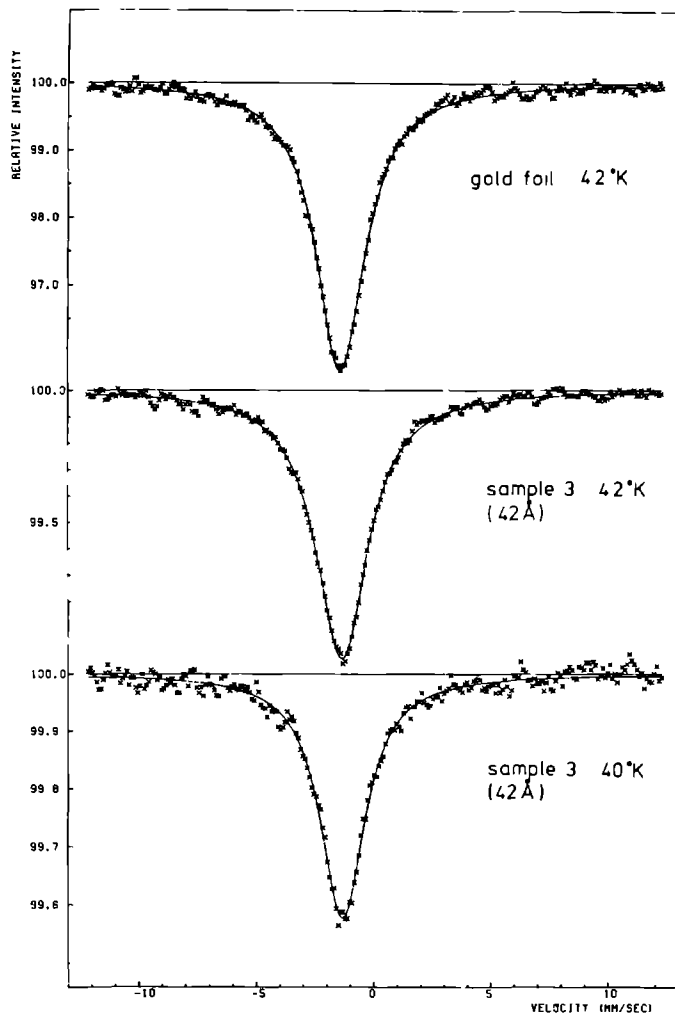
Figure 8.7 Mössbauer spectra of a 99 mg/cm² gold foil at 4.2°K and microcrystal sample 3 at 4.2°K and 40°K. The drawn line is a least-square-fitted Lorentzian.
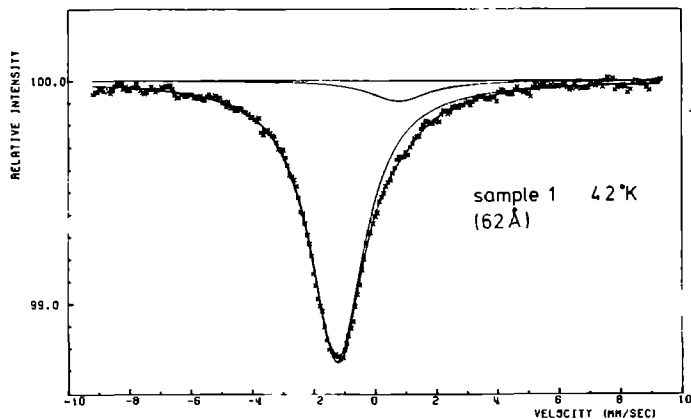
Figure 8.8 Asymmetric absorption line-shape of sample 1. The spectrum was fitted with two Lorentzians, from which the absorption area was determined.

From the values of t_a at 4.2^OK, f_a was derived using the known value of σ [Er71] and the measured n_o. The results are listed in Table 8.1. Errors given are based on the statistical accuracy of the data involved. Systematic errors in f_a may result from slight dehydration of the gelatin, which results in a skrinking of the sample, and from inhomogeneous packing. The latter may be caused by the thready nature of the gelatin.
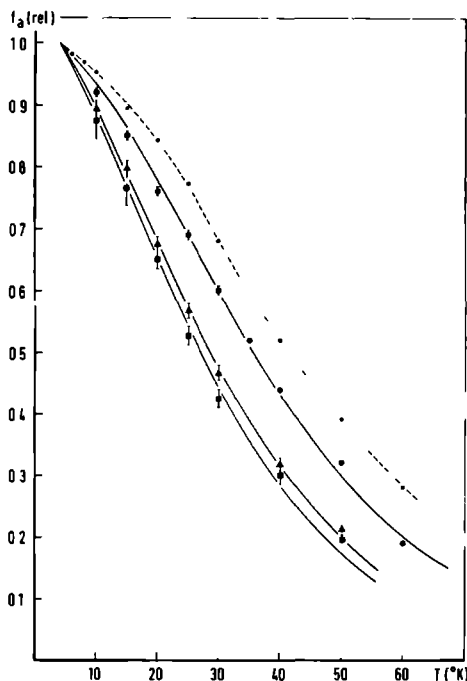
Figure 8.9   Observed temperature dependence of the Mössbauer
fraction f_a relative to f_a at 4.2^OK. · bulk gold
[Er71], ● sample 2 (176 Å), ▲ sample 1 (62 Å),
■ sample 3 (42 Å). The solid curves are least squares
fits to the experimental points using Eq. 8.22 (model
D). In this model the particles are vibrating as a
whole with an Einstein frequency Θ_E, which is the
only free parameter in the fit. The vibrations within
the particle are described by a Debye spectrum (Eq.
8.7), with $\Theta_D = 168^O$K, the value of bulk gold.

Temperature dependent measurements were carried out on sample 1, 2 and 3. For each temperature the absorption area was converted to an effective thickness t_a in the way described above. The temperature dependence of f_a normalized to unity at $4.2^{\circ}K$ is given in Figure 8.9. Systematic errors due to inhomogeneous packing and skrinking are thus eliminated. Also given in Figure 8.9 is $f_a(T)/f_a(4.2^{\circ}K)$ for bulk gold as measured by Erickson et al. [Er71].

8 4 Discussion

a Phonon spectrum

It appears from the results listed in Table 8.1, that there is no clear correlation between the Mossbauer fraction at $4.2^{\circ}K$ and the average particle diameter. In fact if we average all measured values of f_a we find $f_a(4.2^{\circ}K) = 18.8\%$, very close to the value of 18.90% found for bulk gold at $4.2^{\circ}K$ [Er71]. Thus it can be concluded that at $4.2^{\circ}K$ the Mossbauer fraction of small gold particles in gelatin is not much different from bulk gold. The temperature dependence of f_a on the other hand is clearly correlated with particle size. Any valid explanation of the temperature dependence should result in a value of $f_a(4.2^{\circ})$ close to the bulk value.

We have tried to fit the measured values of $f_a(T)/f_a(4.2^{\circ}K)$ with the three models treated in section 8.2 These are:

A: A Debye frequency distribution, Eq. 8.8. The only free parameter in the fit was 0_D. The best fits are plotted in Figure 8.10 together with the measured points. The corresponding values of 0_D are listed in Table 8.2 together with the Mossbauer fraction at $4.2^{\circ}K$ calculated with the parameters of the best fit. It is clear from Figure 8.10 that the single Debye model cannot reproduce the observed temperature dependence. Moreover the calculated Mossbauer fraction at $4.2^{\circ}K$ is too low.

B· No appreciable improvement is obtained when we use Eq. 8.14 even though we have now two free parameters 0_L and 0_H. See curve B in Figure 8.10. In fact the calculated temperature dependence is practically equal to that found with Eq 8.8. The parameters corresponding with the curves B in Figure 8.10 are given in Table 8.2.

C Allowing different vibration amplitudes for bulk and surface atoms by using Eq. 8.15 with a $f_a^S(T)$ and $f_a^B(T)$ given by Eq. 8.8 with different 0_D,
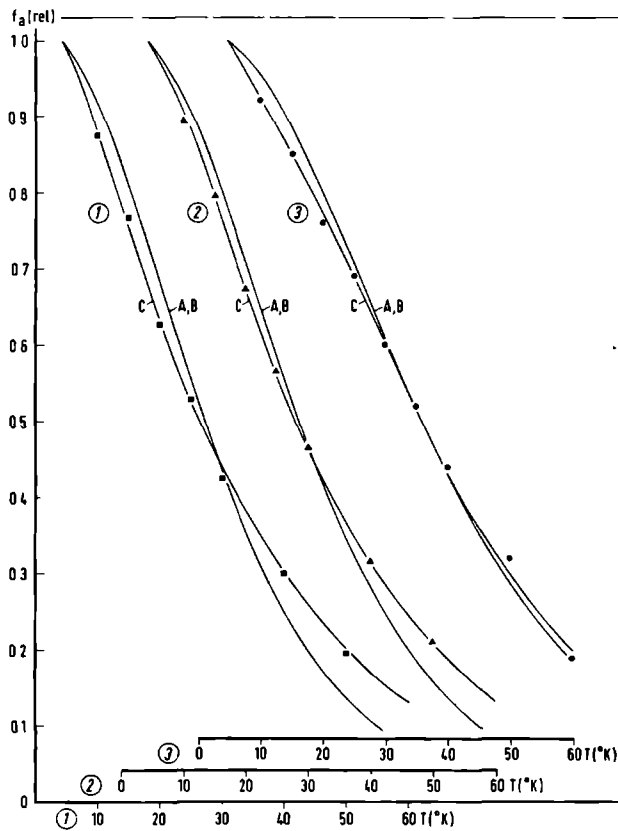
Figure 8.10 Least squares fits to the experimental points, • sample 2
(176 Å), ▲ sample 1 (62 Å), ■ sample 3 (42 Å).

A: Using the Debye theory (Eq. 8.8) with O_D as free parameter.

B: Using the Debye theory including surface and edge modes
(Eq. 8.14) with O_L and Θ_H as free parameters.

C: Summing the independent contributions of the surface
and bulk atoms (Eq. 8.15) with θ_D^S, O_D^B and α as free
parameters.

excellent fits to the measured $f_a(T)$ are obtained. See Figure 8.10, curve
C. In the fit three free parameters were used: α, O_D^S and O_D^B. The results
are given in Table 8.2. Apart from the fact that α is rather small the
calculated value of f_a at 4.2°K is much too low. If θ_D^B and O_D^S are fixed at
168°K and 83°K respectively good fits can still be found, but no appreci-

129

able increase in f_a is obtained.
We conclude therefore that none of the models used gives a satisfactory explanation of the measured $f_a(T)$.

Table 8.9

Model A Eq 8 8	θ_D (°K)	f_a (4 2°K)$_{calc}$ (%)		
Sample 3 (42 Å)	123	9 8		
Sample 1 (62 Å)	128	10 7		
Sample 2 (176 Å)	148	14 5		

Model B Eq 8 14	θ_L (°K)	θ_H (°K)	f_a (4 2°K)$_{calc}$ (%)	
Sample 3 (42 Å)	2 6	129	10 5	
Sample 1 (62 Å)	2 6	133	11 4	
Sample 2 (176 Å)	2 8	154	15 2	

Model C Eq 8 15	α	θ_D^{bulk} (°K)	θ_D^{surf} (°K)	f_a (4 2°K)$_{calc}$ (%)
Sample 3 (42 Å)	0 28	148	78	5 8
Sample 1 (62 Å)	0 37	150	87	7 8
Sample 2 (176 Å)	0 22	153	51	3 7

Model D Eq 8 22	θ_E (°K)	f_a (4 2°K)$_{calc}$ (%)		
Sample 3 (42 Å)	3 1	16 1		
Sample 1 (62 Å)	1 9	16 4		
Sample 2 (176 Å)	0 65	17 0		

In the foregoing discussion we assumed, in line with general practice, that only vibrations within the particle contribute to the vibrational amplitude of the gold atoms. Vibrations of the particle as a whole are assumed to be negligibly small because of the large mass of the particle. On the other hand the opposite approach has been used for molecular crystals [Go68] . In these crystals molecules are bound by Van der Waals forces, that are weak compared with intramolecular forces and the Mossbauer fraction is dominated by the vibrations of the molecular units as a whole in spite of

their larger mass. It is illustrative to consider a harmonic oscillator with frequency

$$\omega = \sqrt{\frac{q}{m}} \quad , \tag{8.17}$$

where q is the binding force constant and m is the mass of the vibrating particle. The mean square vibrational amplitude is given by [We65]

$$< x^2 > = \frac{\hbar}{2m\omega} \{\frac{2}{\exp(\frac{\hbar\omega}{kT})-1} + 1\} \tag{8.18}$$

For T = 0

$$< x^2 > = \frac{\hbar}{2m\omega} = \frac{\hbar}{2} \sqrt{\frac{1}{q \cdot m}} \tag{8.19}$$

and it is clear that in molecular crystals the effect of the large molecular mass can be compensated by a weaker binding force. For the small particles investigated by us the mass is two orders of magnitude larger than the mass of a molecular unit and one may assume that $< x^2 >_{T=0}$ is indeed very small. But at the same time ω (Eq. 8.17) is reduced and consequently the exponential in Eq. 8.18 becomes more important at lower temperatures.

In molecular crystals intermolecular vibrations are of the order of 100°K whereas the mass is typically 3 to 10 times the mass of the Mössbauer nucleus. Assuming similar binding forces one estimates the vibration frequency of a particle with $10^3 \sim 10^4$ atoms to be in the order of $1 \sim 10^\circ$K. For kT > $3\hbar\omega$, $< x^2 >$ is given by:

$$< x^2 > = \frac{kT}{q} \quad , \tag{8.20}$$

and independent of the mass. Thus at very low temperatures the large mass causes such a small vibrational amplitude of the particle that $f_a(T)$ at these temperatures is mainly determined by the vibrations within the particle, but at only slightly higher temperatures the vibration of the particle as a whole results in a considerable decrease of the Mössbauer fraction.

The gold particles investigated by us are bound by Van der Waals forces

to the gelatin matrix. Because the average distance between the particles is large compared to their diameter, vibrational coupling between the particles can be neglected. The vibration is then best described by a localized mode, so that the Einstein model is applicable. Furthermore we assume that there is no coupling between this Einstein mode and the phonons in the particle. Then

$$< x^2 >_{tot} = < x^2 >_{part} + < x^2 >_{latt} \qquad , \qquad (8.21)$$

where $< x^2 >_{part}$ is the mean squared vibrational amplitude of the particle as a whole and consequently

$$f_a^{tot} = f_a^{part} \cdot f_a^{latt} \qquad , \qquad (8.22)$$

f_a^{part} is given by:

$$f_a^{part}(T) = \exp \left\{ \frac{h^2}{2m\lambda^2} \cdot \frac{1}{k\Theta_E} \left[\frac{2}{\exp(\frac{\Theta_E}{T})-1} + 1 \right] \right\} \qquad , \qquad (8.23)$$

as follows by substituting Eq. 8.18 into Eq. 8.1, with $\Theta_E = \hbar\omega/k$ the Einstein temperature.

We applied Eq. 8.22 to analyse the measured temperature dependence of f_a. For f_a^{latt} Eq. 8.8 was used with Θ_D held at $168^\circ K$, the value found for bulk gold [Er71]. The only free parameter in the fit is Θ_E of Eq. 8.23. For m the mass corresponding with the effective average diameter was used. The values of Θ_E, that gave the best fit are listed in Table 8.2, model D, and the calculated temperature dependence is plotted in Figure 8.9. In view of the fact, that only one free parameter is used, the fits are excellent. Moreover the values of Θ_E are of the expected order of magnitude and the absolute Mössbauer fraction calculated with these values agrees reasonably with the measured values (Table 8.1). If Θ_D is also taken as a free parameter the fits are not significantly improved. Similarly, if for f_a^{latt} Eq. 8.14 is used with Θ_L and Θ_H as free parameters, no significant improvement is found, in agreement with the results of fits A and B.

132

The isomer shift is proportional to the electron density at the nucleus. According to Thomson et al. [Th75] addition of one 6s electron results in a shift of +8 mm/sec. From Table 8.1 no simple correlation between isomer shift and particle size can be derived, except that all samples have a shift, positive with respect to bulk gold. As no line broadening is observed, the electron density at the nuclei is the same for surface and inner atoms.

Schroeer [Sc70] has correlated the isomer shift with lattice contraction using two samples of same average size, but giving different isomer shifts. The lattice contraction was determined from the displacement of X-ray Bragg-diffraction peaks. This procedure has recently been questioned by Briant and Burton [Br75]. The shifts observed by us are of the same order of magnitude as those of Schroeer [Sc70].

8 5 Conclusion

We conclude that to explain the temperature dependence of the Mössbauer fraction of gold microcrystals as well as its value at 4.2°K it is necessary to take into account the vibration of the particle as a whole. This has implications for the study of the phonon spectrum of small particles by means of the Mössbauer effect, because the vibration of the particle as a whole overshadows possible size effects and if the particles are bound more tightly the nature of the surface will be affected. Motion of the particles does not affect the Debye-Waller factor for neutron or X-ray diffraction, so that these methods are more suitable for the study of the phonon spectrum of small particles. Such methods applied to 107 Å lead particles in porous glass [No74] and 234 Å gold particles in an Argon matrix [Pe71] indicate an increase in vibrational amplitude of the atoms.

The importance of the binding of small particles for the Mossbauer effect was earlier pointed out by Van Wieringen [Wi68]. In fact Van der Giessen, Rensen and Van Wieringen [Gi68] found a large difference in temperature dependence of the Mössbauer fraction of ^{57}Fe in small particles of FeOOH in a gel and dried. Thus it appears that the Mossbauer effect of small particles can be used to study binding to the medium containing the particles rather than the particles themselves.

REFERENCES

Ab61   A. Abragam, "The Principles of Nuclear Magnetism", Oxford (1961).

Ab64   A. Abragam, "L'effet Mössbauer et ses Applications à l'étude des
        Champs Internes", New York (1964).

Ab70   A. Abragam and B. Bleaney, "Electron Paramagnetic Resonance of
        Transition Ions", Oxford (1970).

Af63   A.M. Afanes'ev and Yu. Kagan, J.E.T.P., $\underline{45}$, 1660 (1963).

Ak59   S. Åkerström, Arkiv Kemi, $\underline{14}$, 387 (1953).

Ak75   S. Akselrod, M. Pasternak and S. Bukshpan, Phys. Rev. B, $\underline{11}$, 1040 (1975).

Al67   J.G. Allpress and J.V. Sanders, Surface Science, $\underline{7}$, 1 (1967).

Ba64   G.A. Baker, Jr., G.S. Rushbrooke and H.E. Gilbert, Phys. Rev. A, $\underline{135}$,
        1272 (1964).

Ba70   H.D. Bartunik, W. Potzel, R.L. Mössbauer and G. Kaindl, Z. Physik,
        $\underline{240}$, 1 (1970).

Ba74   N.C. Baenziger, K.M. Dittemore and J.R. Doyle, Inorg. Chem., $\underline{13}$, 805
        (1974).

Be68a   P.T. Beurskens, H.J.A. Blaauw, J.A. Cras and J.J. Steggerda, Inorg.
        Chem., $\underline{7}$, 805 (1968).

Be68b   P.T. Beurskens, J.A. Cras and J.J. Steggerda, Inorg. Chem., $\underline{7}$, 810
        (1968).

Be68c   L.H. Bennett, R.W. Mebs and R.E. Watson, Phys. Rev., $\underline{171}$, 611 (1968).

Be69   P.L. Bellon, M. Manzerro and M. Sansoni, Ric. Sci., $\underline{39}$, 173 (1969).

Be70a   P.T. Beurskens, J.A. Cras and J.G.M. van der Linden, Inorg. Chem.,
        $\underline{9}$, 475 (1970).

Be70b   P.T. Beurskens, J.A. Cras, Th.W. Hummelink and J.G.M. van der Linden,
        Rec., $\underline{89}$, 984 (1970).

Be71   A.I. Beskrovny and Yu.M. Ostanevich, Pribory i Tekhn. Eksperim., $\underline{14}$,
        54 (1971); Engl. transl.: Instr. Exptl. Tech. (USSR), $\underline{14}$, 1320 (1971).

Bl64   H.J.A. Blaauw, R.J.F. Nivard and G.J.M. van der Kerk, J. Organometal.
        Chem., $\underline{2}$, 236 (1964).

Bl65   H.J.A. Blaauw, Ph.D. Thesis, Nijmegen (1965).

Bl67   A.G. Blachman, D.A. Landman and A. Lurio, Phys. Rev., $\underline{161}$, 60 (1967).

Bo64   J.C. Bonner and M.E. Fisher, Phys. Rev. A, $\underline{135}$, 640 (1964).

Bo65   M. Bonamico, G. Dessy and V. Vaciago, Rend. Acad. Lincei, ser. VIII,
        $\underline{39}$, 504 (1965).

Bo73   V.N. Bogomolov and N.A. Klushin, Fiz. Tverd. Tela, $\underline{15}$, 514 (1973);
        Engl. transl.: Sov. Phys. Solid State, $\underline{15}$, 357 (1973).

Br52   F.H. Brain, C.S. Gibson, J.A.J. Jarvis, R.F. Phillips, H.M. Powell
        and A. Tyabji, J. Chem. Soc., 3686 (1952).

Br62   D.M. Brink and G.R. Satchler, "Angular Momentum", Oxford (1962).

Br75   C.L. Briant and J.J. Burton, Surface Science, $\underline{51}$. 345 (1975).

Bu70   J.J. Burton, J. Chem. Phys., $\underline{52}$. 345 (1970).

By63   G.A. Bykov and Pham Zuy Hien, Zh. Eksperim. i Teor. Fiz., $\underline{43}$, 909
        (1962); Engl. transl.: Sov. Phys. JETP, $\underline{16}$, 646 (1963).

Ch66   W.J. Childs and L.S. Goodman, Phys. Rev., $\underline{141}$, 176 (1966).

Ch70   J.S. Charlton and D.I. Nichols, J. Chem. Soc. (A), 1484 (1970).

Co36   E.G. Cox and K.G. Webster, J. Chem. Soc., 1635 (1936).

Co61   C.A. Coulson, "Valence", Oxford (1961).

Co62   G.E. Coates and C.J. Parkin, J. Chem. Soc., 3220 (1962).

Co64   E.U. Condon and G.H. Shortley, "The Theory of Atomic Spectra",
        Cambridge (1964).

Co67   P.W.R. Corfield and H.M.M. Shearer, Acta Cryst., $\underline{23}$, 156 (1967).

Co70   D. Coucouvanis, Progr. Inorg. Chem., $\underline{11}$, 233 (1970).

Co72   F.A. Cotton and G. Wilkinson, "Advanced inorganic chemistry",
        New York (1972).

Cr70   J.A. Cras, J.H. Noordik, P.T. Beurskens and A.M. Verhoeven, J. Cryst.
        Mol. Struct., $\underline{1}$, 155 (1970).

Cr73   T.E. Cranshaw, J. Phys. E., $\underline{6}$, 1 (1973).

Cr74   T.E. Cranshaw, J. Phys. E., $\underline{7}$, 122 (1974); $\underline{7}$, 497 (1974).

Da63   A. Davison, N. Edelstein, R.H. Holm and A.K. Maki, Inorg. Chem., $\underline{2}$,
        1227 (1963).

Da67   A. Davison, D.U. Howe and E.T. Shawl, Inorg. Chem., $\underline{6}$, 458 (1967).

Da68   W.C. Davidon, Comp. J., $\underline{10}$, 406 (1968).

De90   M. Dennstedt, Chem. Ber., $\underline{23}$, 2570 (1890)

Di73   E. Diemann and A. Müller, Coord. Chem. Rev., $\underline{10}$, 79 (1973).

Do76   H. Dornfeld, Institute for Chemistry, University of Dortmund.

Ei70   R. Eisenberg, Progr. Inorg. Chem., $\underline{12}$, 295 (1970).

Ep74   V.N. Epikhin and I.N. Nikolaev, Fiz. Tverd. Tela, $\underline{16}$, 3120 (1974);
        Engl. transl.: Sov. Phys. Solid State, $\underline{16}$, 2017 (1975).

Er71   D.J. Erickson, L.D. Roberts, J.W. Burton and J.O. Thomson, Phys. Rev.
        B, $\underline{3}$, 2180 (1971).

Er73   D.J. Erickson, J.F. Prince and L.D. Roberts, Phys. Rev. C, $\underline{8}$, 1916
        (1973).

Fa69   M.O. Faltens, Ph.D. Thesis, Berkeley (1969).

Fa70   M.O. Faltens and D.A. Shirley, J. Chem. Phys., $\underline{53}$ 4249 (1970).

Fa71   F.J. Farrell and T.G. Spiro, Inorg. Chem., 10, 1606 (1971).

Fe69   F.D. Feiock and W.R. Johnson, Phys. Rev., 187, 39 (1969).

Fo59   S. Foner, Rev. Sci. Instr., 30, 548 (1959).

Fo64   J.D. Forrester, A. Zalkin and D.H. Templeton, Inorg. Chem., 3, 1507
        (1964).

Fr65   H. Frauenfelder and R.M. Steffen, "Alpha-, Beta- and Gamma-Ray
        Spectroscopy", K. Siegbahn ed., Amsterdam (1965).

Fr68   R. Fritz and D. Schulze, Nucl. Instr. Meth., 62, 317 (1968).

Ga71   P. Gans, "Vibrating Molecules", London (1971).

Gi68   A.A. van der Giessen, J.G. Rensen and J.S. van Wieringen, J. Inorg.
        Nucl. Chem., 30, 1739 (1968).

Go62   U. Gonser, J. Phys. Chem., 66, 564 (1962).

Go68   V.I. Goldanskii and R.H. Herber, eds., "Chemical Applications of
        Mössbauer Spectroscopy", New York (1968).

Go69   G. Goldmann, C. Hahn and J. Ney, Z. Physik, 225, 1 (1969).

Gr71   N.N. Greenwood and T.C. Gibb, "Mössbauer Spectroscopy", London (1971).

Gu72   J.M. Guss, R. Mason, K.M. Thomas, G. van Koten and J.G. Noltes, J.
        Organometal. Chem., 40, C79 (1972).

Ha64   W.C. Hamilton, "Statistics in Physical Science", New York (1964).

Ha73   Y. Hazony and R.H. Herber, "Mössbauer effect methodology", vol. 8,
        (1973).

Ha74   Y. Hazony and R.H. Herber, J. de Physique, Coll., 35, C6-131 (1974).

He05   F. Herrmann, Ber., 38, 2813 (1905).

He61   R. Hesse, "Advances in the Chemistry of Coordination Compounds",
        S. Kirschner ed., New York (1961).

He72   R. Hesse and P. Jennische, Acta Chem. Scand., 26, 3855 (1972).

Ho65   C. Hohenemser, Phys. Rev. A, 139, 185 (1965).

Hu72   J.E. Huheey, "Inorganic Chemistry", New York (1972).

Ja68   F. James, Proceedings of 1968 Hercey-Novi School, London (1968).

Ja69   F. James and M. Roos, MINUIT, CERN, Geneva, programme D-506.

Jo57   L.H. Jones, J. Chem. Phys., 27, 468 (1957).

Jo62   C.K. Jørgensen, "Absorption Spectra", Oxford (1962).

Ka62   Yu. Kagan and Ya.A. Iosilevskii, Sov. Phys. JETP, 15, 182 (1962).

Ka62   B. Kaufman and H.L. Lipkin, Ann. Phys., 18, 294 (1962).

Ka64   E. Kankeleit, Rev. Sci. Instr., 35, 194 (1964).

Ka73   G. Kaindl, K. Leary and N. Bartlett, J. Chem. Phys., 59, 5050 (1973).

Ka75   E. Kankeleit, "Proceedings International Conference on Mossbauer
        Spectroscopy", Vol. 2, Cracow (1975).

Ki71   R. Kirmse, W. Windsch and E. Hoyer, Z. Anorg. Allg. Chem., $\underline{386}$,
       213 (1971).

Kl59   H.P. Klug and L.E. Alexander, "X-ray diffraction procedures", John
       Wiley & Sons, Inc., New York (1959) chapter 9.

Ko58   H. Kopfermann, "Nuclear Moments", New York (1958).

Ko72   G. van Koten and J.G. Noltes, J. Chem. Soc. Chem. Comm., 940 (1972).

Ko73   M. Kostelitz and J.L. Domange, Solid State Comm., $\underline{13}$, 241 (1973).

Ko74a   G. van Koten and J.G. Noltes, J. Organometal. Chem., $\underline{82}$, C53 (1974).

Ko74b   G. van Koten and J.G. Noltes, J. Organometal. Chem., $\underline{80}$, C56 (1974).

Ko76   G. van Koten, J.T.B.H. Jastszebski and J.G. Noltes, Inorg. Chem.,
       (to be published).

Ko76a   G. van Koten, Institute for Organic Chemistry, TNO Utrecht.

Kr52   H.R. Kruyt ed., "Colloid Science", Elsevier Publications, Co.,
       Amsterdam (1952).

La63   G. Lang, Nucl. Instr. Meth., $\underline{24}$, 425 (1963).

La69   G. Lang and W.T. Oosterhuis, J. Chem. Phys., $\underline{51}$, 3608 (1969).

La72   S.L. Lawton, W.J. Rohrbaugh and G.T. Kokotailo, Inorg. Chem., $\underline{11}$,
       2227 (1972).

Le72   K. Leary and N. Bartlett, J. Chem. Soc. Chem. Comm., 903 (1972).

Li71a   J.G.M. van der Linden, Rec., $\underline{90}$, 1027 (1971).

Li71b   J.G.M. van der Linden and H.G.J. van de Roer, Inorg. Chim. Acta, $\underline{5}$,
       254 (1971).

Li73   J.G.M. van der Linden, Ph.D. Thesis, Nijmegen (1973).

Li74   T.M. Lin and R.S. Preston, Mössbauer Effect Methodology, Vol. 9,
       New York (1974).

Li76   J.G.M. van der Linden, Dept. Inorganic Chemistry, University of Nijmegen.

Lo44   A.E.H. Love, "A treatise on the mathematical theory of elasticity",
       Dover publications, Inc., (1944).

Ma61   S. Margulies and J.R. Ehrman, Nucl. Instr. Meth., $\underline{12}$, 131 (1961).

Ma64   A.H. Maki, N. Edelstein, A. Davison and R.H. Holm, J. Am. Chem. Soc.,
       $\underline{86}$, 4580 (1964).

Ma66   S.W. Marshall and R.M. Wilenzick, Phys. Rev. Lett., $\underline{16}$, 219 (1966).

Ma72   A.A. Maradudin, R.F. Wallis, D.L. Mills and R.L. Ballard, Phys. Rev. B,
       $\underline{6}$, 1106 (1972).

Mc64   D.D. McCracken and W.S. Dorn, "Numerical Methods and Fortran program-
       ming", New York (1964).

Mc67   B.R. McGarvey, J. Chem. Phys., $\underline{46}$, 51 (1967).

Mo50   E.W. Montroll, J. Chem. Phys., _18_, 183 (1950).

Mo72   R.L. Mössbauer, as quoted in "Mössbauer Spectroscopy and its
        Applications", (IAEA, Vienna, 1972) p.87.

Ni69   D.I. Nichols and A.S. Charleston, J. Chem. Soc. A, 258 (1969).

No71a   J.H. Noordik, Ph.D. Thesis, Nijmegen (1971).

No71b   J.H. Noordik and P.T. Beurskens, J. Cryst. Mol. Struct., _1_, 339
        (1971).

No73   J.H. Noordik, Th.W. Hummelink and J.G.M. van der Linden, J. Coord.
        Chem., _2_, 185 (1973).

No74   V. Novotny, T.M. Holden and G. Dolling, Can. J. Phys., _52_, 748 (1974).

Nu66   R.H. Nussbaum, "Interpretation and Applications of Mossbauer fraction
        experiments", Mossbauer Effect Methodology, Vol. 2, New York (1966).

Og72   S. Ogawa and S. Ino, J. Crystal Growth, _13/14_, 48 (1972).

Op75   A.V. Oppenheim and R.W. Schafer, "Digital Signal Processing",
        Englewood Cliffs (1975).

Pa35   W. Pauli, Trans. Farad. Soc., _31_, 11 (1935).

Pa63   L. Pauling, "The Nature of the Chemical Bond", New York (1963).

Pa70   D.O. Patterson, J.O. Thomson, P.G. Hurray and L.D. Roberts, Phys.
        Rev. B, _7_, 2440 (1970).

Pe71   Yu.I. Petrov and V.A. Kotel'inkov, Fiz. Tverd. Tela, _13_, 313 (1971);
        Engl. transl.: Sov. Phys. Solid State, _13_, 255 (1971).

Pe76   J.A.A.J. Perenboom, Private Communication.

Pi74   F.W. Pijpers, A.H. Dix and J.G.M. van der Linden, Inorg. Chim. Acta,
        _11_, 41 (1974).

Pl75   K.W. Plumlee, B.M. Hoffman, J.A. Ibers and Z.G. Soos, J. Chem. Phys.,
        _63_, 1926 (1975).

Pr62   R.S. Preston, S.S. Hanna and J. Heberle, Phys. Rev., _128_, 2207 (1962).

Pr75   H. Prosser, F.E. Wagner, G. Wortmann, G.M. Kalvius and R. Wappling,
        Hyp. Int., _1_, 25 (1975).

Re60   D.C. Reitz and S.I. Weissman, J. Chem. Phys., _33_, 700 (1960).

Re70   J.G.M. van Rens and E. de Boer, Mol. Phys., _19_, 745 (1970).

Re74   J.G.M. van Rens, Ph.D. Thesis, Nijmegen (1974).

Re75   A.J. Rein and R.H. Herber, J. Chem. Phys., _63_, 1021 (1975).

Re75a   J.G.M. van Rens, M.P.A. Viegers and E. de Boer, Chem. Phys. Lett.,
        _28_, 104 (1974).

Re75b   J.G.M. van Rens and E. de Boer, Chem. Phys. Lett., _31_, 377 (1975).

Ro60   H.H. Rosenbrock, Comp. J., _3_, 175 (1960).

Ro62   L.D. Roberts, H. Pomerance, J.O. Thomson and C.F. Dam, BAPS, <u>7</u>,
        565 (1962).

Ro65   L.D. Roberts, R.L. Becker, F.F. Obenshain and J.O. Thomson, Phys.
        Rev, <u>137</u>, A895 (1965).

Ro67   S. Roth and E.M. Horl, Physics Lett., <u>25A</u>, 299 (1967).

Ro69   L.D. Roberts, D.O. Patterson, J.O. Thomson and R.P. Levey, Phys. Rev.,
        <u>179</u>, 656 (1969).

Ro75   L.D. Roberts, "Mossbauer Effect Data Index 1973", J.G.Stevens and
        V.E. Stevens, eds., New York (1975).

Sc70   D. Schroeer, R.F. Marzke, D.J. Erickson, S.W. Marshall and R.M.
        Wilenzick, Phys. Rev. B, <u>2</u>, 4414 (1970).

Sc74   R.L Schlupp and A.H. Maki, Inorg. Chem., <u>13</u>, 44 (1974).

Sh61   D.A. Shirley, M. Kaplan and P. Axel, Phys. Rev., <u>123</u>, 816 (1961).

Sh64   D.A. Shirley, Rev. Mod. Phys., <u>36</u>, 339 (1964).

Sh74   G.K. Shenoy, J.M. Friedt, H. Maletta and S.L. Ruby, Mossbauer Effect
        Methodology, Vol. 9, New York (1974).

Si66   H. Siebert, "Anwendungen der Schwingungsspektroskopie in der anorga-
        nischen Chemie", New York (1966).

So73   D.M. Soboroff, Ph.D. Thesis, Iowa (1973).

St50   R. Sternheimer, Phys. Rev., <u>80</u>, 102 (1950); <u>84</u>, 244 (1951); R. Stern-
        neimer and H.M. Foley, Phys. Rev., <u>102</u>, 731 (1956).

St70   J. Strahle and H. Barnighausen, Z. fur Naturforsch., <u>10</u>, 1186 (1970).

Su58   L.E. Sutton, ed., Chem. Soc. Spec. Publ., <u>11</u>, 53 (1958).

Su66   I.P. Suzdalev, M.Ya. Gen, V.I. Goldanskii and L.F. Makarov, J. Exptl.
        Theoret. Phys., <u>51</u>, 118 (1966); Engl. transl. Sov. Phys. JETP, <u>24</u>,
        79 (1967).

Th75   J.O. Thomson, F.E. Obenshain, P.G. Huray, J.C. Love and J. Burton,
        Phys. Rev. B, <u>11</u>, 1835 (1975).

Tu51   J. Turkevich, P.C. Stevenson and J. Hillier, Disc. Farad. Soc., <u>11</u>,
        55 (1951).

Vi74   M.P.A. Viegers and J.M. Trooster, Nucl. Instr. Meth., <u>118</u>, 257 (1974).

Vi76   M.P.A. Viegers, H. Dornfeld and A. Muller, to be published.

Vl32   J.H. van Vleck, "The theory of electric and magnetic susceptibilities",
        Oxford (1932).

Vr75   J.L.K.F. de Vries, J.M. Trooster and P. Ros, J. Chem. Phys., <u>63</u>,
        5256 (1975).

Wa65   J.H. Waters and H.B. Gray, J. Am. Chem. Soc., <u>87</u>, 3534 (1965).

Wa71   J.H. Waters, T.J. Bergendahl and S.R. Lewis, Chem. Comm., 834 (1971).

Wa75   D. Walcher, A. Matla, R. Gruner and W. Wurtinger, as quoted in [Ka75].

We64   G.K. Wertheim, "Mössbauer Effect: Principles and Applications", New
        York (1964).

We65   H. Wegener, "Der Mossbauer Effect und seine Anwendung in Physik und
        Chemie", Mannheim (1965).

We68   M.J. Weeks and J.P. Fackler, Inorg. Chem., 12, 2548 (1968).

We75   H.Wegener, "Proceedings International Conference on Mossbauer
        Spectroscopy", Vol. 2, Cracow (1975).

Wh66   R.L. White, "Basic Quantum Mechanics", New York (1966).

Wi68   J.S. van Wieringen, Phys. Lett., 26A, 370 (1968).

Wi69   J.M. Williams and S.W. Peterson, J. Am. chem. Soc., 91, 776 (1969)

Wi72   J.G. Wijnhoven, W.P.J.H. Bosman and P.T. Beurskens, J. Cryst. Mol.
        Struct., 2, 7 (1972).

Wi75   J.M. Williams and J.S. Brooks, Nucl. Instr. Meth., 128, 363 (1975).

Wi76   J. Willemse, J.A. Cras, J.J. Steggerda and C.P. Keijzers, "Dithio-
        carbamates of transition group elements in unusual oxidation states",
        to be published in "Structure and Bonding".

SAMENVATTING

van wat er eigenlijk in dit proefschrift staat

Met de bedoeling om meer inzicht te verkrijgen in de binding van goud
atomen in verschillende materialen is de kern van het goud atoom (^{197}Au)
bestudeerd met behulp van het Mössbauer effect (ontdekt door Rudolph Möss-
bauer in 1958). Met deze spectroscopische techniek kunnen zeer kleine ver-
anderingen worden waargenomen in de energie van de γ(gamma)-straling die door
de kern wordt uitgezonden of geabsorbeerd. Deze verschillen worden veroor-
zaakt door een wisselwerking tussen de kern van het atoom en zijn omgeving
(de hyperfijn wisselwerking) en geven daardoor informatie over de verdeling
van de electronen in de buurt van de kern. Bovendien geeft het Mössbauer
effect informatie over de stevigheid, waarmee het atoom in de vaste stof
gebonden is. Immers het uitzenden en absorberen van straling gaat gepaard
met een terugstoot, die opgevangen moet worden zonder dat het atoom zich
verplaatst in het kristal, waarin het zich bevindt. Dit gaat beter naarmate
het atoom steviger in het kristal is gebonden en geeft dan aanleiding tot
een grotere absorptie.

Voor de bestudering van de absorptie van γ-straling is een bron nodig,
die goud atomen bevat, die deze γ-straling uitzenden. Zo'n bron kan gemaakt
worden door platina in een kernreactor te bestralen met neutronen. Dan wordt
o.a. de radioactieve isotoop ^{197}Pt gevormd, die spontaan verandert in ^{197}Au
onder uitzending van de gewenste straling. Het radioactieve platina heeft
echter slechts een korte levensduur waardoor het na 3 dagen al niet meer te
gebruiken is, ofschoon het in het begin een hoge activiteit heeft. Derhalve
moest de bestaande apparatuur worden aangepast om veilig en snel met deze
sterke maar kortlevende bronnen te kunnen werken. Daarbij werd een nieuwe
methode ontwikkeld om de intensiteit van γ-straling te meten waardoor een
zeer efficiënt gebruik gemaakt kon worden van de beschikbare radioactiviteit.

Goud, dat bekend is als edel metaal, komt ook voor in een grote ver-
scheidenheid van scheikundige verbindingen. De meeste verbindingen zijn niet
magnetisch. Het goud atoom heeft dan 1 of 3 electronen afgestaan (resulterend
in zgn. 1- of 3-waardig goud) en is vervolgens chemisch gebonden aan andere
atomen. De zo ontstane, over het algemeen gecompliceerde moleculen vertonen
de opvallende eigenschap dat 3-waardig goud steeds omgeven is door 4 buur
atomen in een vlakke omringing en 1-waardig goud door 2 buur atomen in een

keten. Een groot aantal goud verbindingen was reeds eerder onderzocht m.b.v. het Mössbauer effect en gerapporteerd in de litteratuur. De waargenomen tendensen in de hyperfijn effecten konden verklaard worden met een eenvoudig model voor de chemische binding, waarbij de band tussen het goud atoom en zijn buur atoom tot stand komt door een electronen transport langs de bindingsas van dit buur atoom naar het goud atoom: de zg. σ(sigma)-donor-binding. Wanneer dit electronen transport groot is, als bijvoorbeeld koolstof, stikstof of zwavel aan goud gebonden zijn, worden grotere hyperfijn effecten waargenomen dan wanneer het electronen transport klein is, zoals in geval van fluor of chloor. In ons onderzoek is het aantal onderzochte verbindingen met een even zo groot aantal uitgebreid zonder bijzondere afwijkingen van de eerder waargenomen tendensen. Echter, in een poging om de metingen ook quantitatief te verklaren, blijken de hyperfijn effecten veel groter te zijn dan redelijkerwijs met het bovengenoemde model verklaard kan worden. Hiermee is een duidelijke aanwijzing gevonden voor het belang van een tweede electronen transport, de zg. π(pi)-back-donatie, en wel van het goud atoom buiten de σ-binding om terug naar het buur atoom. De π-back-donatie is groter naarmate de σ-donatie ook groter is, zodat we op het goud atoom steeds nage-noeg dezelfde lading zullen aantreffen.

Bij dit onderzoek werden ook metingen verricht aan goud-verbindingen waarin zowel één-waardige als drie-waardige goud atomen voorkomen. Er bleek toen dat de 3-waardige goud atomen (gebonden aan 4 buur atomen) veel beter de terugstoot van de γ-straling konden opvangen dan de 1-waardige (gebonden aan 2 buur atomen). Een voor de hand liggende verklaring zou zijn dat dit ver-oorzaakt wordt door het verschillend aantal buur atomen, waaraan het goud atoom gebonden is. Anderzijds vormt het goud atoom samen met zijn buren een molecuul, dat als geheel kan bewegen t.o.v. andere moleculen in het kristal. Door nu het absorptie gedrag van γ-straling te onderzoeken bij verschillende temperaturen is aan het licht gekomen, dat het goud atoom in een grote variëteit van moleculen steeds even stevig gebonden is binnen het molecuul, maar dat de terugstoot beter opgevangen wordt wanneer de massa van het gehele molecuul groter is. Dit betekent dat uit de mate van absorptie de massa van het molecuul afgeleid kan worden, hetgeen interessant is voor structuur onderzoek van nieuwe goud-verbindingen.

Naast de vele niet magnetische verbindingen is er slechts één magnetische

goud-verbinding in zuivere vorm bekend. In deze verbinding is het goud atoom 2-waardig en heeft het een oneven aantal electronen, zodat er één zgn. ongepaard electron is. Het ongepaard electron gedraagt zich als een magneet en veroorzaakt een magnetisch veld op de plaats van de kern van het goud atoom. De energie van de γ-straling is gevoelig voor de orientatie van de goud kern in dit magneetveld, hetgeen resulteert in een zeer gecompliceerd absorptie spectrum. Om meer inzicht te verkrijgen in de aard van het aanwezige magnetisme is de gevoeligheid van de stof voor een uitwendig aangelegd magneetveld gemeten van kamertemperatuur (300°K) tot bijna bij het absolute nulpunt (0.009°K). Hieruit is gebleken dat de ongepaarde electronen van op een rij liggende goud atomen elkaar beïnvloeden op zo'n manier, dat de kans op tegengesteld gerichte magnetische momenten van de ongepaarde electronen op twee buur atomen groter is dan de kans op evenwijdig gerichte momenten. De Mössbauer metingen kunnen verklaard worden door aan te nemen dat er een magnetische koppeling bestaat tussen de atoomkern en het ongepaarde electron. Met computer berekeningen is de Mossbauer absorptie nagebootst voor het geval dat er één electron is gekoppeld aan de kern, maar ook voor twee electronen die eerst onderling gekoppeld zijn. Omdat er in werkelijkheid meer ongepaarde electronen onderling gekoppeld zijn is geen nauwkeurige nabootsing van het experiment verkregen. Wel is komen vast te staan dat ter plaatse van de kern het magnetisch veld tegengesteld is aan dat van het ongepaarde electron. Hiermee is experimenteel bevestigd wat eerder op grond van de theorie was voorspeld. Verder zijn er Mossbauer experimenten uitgevoerd in een uitwendig aangelegd magneetveld van zo'n sterkte, dat alle ongepaarde electronen zich langs dit veld richten. In dat geval is er niets meer te merken van onderlinge beïnvloeding van de electronen en kan de grootte van het magneetveld ter plaatse van de goud kern bepaald worden. Dit bleek 815 kOe te zijn, ongeveer 5 maal zo groot als de sterkste electromagneet ter wereld.

Tenslotte is Mossbauer onderzoek verricht aan zeer kleine goud deeltjes van verschillende afmetingen, die slechts 1000 tot 10.000 goud atomen bevatten. Trillingen met een golflengte groter dan het deeltje zijn niet mogelijk. Men zou dus kunnen verwachten dat de atomen in zo'n deeltje minder trillen dan in bulk goud, dus vaster zitten, en dat daardoor de Mössbauer absorptie groter is. Van de andere kant zitten er in zulke kleine deeltjes veel atomen aan het oppervlak, waardoor oppervlakte trillingen belangrijk

kunnen worden. Echter geen van deze mogelijke verschillen met bulk goud geeft een bevredigende beschrijving van de waargenomen veranderingen. Het blijkt dat de goud deeltjes als geheel trillen, waardoor mogelijke effecten t.g.v. de kleine afmetingen overschaduwd worden. Deze uitkomst werpt een nieuw licht op de paradoxale resultaten die tot nu toe verkregen waren aan kleine deeltjes van wolfraam en tin, waar geen rekening was gehouden met het trillen van de deeltjes als geheel.

LEVENSLOOP

De auteur werd geboren op 15 juli 1948 te Nijmegen. Na in 1966 het eindexamen gymnasium β te hebben behaald aan het Canisius College begon hij zijn scheikunde studie aan de Katholieke Universiteit te Nijmegen. Het kandidaats examen werd afgelegd op 27 april 1970, het doctoraal examen (cum laude) op 25 september 1972, met als hoofdvak molecuulspectroscopie en bijvak theoretische chemie. Van 1 oktober 1972 tot 1 oktober 1976 heeft hij als wetenschappelijk medewerker van de SON een promotie onderzoek verricht in de werkgroep molecuulspectroscopie.

I

Imanaka e.a. maken geen onderscheid tussen coincidentie en causaal verband, wanneer zij op grond van ESR spectra een katalytische hydrogeneringscyclus beschrijven met Rh(II) complexen.

T. Imanaka, K. Kaneda, S. Teranishi en M. Terasawa, "Proceedings of the Sixth International Congress on Catalysis", Part I, A41, London july 1976.

II

Het is nuttig na te gaan of het door Fletcher gevonden onverwachte gedrag van de roosterwarmtegeleiding van kalium ook gevonden wordt met behulp van het Corbino effect.

R. Fletcher, Phys. Rev. Lett. 32, 930 (1974).

III

Men realiseert zich te weinig dat er methodes zijn voor het produceren van rotary echo's, waarbij de 180° fasedraaiing van H_1 voorkomen wordt.

C.A. Van 't Hof en J. Schmidt, Chem. Phys. Lett. 36, 457 (1975).

E.J. Wells en K.H. Abramson, J. Magn. Res. 1, 378 (1969).

H. Kessemeier en W. Rhim, Phys. Rev. B 5, 761 (1972).

IV

Pollak e.a. negeren ten onrechte de bijdrage van "plasmon loss" satelliet-lijnen van de Al 2p piek tot de intensiteit van "plasmon loss" satellieten van de Al 2s piek.

R.A. Pollak, L. Ley, F.R. McFeely, S.P. Kowalczyk en D.A. Shirley, J. Electron Spectr. 3, 381 (1974).

V

De lage biologische activiteit, die voor het analogon $[Trp^3(5'F)]$-LH-RH werd gevonden, is veeleer toe te schrijven aan sterische inhomogeniteit dan aan verminderde electrondonor-eigenschappen van het op plaats 3 ingevoerde tryptofaan analogon.

Het is bijzonder verwarrend dat sommige auteurs de oorsprong in polaire ruimtegroepen kiezen door het fixeren van één of meerdere atoomparameters, terwijl andere auteurs geen van de atoomparameters fixeren.

J.E. Godfrey en J.M. Waters, Cryst. Struct. Comm. 4, 5 (1975).

K. Simon, Z. Meszaros en A. Kalman, Cryst. Struct. Comm. 4, 135 (1975).

Ter verkleining van persoonlijke risico's van deelnemers aan wedstrijden met voer-, vaar- of vliegtuigen dient men meer over te gaan op afstandsbesturing.

Thijs Viegers   Nijmegen, 12 nov. 1976